ALMA MATER STUDIORUM - UNIVERSITÀ DI BOLOGNA
Dottorato di ricerca in Scienze della Terra
CICLO XXVIII

Study of the optical properties of complex ice crystal aggregates

Application to the remote sensing of dry and mixed-phase snowfall

Davide Ori

Coordinatore dottorato
Jo Hilaire Agnes De Waele

Relatore
Tiziano Maestri

Settore Concorsuale di afferenza 02/C1
Settore Scientifico disciplinare FIS/06

Dipartimento di Scienze Biologiche,
Geologiche e Ambientali

Esame finale
15 Aprile 2016

Abstract

Snowfall is a prominent component of the Earth's hydrologic cycle. Global observations of snowfall are essential for the monitoring of the status of the Earth system, and because of their wide coverage, nowadays, remote sensing instruments are fundamental tools in the measurement of precipitation. The principal uncertainty in the interpretation of radar data are the scattering properties of the hydrometeors which are strictly connected to their microphysical characteristics. The presented study propose a comprehensive approach that analyze the all snow physical characteristics: single particle modeling, snowfall automatic microphysical retrieval, scattering simulations and remote sensing. A state of the art snow aggregation algorithm (SAM) has been implemented to model the snowflake accurate morphology, simulating the basic physical governing phenomena of snow formation and growth. The algorithm has been further extended to model the initial stage of snowflake melting. The snowflake models are used as input of computer scattering simulations. The analysis of the radiative properties obtained with the spherical models and the complex aggregated particles produced by SAM shows that the former are inadequate to represent the scattering characteristics of large aggregated particles. An innovative methodology has been developed to automatically estimate the mean snow mass-size relation using particle size distribution, velocity fits, snow accumulation and Rayleigh radar reflectivity. The radar reflectivities at Ka and W band simulated with T-matrix spheroidal models and using the retrieved mass-dimensional relation cannot match the observation. When the same simulation is performed with the usage of DDA scattering calculations the results reproduce better the observed radar reflectivities. This outcome gives validity to both the microphysical and the scattering model. A multi-perspective approach, that simultaneously include the microphysical and scattering simulation of snowflake properties, is the way forward to solve the uncertainties related to snowfall remote sensing.

Tutto ciò che non abbiamo,
è alla portata della nostra immaginazione
Everything we are missing,
is within the range of our imagination

Immaginazione non significa menzogna
Imagination doesn't mean lying
Daniel Pennac - Messieurs les enfants

Table of contents

List of figures

List of tables

Nomenclature

Symbols

A_r	Area ratio
α β	Parameters of the mass-dimensional power law relation $m(D) = \alpha D^{\beta}$
α_i	Polarizability of i-th dipole
a_r	Aspect ratio
C_a	Absorption cross section
C_d	Aerodynamic drag coefficient
C_e	Extinction cross section
D_0	Median volume diameter
D_{ec}	Equivalent area diameter
d_f	Fractal dimension
D	Diameter
D_{max}	Maximum dimension
D_{vol}	Equivalent volume diameter
$\varepsilon = n^2$	Relative dielectric constant
F_d	Aerodynamic drag force
G	Gauge measured precipitation accumulation
g	Earth mean vertical gravitational acceleration

$\Gamma(x)$ Complete Gamma function

γ δ Parameters of the velocity-dimensional power law relation $v(D) = \gamma D^{\delta}$

$K_w = (n_w^2 - 1)/(n_w^2 + 2)$ Dielectric factor of water

K_{dp} Specific differential phase shift

$k_{a\lambda}$ Spectral absorption coefficient

$k_{e\lambda}$ Spectral extinction coefficient

$\mathbf{k}$ Wave vector

l Mean free path

Λ Scale parameter of inverse exponential or unnormalized gamma distributions

λ Wavelength

m mass

M_k k-th order moment of distribution

μ Shape parameter of unnormalized Gamma distribution

$n = n_r + \imath n_i$ Complex refractive index

N_0 Intercept parameter of inverse exponential or unnormalized Gamma distributions

n_i Complex refractive index of ice

n_w Complex refractive index of water

ν Cinematic viscosity

$P_{col}(D_i, D_j)$ Size distribution of collision probability

ω Wave frequency

$\hat{\alpha}^{\text{ori}}$ Orientation vector of Euler angles

$N(D)$ Particle size distribution

$(\hat{\theta}, \hat{\phi})$ Polarization directions

$\mathbf{P}_i$ Polarization vector of i-th dipole

$\hat{\mathbf{n}} = (\theta, \phi)$ Propagation unit vector

R_e Reynolds number

r_{em} Equivalent mass sphere effective radius

r_g Radius of gyration

ρ_a Air density

ρ_{hv} Correlation coefficient

ρ_{SR} Snow Rate weighted bulk density

ρ_Z Reflectivity weighted bulk density

$\mathbf{S}$ Amplitude matrix

θ Scattering angle

$\sigma_{hh}\,\sigma_{vv}$ Radar copolar backscattering cross section at horizontal and vertical polarization

σ_{bk} Radar backscattering cross section

$\mathbf{N}_n, \mathbf{M}_n$ Vector spherical harmonics

$\mathbf{I} = (I\,Q\,U\,V)^T$ Stokes vector

T_b Brightness temperature

V_f Volume flux

V Volume

v_t Terminal fall velocity

X Davies (or Best) number

x Size parameter

$\mathbf{Z}$ Phase matrix

Zdr Differential reflectivity

Z_e Radar equivalent reflectivity factor

Z Radar reflectivity

Acronyms / Abbreviations

ACE Aerosol/Cloud/Ecosystem mission

ADDA Amsterdam DDA

AMF2 ARM Mobile Facility number 2

ARM Atmospheric Radiation Measurement Program

ARPA-ER Agenzia Regionale Protezione Ambientale Emilia Romagna (Emilia Romagna's regional environmental protection agency)

BAECC Biogenic Aerosol Effects on Clouds and Climate

C3VP Canadian CloudSat/CALIPSO Validation Project

CALIPSO Cloud-Aerosol Lidar and Infrared Pathfinder Satellite Observations

CAP Core Aggregating Particle

CCD Charge-Coupled Device

CDA Coupled Dipole Approximation

CloudSat Cloud Satellite

CPR Cloud Profiling Radar

DDA Discrete Dipole Approximation

DFIR Double Fence Intercomparison Reference

DFR Dual-Frequency Ratio

DLA Diffusion Limited Aggregation

DPR Dual frequency Precipitation Radar

EarthCARE Earth Clouds, Aerosols and Radiation Explorer

EBCM Extended Boundary Condition Method

EMA Effective Medium Approximation

FDTD Finite Difference Time Domain method

FFT Fast Fourier Transform

FMI Finnish Meteorological Institute

FPGA Field Programmable Gate Array

GMM Generalized Multi-particle Mie method

GPM Globale Precipitation Measurement

GPU Graphic Processing Unit

HCA Hydrometeor Classification Algorithm

HPC High Performance Computing

IWC Ice Water Content

KAZR Ka-band Zenith pointing Radar

LDR Linear Depolarization Ratio

LPVEx Light Precipitation Validation Experiment

MDV Mean Doppler Vertical velocity

MG Maxwell-Garnett effective medium approximation

MIC Many Integrated core

MRRM Moments Ratio Retrieval Method

MWACR Marine W-band ARM Cloud Radar

MW Microwave

MWR MicroWave Radiometer

NAP Next Aggregating Particle

OE Optimal Estimation method

PDF Probability Density Function

PIA Path Integrated Attenuation

PIP Particle Image Package

PPI Plane Position Indicator

PRF Pulse repetition frequency

PR Precipitation Radar

PSD Particle Size Distribution

PVI Particle Video Imager

QPE Quantitative Precipitation Estimation

RADAR RAdio Detection And Ranging

RGA Rayleigh-Gans Approximation

RHI Range-Height Indicator

RMSE Root Mean Square Error

RS Radio Sounding

SAM Snow Aggregation and Melting model

SR Snow Rate

SVI Snow Video Imager

TMM T-Matrix Method

TRMM Tropical Rainfall Measuring Mission

UH University of Helsinki

XSACR X-band ARM Cloud Radar

Chapter 1

Introduction

1.1 Motivation

Snowfall is a prominent component of the Earth's hydrologic cycle. For high latitude areas snowfall comprise 45% to 80% of global annual precipitation (Behrangi et al., 2014; Kidd et al., 2009). At high latitude regions, snowfall is the predominant type of precipitation and rainfall is almost always initiated in ice phase (figure 1.1). Most of worldwide reservoirs of fresh water are stored as glaciers and snowfields which act as source of fresh water for industry, hydroelectric power generation, landfill irrigation and human consumption through snowmelt.

As a principal component of the hydrological cycle snowfall has a significant meteorological and climatological impact since it enables precipitation related exchange of sensible and latent heat. Moreover snow cover has important role in the climate system. Snow cover largely increases surface albedo, leading to a great reduction of shortwave radiative heat absorption.

Finally, snowfall has a huge impact on human and economic activities since it dramatically affects logistics, general transportation and flow of supply. It may cause damages to buildings due to heavy accumulation over roofs and trees, cuts power lines, affects airport's activity, makes roads slippery and eventually blocks them. Since heavy snowfall events could quickly paralyze large regions, there is generally a large public interest in snowfall observation, quantification and forecasting.

Global observations of snowfall are essential for the monitoring of the status of the Earth system, and because of their wide coverage, nowadays, remote sensing instruments are fundamental tools in the measurement of precipitation. Precipitation patterns are discontinuous fields, therefore they cannot be adequately represented by point measurements. For hydrological and climate studies, vast-area observations such as the one provided by

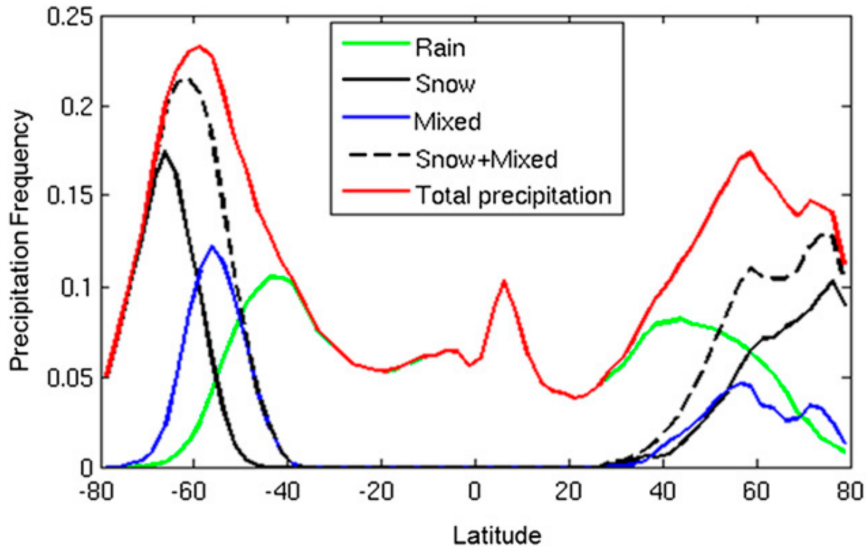

Fig. 1.1 Global zonal averaged distribution of precipitation phase frequency based on CloudSat 2007-2009 data. Image copied from Behrangi et al. (2014).

radars and other remote sensing instrument are more valuable then sparse, even if accurate, local measurements given by networks of precipitation gauges. Moreover there is poor coverage of direct meteorological observations in inhabited areas of the Earth such as polar regions, deserts and oceans. The atmospheric conditions at these areas affect the evolution of weather patterns at global scale. Furthermore, the northern polar regions are the areas most affected by the ongoing climate changes (Holland and Bitz, 2003). The particular characteristics of precipitation fields and the lack of *in-situ* observations in uninhabited areas has led to the introduction of remote sensing systems which allows nearly global coverage of meteorological observations.

Radars are the most commonly deployed ground-based remote sensing instruments. In contrast with radiometers, that passively measure the radiation emitted by hydrometeors, the brightness of the echo signal measured by radars could be directly related to the amount (intensity) of the precipitation. However, ground-based remote sensing systems are limited in range by the curvature of the Earth. Even though most developed countries are covered by networks of weather radars the coverage of radar observation is still limited by the needing of local appropriate infrastructure such as power connection, data links and maintenance services. Despite their costs, space-borne observation instruments give the unique opportunity to measure weather conditions in remote regions. In recent years there has been huge developments in deploying satellite based radar measurement missions. The first radar-equipped spacecraft dedicated to measurements of rainfall, the Tropical Rainfall

Table 1.1 Summary of principal specifications of space-borne radar mission

Mission/instrument	frequency [GHz]	range resolution [m]	sensitivity [dBZ]
TRMM/PR	13.8	250	18
CloudSat/CPR	94	500	-30
GPM/DPR-Ku	13.6	250	18
GPM/DPR-Ka	35.6	250/500	12
EarthCARE/CPR	94	500	-35
ACE/CPR	94	250	-35

Measuring Mission (TRMM) was launched in 1997 (Kummerow et al., 1998) and operated a precipitation radar (PR) at 13.8 GHz (Ku-band). The CloudSat (Stephens et al., 2002), launched in 2006 operates the Cloud Profiling Radar (CPR) a 94-GHz (W-band) radar. The Global Precipitation Measurement (GPM) core satellite (Hou et al., 2013) has been launched in 2014 and it includes the dual frequency precipitation radar (DPR). Another W-band radar (an upgraded version of CPR) is expected to be launched in 2018 on-board of the Earth-CARE (Illingworth et al., 2014) satellite. The value of space-borne radar measurements of precipitation is confirmed by the fact that there has been various proposal of new other space missions that make use of precipitation radars, such as the Aerosol/Clouds/Ecosystem (ACE) mission (Tanelli et al., 2009).

Remote sensing measurements of precipitation are inherently indirect. In order to interpret remote observation, one must identify and characterize all possible physical quantities that could affect the remote measurement and then try to retrieve the interesting properties of precipitation given the observations and any other available information. Most of the time, complete information about the state of the target is not available and thus many assumptions are needed in order to solve this inverse problem. The principal uncertainty in the interpretation of radar data are the scattering properties of the hydrometeors which are strictly connected to their microphysical characteristics (Bringi and Chandrasekar, 2001). Retrieving the precipitation rate through remote sensing requires then to infer also the properties of the hydrometeors using the knowledge about the scattering processes.

Despite the theoretical complexity of remote sensing, rainfall polarimetric radar retrieval has reached extraordinary good performance (Wang and Chandrasekar, 2010) due to the intrinsic simplicity of rain microphysics and scattering modeling. On the contrary, the characteristics of snowfall presents additional challenges to solving the problem of retrieving the precipitation intensity from radar signals. The large variability of the snowflakes structures makes retrievals more complicate as opposed to the relatively well known shape of raindrops as a function of size. While raindrops could be considered as homogeneous spheroids

snowflakes density is another important source of uncertainty. In addiction, snow particles are generally bigger than raindrops causing scattering properties of snowflakes to easily fall outside the Rayleigh regime. Finally, due to the dielectric properties of ice at microwave frequencies, compared to those of water, the snow radar echoes are weaker than those from rain. Mixed phase precipitation (wet snow) is even more challenging to measure because of the presence of water in both liquid and solid phase at the same time. Identifying the precipitation type is in itself nontrivial, and much research effort has been spent on this problem (e.g. Park et al. (2009); Straka et al. (2000), among others).

The modeling of radar measurements of snow is then composed of two fundamental parts. The description of the variability of microphysical features of snow and the accurate computation of the scattering properties of the individual particles (Petty and Huang, 2010).

Due to the high degree of the complexity of the problem, non-spherical ice crystals and snow aggregates have commonly been modeled, for radar and passive microwave (MW) radiative transfer purposes, as spheres or alternatively spheroids composed of a homogeneous mixture of air and ice (Korolev et al., 2003; Matrosov, 2007). These simplified models, commonly named soft-spheroid models, have reached a large popularity due to the associated exploitation of scattering numerical methods, such as the T-Matrix or TMM (Mishchenko et al., 2002), that allow to compute an analytic solution within short computational times. Nonetheless, the simplified assumption, concerning the shape of complex ice crystal, has been recognized to be one of the main sources of error in the retrieval of snowfall from remote sensing measurements (Kulie et al., 2010). Moreover (Leinonen et al., 2012; Petty and Huang, 2010) found that soft-spheroid models are unable to represent scattering properties of large aggregates which has been found to compose the majority of snow particles populations (Brandes et al., 2007). A comprehensive database of snowflake scattering properties that covers the natural variability of snowflake's shapes, dimensions, densities and aspect ratios is needed.

On the other hand, typically the description of snow particle microphysical properties have been made with the direct observation of single particles at surface Kajikawa (1972); Locatelli and Hobbs (1974); Mitchell et al. (1990); Nakaya and Tereda (1935). Many particle's characteristics (fall velocity, side-projected area, general shape, linear size) could be captured by automatic devices such as video-disdrometers and particle imagers, but the measurement of the mass of individual particles still require a lot of human effort[1]. For this reason, such observations are rare and usually involve only small samples, limiting the statistical representation of the microphysical properties of snow and leaving large

[1]Typically the measurement of single snowflake mass require the collection of the falling particle and the rapid direct measurement of the size of the melted drop

uncertainties in the description of the natural variability of snow properties among various geographical area and weather conditions. Other possibilities include bulk approaches that relates disdrometer measurements with integral quantities such as snow accumulation or radar reflectivity (Brandes et al., 2007). Bulk methods are able to overcome the inherent scarce amount of direct microphysical observation, but they are largely affected by the associated measurements and modeling uncertainties.

The accurate measurement of snow precipitation with any kind of measuring device remains a challenging task. Since environmental conditions (wind, temperature, humidity) have large impact on the accuracy of direct snow observations, the reliability of even simple gauge measurements is not always ensured (Rasmussen et al., 2011). Appropriate multi-sensor campaigns may help to determine these uncertainties through opportune consistency analysis between different measurement techniques. Nowadays, such kind of observational campaigns are more common as they are required to provide ground validation for associated satellite missions. The most recent multi-sensor campaigns include the Canadian CloudSat/CALIPSO Validation Project C3VP (Hudak et al., 2006), the Light Precipitation Validation Experiment LPVEx (L'Ecuyer et al., 2010), Atmospheric Radiation Measurement Program ARM (Stokes and Schwartz, 1994). These campaigns provide co-located measurements of bulk properties of snow (precipitation rate, snow depth, multifrequency radar reflectivity) as well disdrometer observations of particle size distribution and fall velocity. The simultaneous measurement of different snow quantities allows to study their physical consistency (Kneifel et al., 2010) and reduces uncertainties associated with automatic observations.

1.2 State of the art

A key problem that afflicts the development of snowfall retrievals is the lack of simultaneous in-situ observations of snowfall microphysics combined with measurements of radiative quantities. Ground based observations can not give broad spatial coverage, but nonetheless they allow to record long-term information linking microphysical structure of snowfall to radiative properties. Thus, ground-based observations can help to constrain snowfall retrievals that can eventually be applied to satellite remote sensing.

Snow particle modeling and single scattering simulations

As previously discussed, the first and most commonly used snowflake models are those of equivalent mass solid ice spheres (Smith, 1984) that makes use of Mie theory to determine the scattering and absorption properties of the flakes. The radiative properties of solid spheres are thus easier to compute than irregularly shaped aggregates, but it has been proved that they

are not always applicable. Kim (2006) used discrete dipole approximation, or DDA (Draine and Flatau, 1994), to compute various radiative properties of simple ice crystal aggregates made of cylinders with maximum dimension up to 5 mm and found that Mie theory did not adequately predict the single-scattering properties for these objects when the size parameter is greater than 2.5. In this case, size parameter is defined as $x = 2\pi r_{em}/\lambda$ where r_{em} is the radius of the equal mass solid ice sphere and λ is the wavelength of the incoming electromagnetic wave.

A slightly more sophisticated approach to solid sphere approximation is that of a soft sphere with the same geometrical dimensions of natural snowflakes and composed of a mixture of ice and air (Bennartz and Petty, 2001; Hogan et al., 2006). In this case, an effective dielectric constant is determined by mixing formulas (Bruggeman, 1935; Maxwell Garnett, 1904; Sihvola and Kong, 1988). Several studies have investigated the accuracy of such models. Liu (2004) compared radiative properties of dendritic and rosette ice crystals obtained with DDA and soft sphere approximation and concluded that the simulated brightness temperature does not match satellite measurements when soft sphere models are used. Kulie et al. (2010) analyzed the combined measurements of brightness temperature T_b and equivalent reflectivity factor Z_e from various satellite observations and compared them with simulated results obtained from radiative transfer modeling. Their conclusions highlight that simple ice particle models (e.g., low-density spheres) produce consistently implausible results when compared to actual measurements.

The principal obstacle to the extensive use of complex aggregate models and DDA calculations is the huge computational cost of DDA respect to the spherical Mie solution or the spheroidal TMM. For this reason, first scientific studies involving complex modeling of snow particles were limited to the analysis of single small pristine crystals (Botta et al., 2008; Evans et al., 1998, 2005; Grecu and Olson, 2008; Hong, 2007a,b; Liu, 2008a; Noh et al., 2006; Seo and Liu, 2005; Teschl et al., 2013). The use of these single crystals models are valid for satellite remote sensing studies that involve visible and infrared radiation (Yang et al., 2013) which are able to observe just the upper part of clouds where ice particles are usually simple ice crystals (Field and Heymsfield, 2003). On the contrary microwaves are capable of penetrating clouds and precipitation giving to satellite radars and microwave radiometers the possibility to sense snowfall below clouds. Many *in-situ* observations revealed that natural snow consists mostly of complex aggregates (Heymsfield et al., 2002a) composed of tens to thousands of pristine crystals. These larger particles significantly affect radar measurements. Since back scattering properties are particularly sensitive to the target's dimensions, few big particles in the radar volume can cause large deviations in the radar signal.

With the increasing of the computational power and availability of high performance computing (HPC) facilities, in recent years many studies have investigated the scattering properties of complex aggregated snowflakes. Petty and Huang (2010) investigated the suitability of soft-sphere models to represent extinction C_e and backscattering σ_{bk} cross sections of realistic aggregates at various radar frequencies. They found that it is not possible to find a single combination of density and particle mass that simultaneously captures the multifrequency properties of complex aggregates and therefore recommend to not use soft-sphere as general model for the microwave properties of snowflakes. Several studies have further confirmed these conclusions (Botta et al., 2011; Leinonen et al., 2012; Tyynela et al., 2011). After these results, databases of scattering properties of complex aggregated snowflakes have experienced a rapid development (Leinonen and Szyrmer, 2015; Nowell et al., 2013; Ori et al., 2014; Tyynelä and Chandrasekar, 2014).

Kulie et al. (2014) following the methodology proposed Kneifel et al. (2011) have shown that triple frequency measurements of snow could be linked to snow particle microphysical properties and deviations from the spheroidal model occurs in cases where large aggregates are present. These new concepts give the theoretical basis to implement a multifrequency snow retrieval with implicit microphysical parameterizations.

Some studies, have also attempted to simulate the radiative properties of mixed-phase particles (Botta and Aydin, 2010; Johnson et al., 2015; Ori et al., 2014; Tyynelä et al., 2014). This particular topic remains challenging for two main reasons: first, there are few studies that describe the microphysical process of snowflake's melting; and second, the addiction of water in the composition of the particles increases the computational cost of DDA, at microwave frequencies, by two orders of magnitude, making the scattering simulation nearly impracticable.

The scattering study from Petty and Huang (2010) have made use of an unusual formulation of the DDA algorithm that makes use of an optimized sparse representation of the dipole structure of the particle. This modification dramatically reduce the memory consumption of the program with a little computational time penalty. Such formulations are interesting for modern HPC environments where the use of accelerators such as graphic processing units (GPU), many integrated cores (MIC) or field programmable gate arrays (FPGA) is becoming more and more popular for general purpose computing. These kind of accelerators gives extraordinary computational performance when run programs with high level of parallelism and very low memory footprint. The implementation of the Petty and Huang (2010) technique for accelerators could open new possibilities for investigating radiative properties of complex snowflakes and mixed phase particles.

Microphysical properties of snow

The realistic snow aggregate models, mentioned in the previous section, are dependent on the observational data available regarding snow particle habit, particle size distributions (PSD), mass-size relations, and density. Therefore, a database of in-situ observations of various ice particles microphysical properties is needed.

In-situ observations of snow particle size distribution and snowflakes habits are still rare. Most of available databases are based on aircraft observations (Heymsfield et al., 2013, 2002a; Lawson et al., 2001). Some studies (Field and Heymsfield, 2007; Field et al., 2005), have found that aircraft observed particle size distribution are generally related to cloud temperature, giving the opportunity to predict PSD's parameters from basic thermodynamic measurements. But recent studies have recognized that existing aircraft observations are affected by spurious large amounts of small particles (Field et al., 2006; Gayet et al., 1996; Lawson, 2011) and ground measurements have found that PSD parameterizations tends to underestimate large snow particles (Löhnert et al., 2011). This evidence might be related to many physical phenomena like the sublimation of smaller ice crystals or near ground aggregation, but what poses serious concern about the reliability of existing aircraft datasets is the shattering of ice particles on optical probes (Korolev et al., 2013, 2010). Aircraft PSD measurements should then be carefully checked and cleaned by spurious artifacts (Heymsfield et al., 2008). Ground based observation datasets still lack of extensive spatial and temporal coverage, but they are more and more common and give the opportunity to investigate the microphysical properties of snow at the surface (Brandes et al., 2007; Garrett et al., 2012; Löhnert et al., 2011).

Snow mass-size relation (or density) are an essential part of snow characterization. Along with PSD, mass-size relation defines the ice water content (IWC). It is also strictly connected with the fallspeed-size relation (Heymsfield et al., 2002b) which gives the snow rate (SR). Finally, in Rayleigh regime, radar reflectivity could be expressed as proportional to the integral over the particle size distribution of the squared mass-size relation (Smith, 1984). Estimates of snow particle mass-size or velocity-size relations, made with surface observations, have typically involved measurements of individual particles from both natural (Kajikawa, 1972, 1975; Locatelli and Hobbs, 1974; Mitchell et al., 1990; Nakaya and Tereda, 1935) and laboratory experiments (Heymsfield and Westbrook, 2010). Due to the dramatically large amount of effort required for these studies the sample sizes have necessarly to be small. Nonetheless, field studies have been performed primarily in mountain locations, limiting the spatial and coverage of the datasets.

Another possible approach involves the derivation of bulk microphysical properties. Integral quantities such as accumulated precipitation or radar reflectivities (Brandes et al.,

2007; Heymsfield et al., 2004) are directly related to certain moments of the particle size distribution, thus, the measurement of such quantities provide information on the bulk properties of the PSD. Given the relative simplicity of bulk measurements, these studies have been capable to greatly extend the quantity of available microphysical retrieval, but bulk approaches are not always easily linked to size resolved microphysical relations. In fact, it is well known that the properties of a arbitrary distribution are fully described by the complete series of its moments which is generally infinite. These kind of problems are therefore generally inherently ill-posed and many assumptions on the formulation of snow properties size relation are needed in order to reduce the complexity of the retrieval problem. Moreover, generally only few bulk measurement are available (precipitation accumulation and eventually reflectivity) whereas even with the simplest parameterizations (inverse exponential size distribution and power laws for mass and velocity as function of the particle size) the number of unknown variables is larger, resulting in an under-constrained problem.

These kind of problems are generally addressed by combining observations with a-priori information in a probabilistic framework. Recently, Wood et al. (2014) proposed a Bayesian variational method called Optimal Estimation (OE) method (Rodgers et al., 2000) to retrieve microphysical properties of snowfall from multisensor measurements. With this approach, the microphysical properties of snow are retrieved in terms of probability density functions (PDFs) which describe the expected values and the covariances for these properties. These kind of studies are particularly relevant because they provide results that are physically consistent among different snow measurements, along with estimates of the result uncertainties. Results from Wood et al. (2015) suggest that some microphysical properties could be directly retrieved from multiple measurements. This approach should be further investigated because direct retrievals makes clearer which are the physical mechanisms that connect the microphysical properties to the measurements and makes possible instrument errors more evident.

1.3 Objectives and outline

The work presented in this study aims to improve the retrieval capabilities of snow precipitation through remote sensing instruments focusing especially on radar measurement techniques.

A brief introduction of the general concepts behind snow radar retrieval is illustrated in chapter 2. This study could be then divided in three principal areas.

The first part focuses on the modeling of snow particle structure and scattering properties. The structural modeling of snow particle analyses the principal processes of snowflakes

formation making use of state of the art knowledge on ice crystals nucleation, growing and aggregation (chapter 3). An original snow aggregation algorithm is described in section 3.1. The snow particle model includes also an initial attempt of snow melt simulation (section 3.2) and thus, the major challenges of mixed-phase particle modeling are illustrated.

The snow particle models are used as basis to compute the scattering properties of realistic shaped ice aggregates in chapter 4. These scattering properties are compared to those obtained with simplified models accounting for inhomogeneous distribution of ice mass inside the snowflake showing the importance of accurate modeling of ice particles when wavelength much smaller than the particle's dimension are accounted for. Finally, section 4.4 discuss the computational cost of these precise scattering calculations and illustrate an innovative methodology that makes use of low memory intensive scattering model in conjunction with exploitation of modern accelerators which are becoming more and more popular for scientific high performance computing.

In the second area, the presented study aims to improve the characterization of snow microphysical properties and their uncertainties. Chapter 5 illustrates a novel scheme for the retrieval of snow mass-size relationship that makes use of co-located disdrometer and bulk observations. The study explains the basic relations between snow properties that allows the microphysical retrieval and apply the new methodology to three snow events recorded during the Biogenic Aerosols Effects on Clouds and Climate (BAECC) field campaign that took place at the University of Helsinki Hyytiälä Forestry Field Station, Finland (Petäjä et al., 2013). In this retrieval, observations of snow rate, particle size distribution, fallspeeds and X-band radar reflectivity are used to estimate the parameters of power laws describing particle mass as a functions of size. Other complementary measurements are used to analyze the consistency of the derived quantities.

The third part of the study is dedicated to the application of methods illustrated in previous sections to real snowfall events. In particular section 6.2 illustrates the work carried on at the Emilia Romagna environmental agency (ARPA-ER) to implement an state of the art fuzzy logic hydrometeor classification algorithm (HCA). The microphysical parameters obtained in 5 are used in combination with accurate scattering properties calculated in chapter 4 to estimate radar reflectivity at Ka- and W-band. The comparison with observational data shows the accuracy and consistency of the joint microphysical and modeling of snow carried on in this study.

Finally, the principal results are summarized along with prospects for future work in chapter 7.

Chapter 2

Concepts of Radar Measurements

Remote sensing techniques measures the interaction of electromagnetic waves with hydrometeors, aerosols and atmospheric gases to retrieve the physical state of the atmosphere. Remote sensing instruments are designed to take advantage of the different types of interaction between matter and radiation, namely absorption, emission and scattering.

This chapter briefly overview the interacting processes of radiation with atmospheric components and how they can be exploited to retrieve the atmospheric state through remote sensing measurements. The review will focus on the microwave [1] region which is one of the most used frequency range for the remote sensing of precipitation. The general principles of radar technology and retrieval is presented more extensively and it will be used in subsequent chapters. The theory presented in this chapter is partially drawn from Bohren and Huffman (1983); Bringi and Chandrasekar (2001); Mishchenko et al. (2002).

2.1 Interaction of matter and radiation

Classical electromagnetic phenomena are mathematically described by the set of Maxwell's equations (Jackson, 1962). The fundamental properties of these equations is that they allow the representation of the electromagnetic field in a homogeneous medium as a superposition of plane traveling waves which takes the form

$$\mathbf{E}(\mathbf{x},t) = \mathbf{E}_0 \exp(\imath \mathbf{k}\cdot\mathbf{x} - \imath\omega t) \tag{2.1}$$

where $\mathbf{E}_0$ is the amplitude of the electromagnetic wave, $\mathbf{k}$ is the wave vector and ω is the wave frequency. $\mathbf{x}$ and t are respectively the spatial and temporal coordinates.

[1] Microwaves are usually defined as the frequency range between 3 and 300 GHz, that corresponds to wavelengths from 1 m to 1 mm

Most optical instruments cannot measure the electric field, conversely, they measure the intensity of radiation and its polarimetric state. An important representation of this quantities are the so called Stokes parameters. These parameters will be defined in a spherical coordinate system associated with a local right-handed Cartesian coordinate system having its origin at the observation point

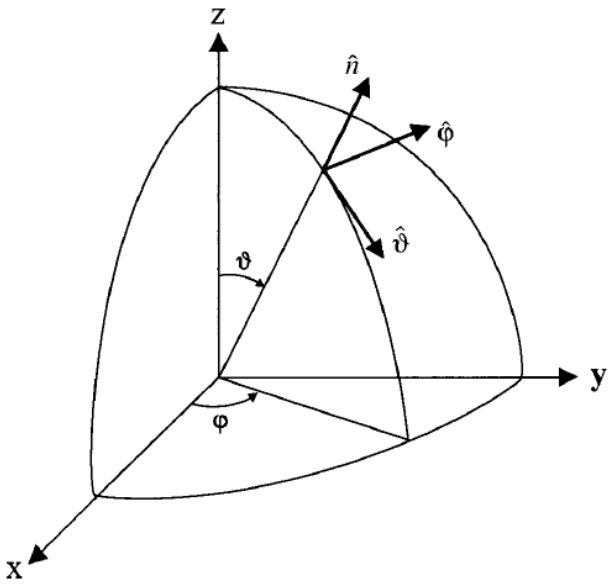

Fig. 2.1 Spherical reference frame for electromagnetic wave. Image extracted from Mishchenko et al. (2002). The direction of propagation of the electromagnetic wave is $\hat{\mathbf{n}}$, θ and ϕ are respectively the zenith and azimuth angle respect to the observation point which correspond to the polarization states $\hat{\theta}$ and $\hat{\phi}$.

The direction of propagation of a plane electromagnetic wave is specified by $\hat{\mathbf{n}}$ or, equivalently, by the couplet (θ,ϕ), where $\theta \in [0,\pi]$ is the polar (zenith) angle measured from the positive z-axis and $\phi \in [0,2\pi]$ is the azimuth angle measured from the positive x-axis in the clockwise direction. The electromagnetic field is then conveniently divided into its components along the local $\hat{\theta}$ and $\hat{\phi}$ directions which correspond to the vertical and horizontal polarization state for radars.

$$\mathbf{E}(\mathbf{x},t) = \mathbf{E}_{\hat{\theta}}(\mathbf{x},t)\hat{\theta} + \mathbf{E}_{\hat{\phi}}(\mathbf{x},t)\hat{\phi} = \begin{cases} \mathbf{E}_{\hat{\theta}}(\mathbf{x},t) = E_{\theta}\exp(\imath\hat{\theta}\cdot k\mathbf{x} - \imath\omega t) \\ \mathbf{E}_{\hat{\phi}}(\mathbf{x},t) = E_{\phi}\exp(\imath\hat{\phi}\cdot k\mathbf{x} - \imath\omega t) \end{cases} \tag{2.2}$$

The Stokes parameters I, Q, U, and V carry the intensity information about each orthogonal component of the electromagnetic wave and they are usually represented as the elements

of a 4×1 column vector **I**, otherwise known as the Stokes column vector, as follows:

$$\mathbf{I} = \begin{pmatrix} I \\ Q \\ U \\ V \end{pmatrix} = \begin{pmatrix} \mathbf{E}_\theta \mathbf{E}_\theta^* + \mathbf{E}_\phi \mathbf{E}_\phi^* \\ \mathbf{E}_\theta \mathbf{E}_\theta^* - \mathbf{E}_\phi \mathbf{E}_\phi^* \\ -\mathbf{E}_\theta^* \mathbf{E}_\phi - \mathbf{E}_\theta \mathbf{E}_\phi^* \\ \imath(\mathbf{E}_\theta \mathbf{E}_\phi^* - \mathbf{E}_\theta^* \mathbf{E}_\phi) \end{pmatrix} \tag{2.3}$$

Stokes parameters give a numerical representation of the so called *polarization ellipse*. The first parameter I represent the total intensity of the electromagnetic wave. The parameters Q measures the difference between the intensity of the two orthogonal components of the radiation in the $(\hat{\theta}, \hat{\phi})$ reference frame[2] whereas V measures the component intensity difference in a reference frame rotated by 45°. V indicates the intensity difference of the components in the circular reference frame. For pure monochromatic coherent radiation the Stokes parameters satisfy

$$I^2 = Q^2 + U^2 + V^2 \tag{2.4}$$

Figure 2.2 gives a quick look of particular degenerate states of the Stokes vector. Panels (a), (b), (c) and (d) represent common linear polarized waves used by polarimetric weather radars.

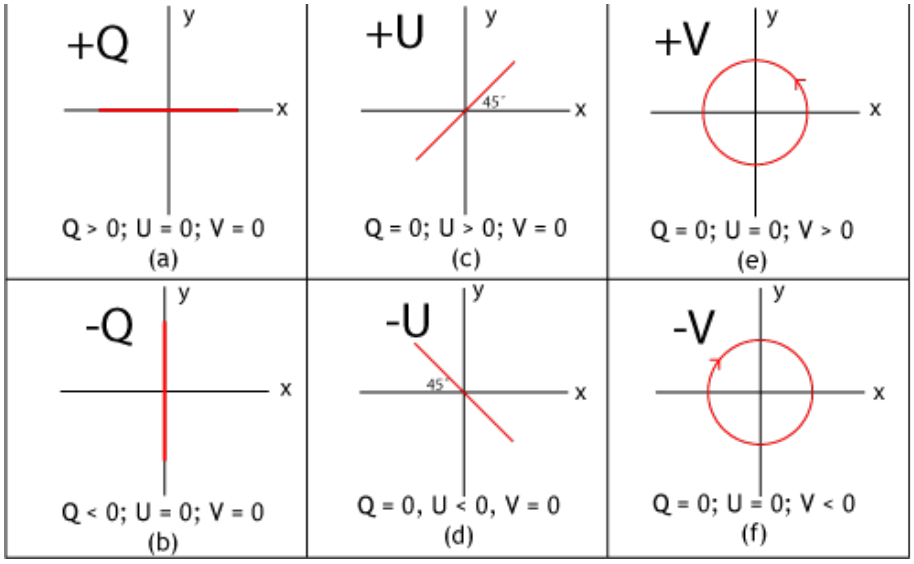

Fig. 2.2 Stokes parameters: Polarization state of electromagnetic wave in some degenerate cases

[2] (x, y) in figure 2.2

2.1.1 Absorption and emission

Electromagnetic waves are absorbed by matter when traveling through it. In general the variation of radiation intensity caused by traversing a piece of matter of thickness ds in the propagation direction is

$$dI_\lambda = -k_{e\lambda} I_\lambda ds \tag{2.5}$$

where the $k_{e\lambda}$ denotes the *extinction coefficient* and the subscript λ indicates that interaction properties are wavelength dependent. The extinction characteristics of matter are the sum of the absorption and scattering properties. For homogeneous media, such as the atmospheric gases, the absorption coefficient is linearly dependent on the imaginary part m_i of the complex refractive index $n = n_r + \imath n_i$

$$k_a(\lambda) = \frac{4\pi n_i(\lambda)}{\lambda} \tag{2.6}$$

At typical radar frequencies, the contribution of radiation extinction by gas absorption is negligible compared to the absorption and scattering from particulate matter (aerosols, hydrometeors, insects and birds). When the absorbing medium consists of a large number of dispersed, the absorption coefficient can be calculated by the integral

$$k_a(\lambda) = \int_0^\infty C_a(D,\lambda) N(D) dD \tag{2.7}$$

where $C_a(D,\lambda)$ is the size dependent absorption cross section of the particles, and $N(D)$ denotes the particle size distribution (PSD).

A perfect absorber emits radiation according to the *Planck function*. Most objects, in reality, are far from being perfect absorbing bodies and the ratio between the emitted monochromatic intensity and the radiation given by the Planck function is denoted as *emissivity*. *Kirchhoff's law* reveals that, at thermodynamic equilibrium, the emissivity of a body is equal to the ratio of absorbed radiation to incident radiation (*absorptivity*) for a specific viewing angle and wavelength.

Measuring emission and absorption of radiation helps radar meteorologist to determine the radar attenuation due to wet antenna/radome or heavy rainfall. Since the imaginary part of the complex refractive index of ice is small, attenuation due to absorption by frozen hydrometeors could ignored in most cases.

2.1.2 Scattering

When an electromagnetic wave crosses a boundary between two different refractive indexes it changes its direction of propagation. Unlike the absorption process, scattering does not deplete radiation energy, but diffuse it into different directions. The scattered field is the difference between the total field in presence of the scattering object and the field that would exist in conditions of perfectly continuous and homogeneous medium. The formal solution of the scattering problem is described by the complex 2x2 *amplitude scattering matrix* $\mathbf{S}$ that relates the incident electric field $\mathbf{E}^{\text{inc}}$ to the scattered field $\mathbf{E}^{\text{sca}}$

$$\mathbf{E}^{\text{sca}}(\hat{\mathbf{n}}^{\text{sca}}) = \begin{pmatrix} E_h^{\text{sca}}(\hat{\mathbf{n}}^{\text{sca}}) \\ E_v^{\text{sca}}(\hat{\mathbf{n}}^{\text{sca}}) \end{pmatrix} = \frac{\exp(\imath kr)}{r}\mathbf{S}(\hat{\mathbf{n}}^{\text{inc}}, \hat{\mathbf{n}}^{\text{sca}}, \hat{\alpha}^{\text{ori}}) \begin{pmatrix} E_h^{\text{inc}} \\ E_v^{\text{inc}} \end{pmatrix} \tag{2.8}$$

As equation 2.8 shows, the angular distribution of the scattered field depend on the physical and geometrical properties of the scatterer (size, composition, and shape) as well as the orientation of the particle $\hat{\alpha}^{\text{ori}}$ and the propagation direction of the of the incident and scattered electromagnetic wave $(\hat{\mathbf{n}}^{\text{inc}}, \hat{\mathbf{n}}^{\text{sca}})$. From the $\mathbf{S}$ matrix elements it is easy to compute the scattering properties relevant for remote sensing. For example the radar backscattering cross sections needed to compute copolar radar reflectivity are

$$\sigma_{hh} = 4\pi \left| S_{11}(\hat{\mathbf{n}}^{\text{inc}} = -\hat{\mathbf{n}}^{\text{sca}}) \right|^2 \tag{2.9}$$

$$\sigma_{vv} = 4\pi \left| S_{22}(\hat{\mathbf{n}}^{\text{inc}} = -\hat{\mathbf{n}}^{\text{sca}}) \right|^2 \tag{2.10}$$

In analogy to equation 2.8, the scattering process could be represented in terms of Stokes vector and the real 4x4 *phase matrix* $\mathbf{Z}$ which gives an immediate look to the intensity of scattered electromagnetic wave

$$\mathbf{I}^{\text{sca}}(\hat{\mathbf{n}}^{\text{sca}}) = \frac{1}{r^2}\mathbf{Z}(\hat{\mathbf{n}}^{\text{inc}}, \hat{\mathbf{n}}^{\text{sca}}, \hat{\alpha}^{\text{ori}})\mathbf{I}^{\text{inc}} \tag{2.11}$$

Scattering properties are in general strongly dependent on the so called *size parameter* which represent the ratio between the size of the scattering particle and the wavelength of the incident radiation

$$x = 2\pi D/\lambda. \tag{2.12}$$

The scattering properties of particles at any size parameter x are fully described by the Maxwell's equations and, in particular, the Mie scattering theory can entirely characterize the scattering properties of spherical targets regardless of their size. However it is common to identify three main "scattering regimes", dividing the general scattering theory from

its asymptotic limits for very small and very large size parameters. By contrast to the Mie theory, which provides an analytic solution only for spherical objects, these scattering approximations are applicable only within certain restriction to the size parameters, but can calculate the optical properties of arbitrary shaped particles.

Geometric optics

The upper limit of scattering theory occurs when $x > 10^3$. In this regime, *geometric optics* or ray tracing methods can be applied. In atmosphere this happen when visible light is scattered by water drops and ice crystals enabling impressive optical phenomena such as rainbows and halos. For microwave radiation this scattering regime is not occurring in atmosphere and it will be neglected in this study.

Rayleigh scattering

When the scattering particles are small compared to the radiation wavelength $x \ll 1$ Rayleigh approximation applies.

The most common example for Rayleigh scattering in the atmosphere is the scattering of visible light at air molecules which partially explains the blue color of the sky. However, also many radar applications fall within the Rayleigh scattering regime (typical wavelength for operational weather radar ranges from 3 to 10 cm whereas hydrometeor sizes fall in the millimeter range).

Since the wavelength is much larger than the particle, the polarization induced by the external electric field on each part of the particle can considered at the same phase. It can be shown that the amplitude scattering matrix under the restrictions of Rayleigh (Strutt, 1871) regime is

$$\mathbf{S}(\theta) = \frac{3\pi}{\lambda^2}\left(\frac{n^2-1}{n^2+2}\right) V \begin{pmatrix} 1 & 0 \\ 0 & \cos(\theta) \end{pmatrix} \tag{2.13}$$

where V is the volume of the particle and θ is the *scattering angle*, i.e. the angular difference between the incident and the scattered field. Considering a spherical particle with diameter D, the relation between the incident and scattered intensity of unpolarized light is

$$\mathbf{I}^{\mathrm{sca}}(\theta) = \frac{\mathbf{I}^{\mathrm{inc}}}{r^2} 2D^6 \left(\frac{\pi}{2\lambda}\right)^4 \left(\frac{n^2-1}{n^2+2}\right)^2 (1+\cos^2(\theta)) \tag{2.14}$$

The total scattering cross section is calculated integrating equation 2.14 over the whole solid angle. And the radar backscattering cross section is obtained from equation 2.14

considering only the backward scattering direction

$$C_s = \frac{2}{3}\frac{\pi^5 D^6}{\lambda^4}\left(\frac{n^2-1}{n^2+2}\right)^2 \tag{2.15}$$

$$\sigma_{bk} = \frac{\pi^5 D^6}{\lambda^4}\left(\frac{n^2-1}{n^2+2}\right)^2 \tag{2.16}$$

The most prominent feature of Rayleigh scattering is its sensitivity to scatterers size. Rayleigh scattering cross sections are proportional to the sixth power of the particle dimension, thus aggregation and coalescence of particles greatly enhances the intensity of scattered radiation in Rayleigh regime.

The assumptions of the Rayleigh approximation are valid for most measurements by ground-based weather radars which use wavelength ranging from 3 cm (X band) to 10 cm (S band). For this reason, Rayleigh approximation is the basis of the definition of radar reflectivity (section 2.3.1), but for higher frequency radars (K and W bands) Rayleigh approximation is no longer valid.

Mie scattering

If $x \geq 1$ the conditions of Rayleigh approximation breaks because the spatially distributed parts of the scattering particle experience a different phase of the incident electric field. This leads to complex interactions and usually numerical approximations have to be employed in order to obtain the scattering properties of particles in Mie regime. A typical example of scattering in the Mie regime is the scattering of millimeter-sized wave at large hydrometeors like snowflakes or hailstones.

Nonetheless, the solution of the scattering problem for highly symmetrical particles could be found analytically. Mie (1908) derived a solution for the wave equations scattered by homogeneous spheres that is commonly known as *Mie Theory*. A rigorous derivation of Mie theory can be found in van de Hulst (1957). The solution for this particular problem is found expanding the scattered electrical field in terms of vector spherical harmonics $(\mathbf{N}_n, \mathbf{M}_n)$ with expansion coefficients a_n and b_n

$$\mathbf{E}^{\text{sca}} = E_0 \sum_{n=1}^{\infty} (\imath)^n \frac{2n+1}{n(n+1)} \left[\imath a_n \mathbf{N}_n + b_n \mathbf{M}_n\right] \tag{2.17}$$

where E_0 is the amplitude of the incoming electromagnetic wave.

Imposing the continuity condition at the edge of the spherical scattering particle the expansion coefficients a_n and b_n can be calculated with an analytic expression, then the main

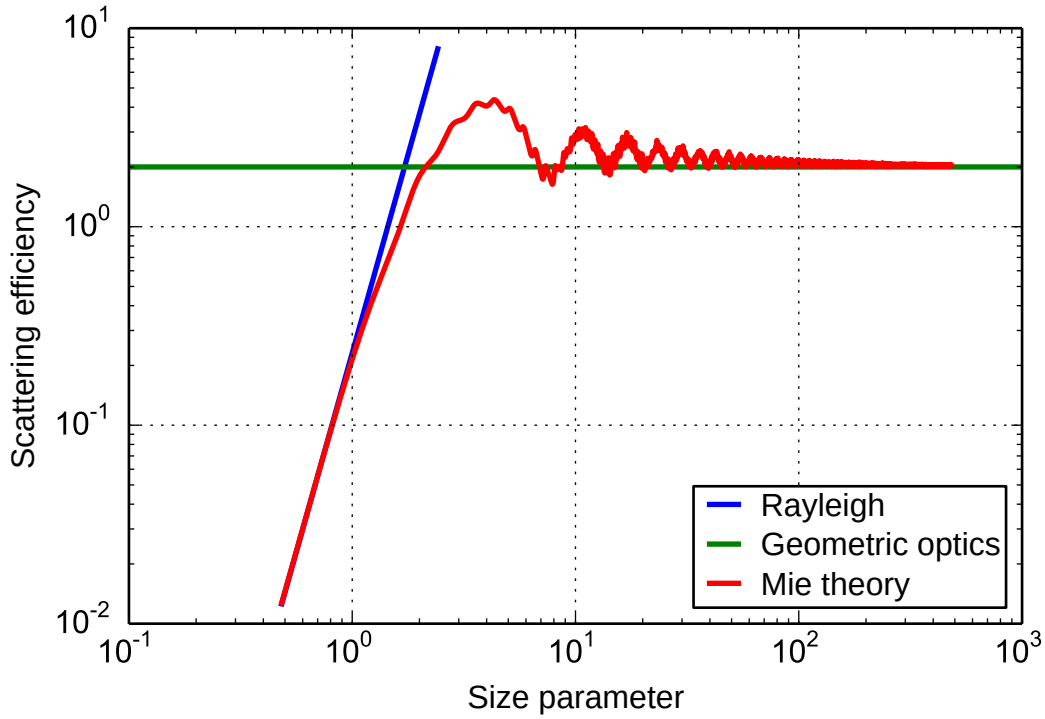

Fig. 2.3 Scattering efficiency of an homogeneous solid sphere with refractive index $n = 1.5$ as a function of its size parameter (red line). Green and blue lines are respectively the geometric optics and Rayleigh approximation.

scattering properties of the particle can be expressed as convergent series

$$C_s = \frac{\lambda^2}{2\pi} \sum_{n=1}^{\infty} (2n+1)(|a_n|^2 + |b_n|^2) \tag{2.18}$$

$$\sigma_{hh} = \frac{\lambda^2}{4\pi} \left| \sum_{n=1}^{\infty} (2n+1)(-1)^n (a_n - b_n) \right|^2 \tag{2.19}$$

In order to compare Rayleigh and Mie scattering it is useful to introduce the *scattering efficiency* which is the scattering cross section normalized by the projected area of the scattering particle.

$$Q_s = 4C_s/\pi D^2 \tag{2.20}$$

Figure 2.3 shows the scattering efficiency of an homogeneous solid sphere with refractive index $n = 1.5$ as a function of its size parameter. The asymptotic limits of Rayleigh and geometric optics are illustrated for comparison.

Even if analytic, the Mie solution is a convergent series and needs to be truncated at a certain point for practical reasons. Wiscombe (1980) found that the optimal truncation point $\tilde{n}$ for the series expansion is dependent on the size parameter

$$\tilde{n} = x + 4x^{1/3} + 2 \tag{2.21}$$

The Mie theory gives analytic solution of the scattering problem only for spherical targets. Rain drops are not exactly spherical, but Mie theory has been commonly employed to compute the scattering properties of raindrops with sufficient accuracy. Mie theory can be generalized to multi-layered spheres(Aden and Kerker, 1951; Yang, 2003) allowing the sphere model to represent radial distributed inhomogeneities in the particle's structure.

2.2 Simulation of single scattering properties

Rayleigh approximation applies when the small size parameter condition is satisfied independently from the scatterers shape. Mie theory works at any size parameter, but an analytic solution has been found only for spherical particles. When the scattering objects are not spherical other methods aiming to compute the single scattering properties are needed. Among others, the most used scattering methods for microwave radiative transfer are the T-Matrix Method (TMM) and the Discrete Dipole Approximation.

A fundamental part of scattering simulation is also the characterization of the refractive index of the scattering particles. The dielectric properties of ice and water are the most basic information needed for precipitation remote sensing. Many scattering methods are suitable only for homogeneous particles, thus effective medium approximation are frequently used to compute the dielectric properties of hydrometeors composed of mixtures of water, ice and air.

2.2.1 T-Matrix Method

The incident and the scattered field are related via the amplitude matrix $\mathbf{S}(\hat{\mathbf{n}}^{\text{inc}}, \hat{\mathbf{n}}^{\text{sca}}, \hat{\alpha}^{\text{ori}})$ (equation 2.8) which is dependent on the scattering particle orientation and the propagation directions of the incident and the scattered electromagnetic wave. In general, a new solution of the scattering problem is needed anytime the orientation of the particle or the scattering angle is changing. The computational cost of this problem could be alleviated just by important particle symmetries, which lead to the rather simple Mie solution for the spherical particles.

A generalized formulation of the scattering from ellipsoidal objects has been developed by Waterman (1965). Following the same conceptual framework of the Mie theory, incident and scattered fields are expanded in vector spherical harmonics

$$\mathbf{E}^{\text{inc}}(\mathbf{r}) = \sum_{n'=1}^{\infty} \sum_{m'=-n'}^{n'} [a_{m'n'}\mathbf{M}_{m'n'}(k\mathbf{r}) + b_{m'n'}\mathbf{N}_{m'n'}(k\mathbf{r})] \tag{2.22}$$

$$\mathbf{E}^{\text{sca}}(\mathbf{r}) = \sum_{n=1}^{\infty} \sum_{m=-n}^{n} [p_{mn}\mathbf{M}_{mn}(k\mathbf{r}) + q_{mn}\mathbf{N}_{mn}(k\mathbf{r})] \tag{2.23}$$

The series of expansion coefficient of the incident (a_{mn}, b_{mn}) and the scattered (p_{mn}, q_{mn}) waves are then related through the so called T-matrix.

$$\begin{pmatrix} p_{mn} \\ q_{mn} \end{pmatrix} = \begin{pmatrix} \mathbf{T}_{11} & \mathbf{T}_{12} \\ \mathbf{T}_{21} & \mathbf{T}_{22} \end{pmatrix} \begin{pmatrix} a_{m'n'} \\ b_{m'n'} \end{pmatrix} \tag{2.24}$$

The most important feature of this method is that the T-matrix is only dependent on the radiation's wavelength and on the particle's shape and composition. Once T-matrix is obtained it is relatively easy to derive the particle scattering properties for any particle's orientation and any scattering angle. This is particularly advantageous for many applications, including scattering by hydrometeors, that need to perform the orientation averaging of the scattering properties.

The elegance of the T-matrix formalism (equation 2.24) hides its fundamental complexity. It is worth to note that each of the four elements of the T-matrix is actually a four dimensional infinite series of tensor $\mathbf{T}_{11} = \mathbf{T}_{11}(m, n, m', n')$ and the T-matrix representation of scattering requires to truncate the series expansion at a certain point in order to be calculated.

The T-Matrix method is actually just a useful formalism that needs to be coupled with a method which is able to compute the T-matrix itself. Many computational methods have been applied in combination with the T-Matrix formalism (null-field method, generalized point matching, method of moments, discrete dipole approximation), but just few of them have acquired large popularity due to the computational cost of calculating the T-Matrix.

The T-Matrix code by Mishchenko and Travis (1998) makes use of the null-field method (also known as extended boundary condition method EBCM) to efficiently calculate the T-matrix of rotationally symmetric homogeneous particles such as cylinders, spheroids and Chebyshev particles. This formulation of the T-Matrix algorithm is popular among radar scientists because spheroids are quite accurate models of raindrops (Thurai et al., 2007). The spheroidal representation of hydrometeors allows to simulate the polarimetric properties

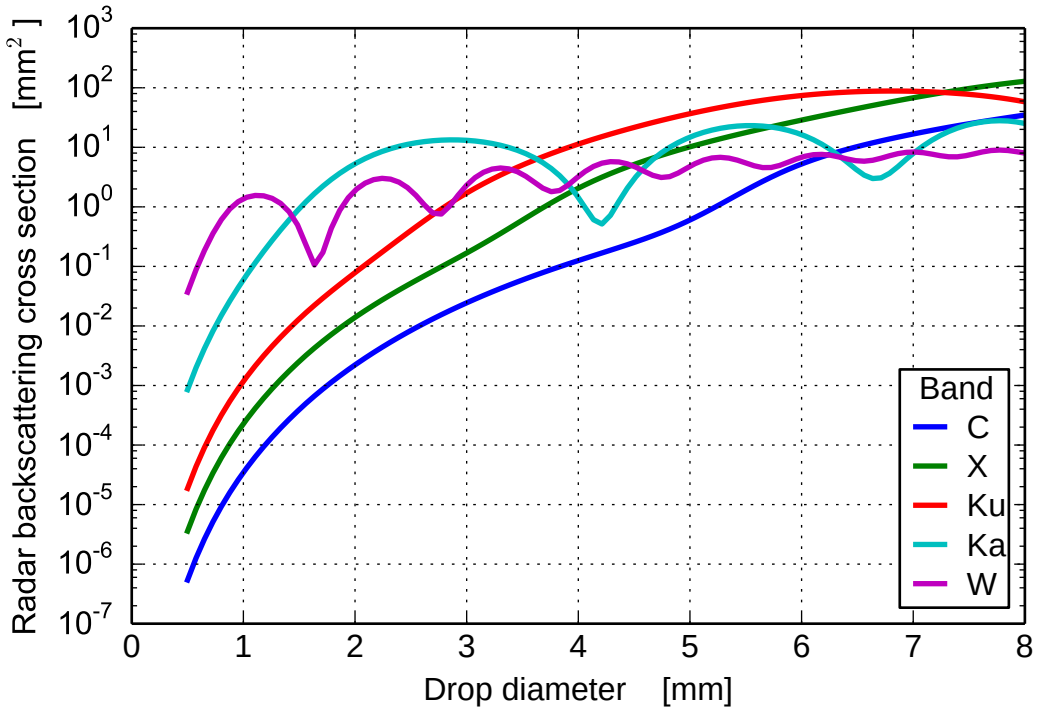

Fig. 2.4 Radar backscattering cross section at different radar bands for raindrop diameter ranging from 0.5 to 8 millimeters calculated with T-Matrix method for spheroids. The raindrop aspect ratio changes with the diameter according to Thurai et al. (2007).

of precipitation which is a largely accepted method to further constrain the weather radar retrieval process.

Figure 2.4 shows the radar backscattering cross section calculated with T-Matrix (Leinonen, 2014) for raindrops with diameter ranging from 0.5 to 8 millimeters. Drops with diameter smaller than 1 mm could be considered in the Rayleigh scattering regime at all the calculated frequencies and the radar back scattering cross section is proportional to D^6/λ^4. At larger drop diameters the Rayleigh assumptions are no longer valid and the Mie's resonance phenomena become evident.

The original work of Waterman (1965) was intended to establish a methodology to compute the scattering properties of ellipsoidal particles applying the so called *Huygens principle* and the concept of expanding the incident and scattered waves in vector spherical wave functions was perceived as auxiliary to the main problem. However, relating these expansions by means of the T-matrix has proved to be extremely powerful by itself and has dramatically expanded the applicability of the T-matrix approach beyond the traditional scope of simulating the electromagnetic scattering of rotationally symmetric particles. Ad-

vanced algorithms able to compute the T-matrix for specific shapes are available, including cubes (Yurkin and Kahnert, 2013) and prisms with finite symmetries (Kahnert, 2013). A database of the T-matrix related publications regarding electromagnetic scattering can be found in Mishchenko et al. (2013). The T-matrix methodology has been also extended to non-electromagnetic scattering such as acoustic and elastic waves (Ganesh and Hawkins, 2008; Varadan et al., 1988).

2.2.2 Discrete Dipole Approximation

Mie theory and T-Matrix method calculate the scattering properties by solving the differential Maxwell equation and thus the scattering particles are described in terms of their surfaces. For completely irregular particles (like e.g. snowflakes) it is more convenient to describe the scatterer in terms of its volume and therefore, to solve the scattering problem in terms of the *volume integral equation*

$$\mathbf{E}(\mathbf{r}) = \mathbf{E}^{\text{inc}}(\mathbf{r}) + k^2 \left(\mathbf{I} + \frac{1}{k^2} \nabla \times \nabla \right) \int_V \mathrm{d}\mathbf{r}' [n^2(\mathbf{r}') - 1] \mathbf{E}(\mathbf{r}') \frac{\mathrm{e}^{\imath k|\mathbf{r}-\mathbf{r}'|}}{4\pi|\mathbf{r}-\mathbf{r}'|} \tag{2.25}$$

where $n(\mathbf{r}')$ is the spatial distribution of the refractive index inside the particle volume V and $\mathbf{E}(\mathbf{r}')$ is the electric field inside the scattering particle.

As a first approximation of equation 2.25 it is possible to consider $\mathbf{E}(\mathbf{r}') = \mathbf{E}^{\text{inc}}(\mathbf{r})$ which reduces the integral equation to an ordinary analytic integral formula. This approximation is commonly referred as the *Rayleigh-Gans approximation* (RGA) and has been also used for simulating snowflake scattering properties at microwave frequencies (Tyynelä et al., 2013; Westbrook et al., 2006).

Discrete Dipole approximation was first introduced by DeVoe (1964) and formalized by Purcell and Pennypacker (1973). The basic idea behind DDA is to discretize equation 2.25 describing the scattering particle with a cluster of small polarizable volumes which behave as simple electric dipoles.

Each polarizable region i reacts linearly to the local electric field $\mathbf{E}_i$ as

$$\mathbf{P}_i = \alpha_i \mathbf{E}_i \tag{2.26}$$

where $\mathbf{P}_i$ is the polarization of i-th region α_i is its polarizability.

Because of the *superposition principle* the local electric field is the sum of the incident radiation plus the contribution of all the other excited volumes

$$\alpha_i^{-1}\mathbf{P}_i = \mathbf{E}^{\text{inc}}(\mathbf{r}_i) + \sum_{j\neq i}\mathbf{A}_{ij}\mathbf{P}_j \tag{2.27}$$

where $\mathbf{A}_{ij}$ is a 3x3 linear operator which maps the contribution of the polarization vector of j-th region to the local electric field at region i.

Supposing that the scattering particle has been divided in n polarizable volumes, equation 2.27 represent a linear system of n vector equations where the polarization state $\mathbf{P}$ is the unknown. Once equation 2.27 has been solved it is possible to compute the scattered field in any location of the space and thus also the scattering properties of the particle.

DDA is a *quasi-exact* technique in the sense that the formulation of the DDA actually solves the scattering problem for a cluster of polarizable regions. The accuracy of DDA, in solving actual scattering problems, depends on how well the discrete representation of the scatterer suites the real morphology of the scattering particle. Aiming to ensure the accuracy of DDA, it is recommended to set the size of the dipoles d to be small compared to the wavelength of the radiation inside the particle. The condition $|n|kd < 1$ (Zubko et al., 2010) is commonly adopted as a general "rule of thumb" for this purpose.

The system of n vector equation can be simplified into a system of $3n$ scalar equation which can be solved using standard linear algebra algorithms. Gaussian elimination would ensure an accurate solution, but it comes with a computational cost of $O(n^3)$. Iterative solving methods reduce the computational complexity to $O(n^2)$ allowing modern computers to calculate the scattering properties of small ice crystals at microwave frequencies with DDA. Goodman et al. (1991) note that the DDA matrix-vector products takes the form of a three-dimensional convolution and thus it can be accelerated using a fast Fourier transform (FFT) algorithm (Frigo and Johnson, 2005). The total computational cost of the FFT-DDA method is $O(N\log N)$ where N is now the number of cubic lattice discrete space with pace d that encloses the scattering particle.

The FFT-DDA algorithm allowed to compute the scattering properties of centimeter-sized particle at microwave frequencies. The computational advantage of the FFT-DDA also comes with some drawbacks: the cluster of dipoles must be defined in a regular grid; and "void" dipoles must be included in the scattering problem. The last requirement could be wasteful in case of large sparse aggregates are investigated and non-FFT formulation could be preferred.

Snowflakes and ice crystals are complex objects and as such present natural applications for the DDA. It is worth to mention that DDA is not the only possible scattering algorithm for complex shaped particles. Other methods capable of solving the scattering problem for

arbitrarily shaped particles have been used to model snowflakes: Ishimoto (2008) used the finite difference time domain (FDTD) method (Taflove and Hagness, 2005), while Botta and Aydin (2010) used the generalized multiparticle Mie (GMM) method.

2.2.3 Dielectric properties of liquid and frozen hydrometeors

The dielectric properties of ice and water are of prominent importance for the remote sensing of precipitation. In fact, the absorption coefficient of a substance is directly connected to the imaginary part of its refractive index and the scattering phenomena are related to changes in the real part of the refractive index of media. Uncertainties of radiative transfer computations have often been limited by the insufficient accuracy of dielectric properties databases (Matzler, 2006). The frequency and temperature dependence of ice and water dielectric models used in this study are shown in figure 2.5 and 2.6.

For liquid water the dielectric model of Meissner and Wentz (2004) is used. This dielectric model is accurate for microwave frequencies ranging from 1 to 100 Ghz and for temperatures up to 30 °C. For calculations made up to 300 Ghz the database of water dielectric properties measurement by Ellison et al. (1996) is used instead. Water interacts strongly with microwave radiation. The real part of the refractive index ranges from 3 to 6 and the imaginary part is of the same order of magnitude.

For the dielectric properties of ice we use the formula from Warren and Brandt (2008) which is accurate for microwave frequencies ranging from 10 kHz to 1000 GHz. The real part of the refractive index of ice does not depend on frequency in the microwave region and is only slightly dependent on temperature. Ice is also one of the most transparent media at microwave with a very low dielectric attenuation; the imaginary part of its refractive index is in fact $O(10^{-3})$.

Effective medium approximation

Many methods of computational electrodynamics (e.g. Rayleigh approximation, Mie theory, TMM) assume that the scattering particle is constituted of homogeneous material. Some hydrometeors are made of different substances within the particle model (e.g. ice and air for snowflakes; ice, water and air for melting snowflakes). Such particles should be modeled with an equivalent object composed of a single *effective medium*, whose dielectric properties are such that they would produce the same electromagnetic effects of the real particle. There are various formulations in scientific literature regarding how this effective medium approximation (EMA) should be calculated (Bohren and Battan, 1980; Sihvola, 1989).

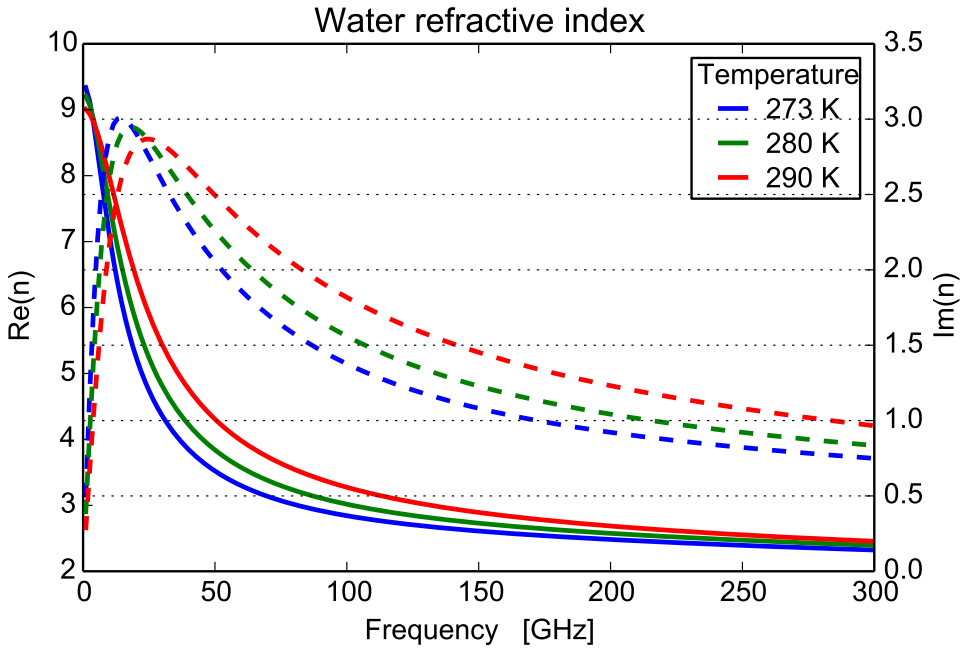

Fig. 2.5 Water refractive index as a function of frequency for different temperatures. Solid lines are the real part of the refractive index and dashed lines are the imaginary part

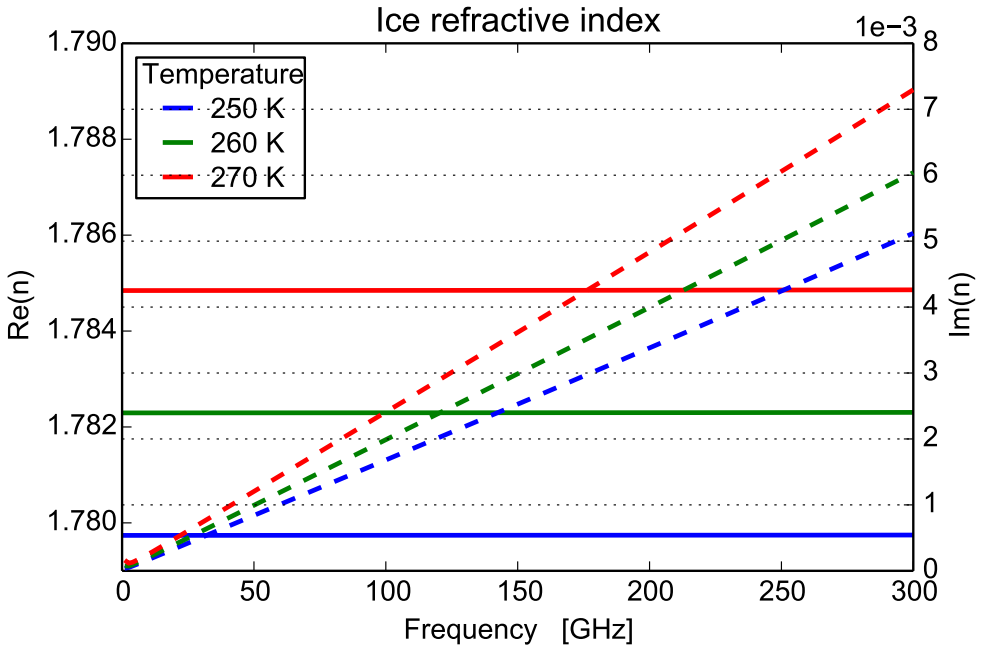

Fig. 2.6 Ice refractive index as a function of frequency for different temperatures. Solid lines are the real part of the refractive index and dashed lines are the imaginary part

One of the most commonly used EMA is Maxwell-Garnett (MG) formula (Maxwell Garnett, 1904). MG formulation uses the *Clausius-Mossotti* relation to solve the problem of mixing materials with different dielectric properties assuming that one component is present as small inclusions in the other component, referred as the matrix. The assumptions behind the MG formulation suggest that it is only valid when the inclusion material represents just a small fraction of the composite particle. The MG mixing formula is

$$f_i \frac{\varepsilon_i - \varepsilon_m}{\varepsilon_i + 2\varepsilon_m} = \frac{\varepsilon_{eff} - \varepsilon_m}{\varepsilon_{eff} + 2\varepsilon_m} \tag{2.28}$$

where ε_i and ε_m are the relative dielectric constant of the inclusion and matrix material respectively ($\varepsilon = n^2$); f_i is the volume fraction of inclusion and ε_{eff} is the relative dielectric constant of the effective medium.

The MG relation is not symmetric with respect to the selection of the inclusion and the matrix, meaning that the result depends on how the two material are chosen. The EMA of Bruggeman (1935) is symmetric with respect to the choice of materials 1 and 2, and is given by

$$f_1 \frac{\varepsilon_1 - \varepsilon_{eff}}{\varepsilon_1 + 2\varepsilon_{eff}} = (f_1 - 1) \frac{\varepsilon_2 - \varepsilon_{eff}}{\varepsilon_2 + 2\varepsilon_{eff}} \tag{2.29}$$

There is no obvious reason to prefer one EMA than another. However, if one component constitutes the large majority of the mixture, the different symmetric EMA formulations give generally similar results and the asymmetric MG relation is consistent with respect to the symmetric ones if the minority component is treated as the inclusions and the majority component as the matrix (see figure 2.7).

Johnson et al. (2012) tested different EMA for modeling snowflakes microwave properties and proved that the simulation of snow scattering properties is not sensitive to the choice of the dielectric mixing formula, provided that one considers ice as the inclusion in an air matrix when Maxwell-Garnett formulation is adopted. Otherwise, the reversal of the roles of ice and air leads to non negligible changes in both the real and imaginary part of the calculated effective refractive index and a significant change in both microwave brightness temperature and radar reflectivity simulated.

2.3 Interpretation of radar signal

Radars observe their targets by transmitting pulses of microwave radiation and measuring the power of the received echoes. The return signal of a weather radar depends on the number, size, shape and composition of the hydrometeors in the observed volume. By

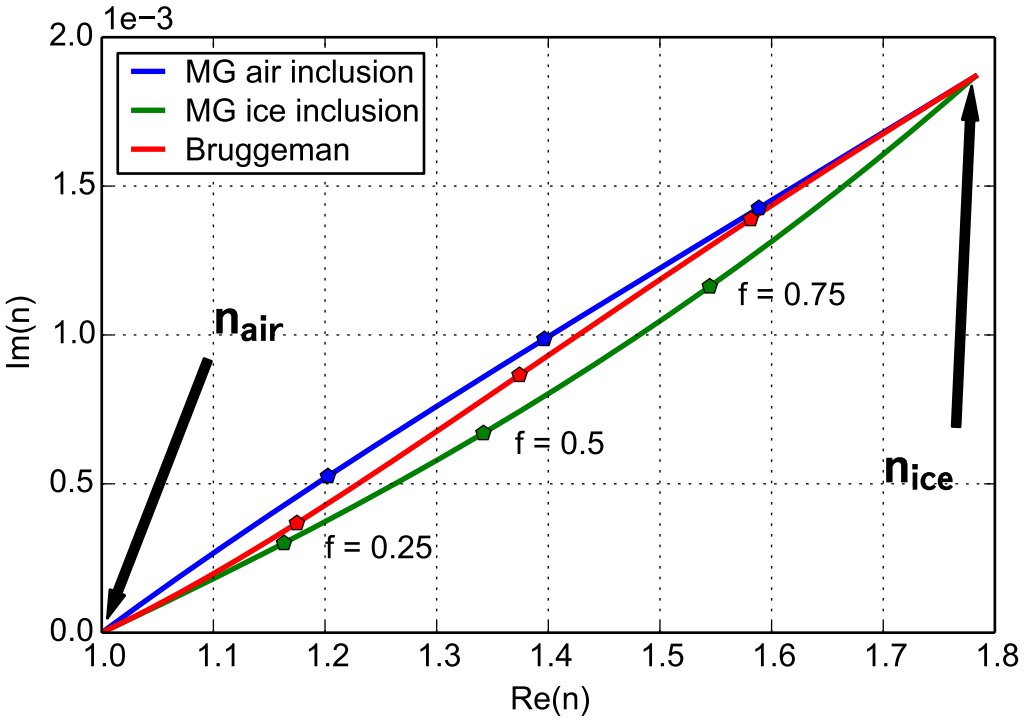

Fig. 2.7 Comparison of Bruggeman effective medium approximation with the two Maxwell-Garnett dielectric mixing rules. The comparison is carried on for mixture of ice and air at 94 GHz. Note the two different definitions of Maxwell-Garnett mixing considering respectively air inclusions in ice matrix and ice inclusions in air matrix. In the air refractive index $(1 + \imath 0)$ is in the bottom left corner and the volume fraction of ice is increasing parallel to each curve. The different mixing formulations match at the refractive index of pure ice $(1.77 + \imath 1.8e-3)$ in the top right corner of the graph. Markers show the location of ice volume fraction equals to 25%, 50% and 75%.

integrating the calculated scattering properties over measured particle size distributions, meteorologist look for relations between reflectivity and precipitation rate. Modern weather radars include many measuring capabilities which have been developed in order to further constrain the relations between physical parameters of precipitation and radiative quantities. These new measuring capabilities include polarimetry, doppler spectra and more recently also multifrequency analysis. This section introduces the general concepts of radar measurement; a comprehensive view of the topic can be found in Bringi and Chandrasekar (2001).

2.3.1 Radar reflectivity

Weather radars were first employed for the detection and quantification of rainfall. Raindrops at S and C band are can be considered as Rayleigh scatterers, thus the expected radar echo

Table 2.1 Summary of characteristics of the principal microwave bands used in radars

Band	frequency range	wavelength range
S	2 - 4 GHz	7.5 - 15 cm
C	4 - 8 GHz	3.75 - 7.5 cm
X	8 - 12 GHz	25 - 37.5 mm
Ku	12 - 18 GHz	16 - 25 mm
Ka	26 - 40 GHz	5 - 11 mm
W	75 - 110 GHz	2.7 - 4 mm

intensity is proportional to the sum of the sixth powers of the diameters of the raindrops in the measurement volume. For this reason the radar *reflectivity Z* is defined as the sixth moment of the drop size distribution

$$Z = \frac{1}{V_{radar}} \sum D_i^6 = \int_{\min(D)}^{\max(D)} N(D) D^6 \, dD \tag{2.30}$$

In the general case of possible non-Rayleigh scatterers, the *equivalent reflectivity factor* Z_e is defined such that it would match the definition 2.30 in case of Rayleigh scatterers (equation 2.16)

$$Z_e = \frac{\lambda^4}{\pi^5 |K_w|^2} \int_{\min(D)}^{\max(D)} \sigma(D) N(D) \, dD \tag{2.31}$$

where λ is the wavelength, and $\sigma(D)$ is the average radar backscattering cross section of particles of size D. $K_w = (n_w^2 - 1)/(n_w^2 + 2)$ is the the water *dielectric factor* in which n_w is the complex refractive index of water.

In fact, at shorter wavelengths, commonly used by space-borne radars (table 2.1), the Rayleigh approximation breaks down. The equivalent reflectivity factor is also different from Z for frozen hydrometeors and mixed-phase particles due to the dielectric constant of ice being different from that of water.

Since the scattering cross section is strongly dependent on particle size, the measured reflectivities span over 10 orders of magnitude, therefore the reflectivity factor is typically presented in logarithmic units of dBZ as $10 \log_{10}(Z_e/Z_0)$, where $Z_0 = 1 \; mm^6 m^{-}3$.

Even in the most simple case of the Rayleigh regime, the dependence of the reflectivity on the the water content or the precipitation rate is not straightforward. Integral quantities such as reflectivity, precipitation rate and mass content are integrated over the particle size distribution which exhibit large variability among different geographical locations and weather conditions. This fact dramatically limits the accuracy of the precipitation rate

estimate through radar retrieval because, different PSDs, and thus precipitation rates, can give the same radar reflectivity.

Historically, this problem has been addressed looking for empirical correlations between precipitation rate and radar reflectivity. Starting from Marshall and Palmer (1948) for rain and Gunn and Marshall (1958) for snow, relations in the power-law form of $Z_e = \alpha R^\beta$ have been proposed by numerous authors. These relations are correct just on average, and the constants α and β depend on the measurement's location as well as the current weather conditions, in particular the distinction between stratiform and convective precipitation (Atlas et al., 1999).

Empirical snow rate estimation formulas exhibit more variability than those for rain (see Sekhon and Srivastava (1970); Smith (1984), among many others). Furthermore the random variability around the average relation is larger. Regarding the precipitation rate estimation for snowfall, the uncertainties are even greater than with rain because of the intrinsic variability in the of snowflakes' shape, density and aspect ratio.

2.3.2 Dual-polarization and doppler measurements

The dual-polarization concept have been introduced by Seliga and Bringi (1976) and has now reached large popularity within the operational radar community (Huuskonen et al., 2014).

Dual-polarization radars emits (and receive) simultaneous or alternate pulses of radiation in the two orthogonal polarization direction (vertical and horizontal). The basic idea behind the dual-polarization measurements is that hydrometeors falling attitude is related to their shape and hydrometeors shapes is related to the particle size.

The first polarimetric quantity introduced is the so called *differential reflectivity* Z_{dr} which is simply the ratio between the received signals at the two distinct polarization and is generally expressed in dBZ

$$Z_{dr} = 10 \log_{10} \frac{Z_{hh}}{Z_{vv}} \tag{2.32}$$

Being the ratio between horizontal to vertical copolar reflectivities Z_{dr} is not dependent on particle number concentration and is directly related to the oblateness of particles horizontal projections. It has been found that small raindrops are nearly spherical and their aspect ratios increases with the size of the particle (Thurai et al., 2007).

Figure 2.8 show the ratio of backscattering cross section at horizontal to vertical polarization as a function of drop diameter. It is shown that this ratio correlates well with drop diameter in the Rayleigh scattering regime. On the other hand, when Rayleigh approximation

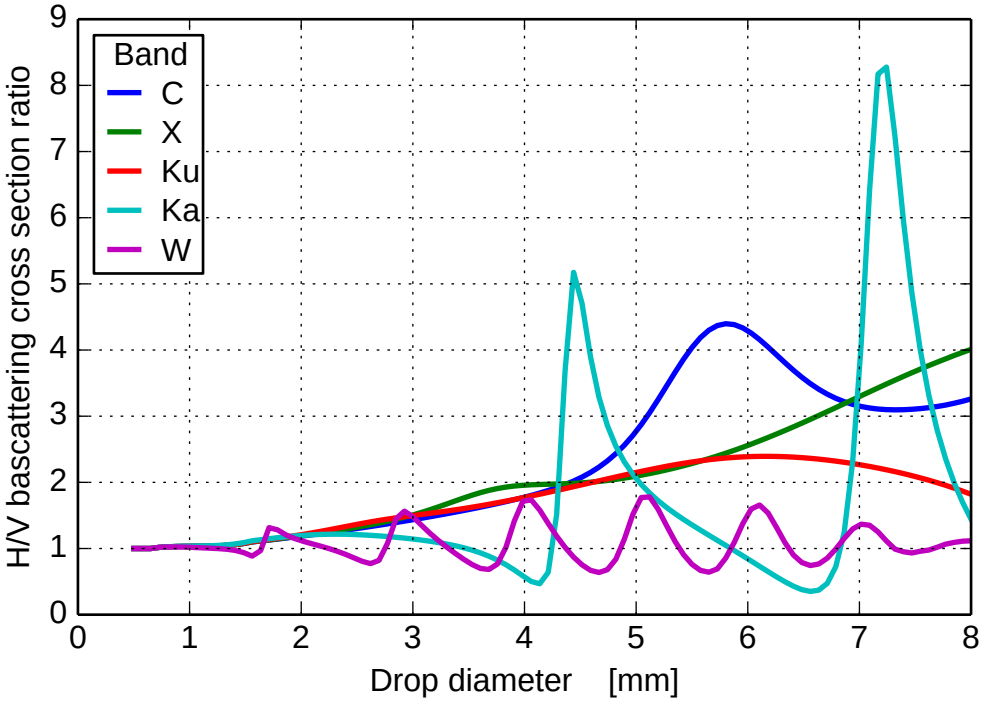

Fig. 2.8 Ratio between radar backscattering cross section at horizontal to vertical polarization for different radar bands. Raindrop diameter ranges from 0.5 to 8 millimeters and aspect ratio changes with the diameter according to Thurai et al. (2007).

is not valid, the Mie resonance behavior give raises to large uncertainties in the interpretation of differential reflectivity.

Giving the size information provided by Z_{dr}, the differential reflectivity is often used in combination with Z_e to constrain quantitative precipitation estimations with formulas of the form $R = \alpha Z_e^{\beta_1} Z_{dr}^{\beta_2}$.

The *specific differential phase* K_{dp} gives the rate of change in the relative signal phase of the signals in the two distinct polarizations. It usually expressed in $^{\circ}\mathrm{km}^{-1}$ and is given by.

$$K_{dp} = \frac{180\lambda}{\pi} \int_{D_{min}}^{D_{max}} \Re \left[S_{hh}(\hat{\mathbf{n}}^{\mathbf{sca}} = \hat{\mathbf{n}}^{\mathbf{inc}}, D) - S_{vv}(\hat{\mathbf{n}}^{\mathbf{sca}} = \hat{\mathbf{n}}^{\mathbf{inc}}, D) \right] N(D) dD \tag{2.33}$$

where $S_{hh,vv}(\hat{\mathbf{n}}^{\mathbf{sca}} = \hat{\mathbf{n}}^{\mathbf{inc}}, D)$ represent the diagonal element of the amplitude scattering matrix at given size D and forward scattering direction.

K_{dp} is sensitive to both particles average size and number concentration. It is used to correct radar reflectivity from attenuation and for constrained quantitative precipitation estimation in combination with Z and Z_{dr}. K_{dp} based precipitation measurements are

particularly popular for the estimation of heavy rainfall since K_{dp} accuracy is not degraded by radar attenuation.

Due to the lower refractive index of ice with respect to water snow radar signals are generally weaker than those of rain. Moreover there is no obvious relation between snowflake size and shape and the inhomogeneous internal structure of snowflakes further complicates snow polarimetric properties. Therefore, the polarimetric signature of snowfall is weaker and more ambiguous with respect to that of rainfall. Nonetheless, wet snow exhibit a pronounced polarimetric feature called *melting layer* which is used to distinguish radar echoes from liquid and frozen hydrometeors (Giangrande et al., 2008).

The *correlation coefficient* (ρ_{hv}) measure how the vertical and horizontal polarized return signal, within a radar volume, correlates each other.

$$\rho_{hv} = \frac{\int_{D_{min}}^{D_{max}} S_{hh}(D) \cdot S_{vv}^{*}(D) N(D) dD}{\sqrt{\int_{D_{min}}^{D_{max}} \sigma_{hh}(D) N(D) dD} \sqrt{\int_{D_{min}}^{D_{max}} \sigma_{vv}(D) N(D) dD}} \tag{2.34}$$

Non-meteorological echoes such as birds and insects have complex and highly variable shapes which result in the horizontal and vertical pulses behaving very differently and thus ρ_{hv} is expected to be smaller than 0.9. For meteorological echoes that have complex shapes or mixed-phase the correlation coefficient ranges from 0.85 to 0.95. For meteorological echoes that are fairly regular in shape and size ρ_{hv} usually is larger than 0.97.

Doppler radar

Another source of information is the dependence of the frequency of the radar return signal on the along-beam targets' velocity. The measuring technique is based on the principle of Doppler frequency shift. Generally for ground-based scanning weather radar the velocity information is used to infer wind speed and to detect ground clutter.

On the other hand, vertical pointing radar can use their Doppler capabilities to measure the fall velocity spectra. Since the vertical fall speed is related to the microphysical properties of precipitating particle as well as vertical air motion Doppler measurements constitutes an important source of information for quantitative precipitation estimation (Kollias et al., 2002; Shupe et al., 2004; Wakasugi et al., 1986).

Errors in radar measurements

Being an electronic measurement device the radar suffers of energy dissipation inside its circuits and waveguide, thus it needs to be calibrated against known energy sources (e.g. the sun) or calibrated targets. Technical parts of radar systems also degrade their quality

with time and are then subjected to calibration drift. For the calibration of the receiver the correlation between Z, Z_{dr} and K_{dp} in case of rainfall can be used for absolute calibration of the radar system employing the so called *self-consistency theory* (Gourley et al., 2009).

As stated before the radar signal is attenuated when traveling through precipitation. The magnitude of attenuation is usually measured in units of dB per kilometer (*specific attenuation* A_i. The integration of A_i along the optical path of the radar beam yields the path-integrated attenuation (PIA). PIA could be estimated by the measurements of precipitation intensity (Z_e,K_{dp}), but the quality of these measurements degrades because of the attenuation, thus the attenuation correction becomes unstable as the attenuation increases.

A wet radome[3] can be another source of systematic attenuation. Since absorbing matter also emits radiation due to the Kirchhoff's law (see section 2.1.1), radome attenuation can be detected and eventually corrected measuring the variations in the radar noise level, i.e. the energy returned to the radar antenna in absence of radar emitted pulses (Thompson et al., 2011).

Random errors arises from the electronic noise of the receiver. Usually this error is mitigated by averaging the received signal over several radar pulses. The noise level is then lowered by increasing the *pulse repetition frequency* (PRF) or pulse width, but this also affect the maximum unambiguous range of the radar and the maximum unambiguous measured Doppler velocity; the choice of the PRF value is usually the result of a trade off between these various requirements for the radar system.

2.3.3 Multiple frequencies

The simultaneous use of two or more radars at different wavelengths has been investigated as another method to constrain precipitation rate estimates.

First attempts at dual-frequency retrieval algorithms were based on the differential attenuation characteristics of precipitation at different wavelengths (Eccles and Mueller, 1971). Similar to precipitation estimate techniques based on differential phase shift of polarimetric radars, these methods derive the rain rate from the difference of the radar signal attenuation levels at two frequencies. Respect to the dual-polarization technique this estimate can be employed also on vertically pointing radars carried on satellite missions.

Another multiple-frequency technique involves the so called *dual-frequency ratio* (DFR) (Meneghini et al., 1992) which is the ratio of measured reflectivities at two distinct frequencies. These methods generally require one of the wavelengths to be out of the Rayleigh regime. The basic property of DFR is that it is not dependent on the particle number concentration

[3]Radome is portmanteau of radar and dome

of the PSDs, but just on the shape of particles. Being a multiplicative constant, the particle number concentration exit the integral sign of equation 2.31 and cancels out in the ratio. Then the DFR yields information about the average size of precipitating particles. Similarly to Z_{dr} and K_{dp} based measurements the information on the particle size can be used as a constrain to reduce the uncertainties in the precipitation estimation.

The main advantage of dual-frequency estimation respect to polarimetric study is that DFR is directly connected to the average size of the particles whereas the polarimetric properties are related to the shape of the scatterers. More precisely: DFR does not assume any relation between the size and the shape of the particles. Thus, DFR can be used to investigate the microphysical properties of complex shaped hydrometeors such as snowflakes and ice crystals through remote sensing techniques (Kneifel et al., 2011; Löhnert et al., 2011; Matrosov, 1998).

For ground-based radars dual-frequency methods are still just a research tool. Regarding space-borne mission with the launch of the GPM-core satellite dual-frequency estimation techniques has become operational for precipitation retrieval. For this reason dual frequency based algorithms which combines both DFR and differential attenuation has received recently more attention (Liao and Meneghini, 2005; Liao et al., 2005).

Chapter 3

Snowflake modeling

The remote sensing of snowfall require both a detailed and validated microphysical description of snow particles and the simulation of their electromagnetic properties which allows to relate the physical properties of interest to the measured variables like radar reflectivity. The snowflake formation is affected by the cloud vertical distribution of water, particle size distribution and thermodynamic conditions, and has a direct impact on snow particle size, shape, mass which in turn control the flake fall speed and therefore the precipitation rate. The snow microphysics is then directly connected to parameterizations implemented in numerical weather predictions, climate simulations and remote sensing algorithms. Snow particle formation also control the snowflake shape which has a significant impact on particle single scattering properties. The snow particle modeling is then of a prominent importance in the simulation of snow radiative characteristics and their measurements.

The scattering calculations require the description of realistic target shapes. The unlimited variety of snowflake morphologies is a known point of popular wisdom. Talking about snowflakes it is common across multiple cultures to say: "There is no one like another". Snowflake shape varies over a wide range of morphologies from small pristine ice crystals to large aggregates. Single crystals could be classified in a limited number of shapes (Magono and Lee, 1966) and pristine habit could be predicted knowing the thermodynamic conditions (see figure 3.1) that lead to their initial diffusional growth (Pruppacher and Klett, 1997). Snowflake shapes becomes much more difficult to predict when snow accretion starts to be dominated by aggregation, riming, break up and splintering. Aggregates' shapes are irregular (figure 3.2) and the complexity of their description rises fast (Jiusto and Weickmann, 1973).

The description of the microphysical properties of mixed-phase particles is even more complicate. The scientific literature treating the morphological and microphysical characterization of melting snowflakes is poor. Nonetheless the atmospheric layer where melting

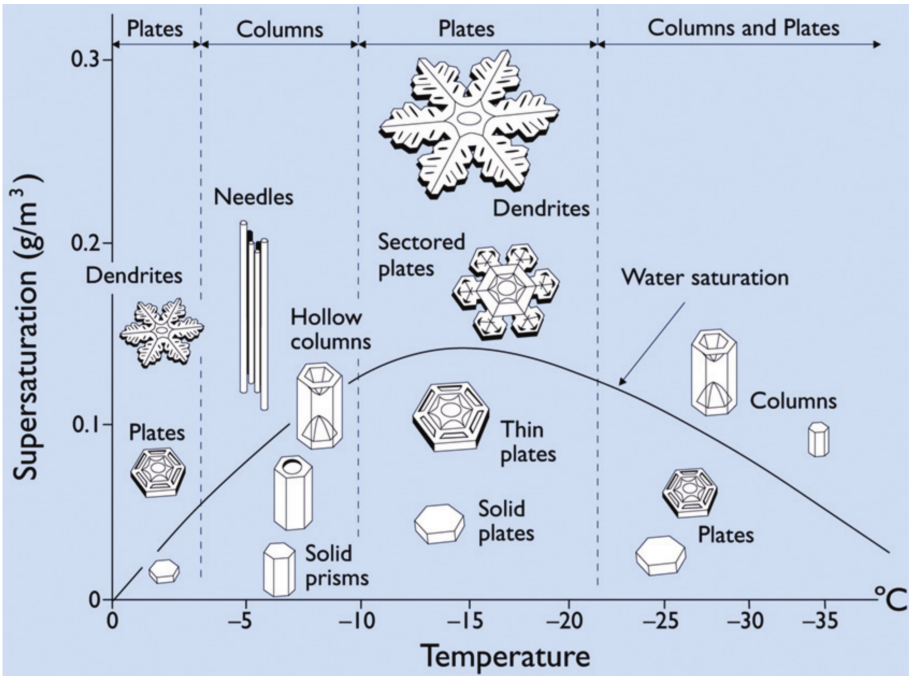

Fig. 3.1 The types of snowflakes that form in different temperature and humidity conditions. Image extracted from (Libbrecht, 2005).

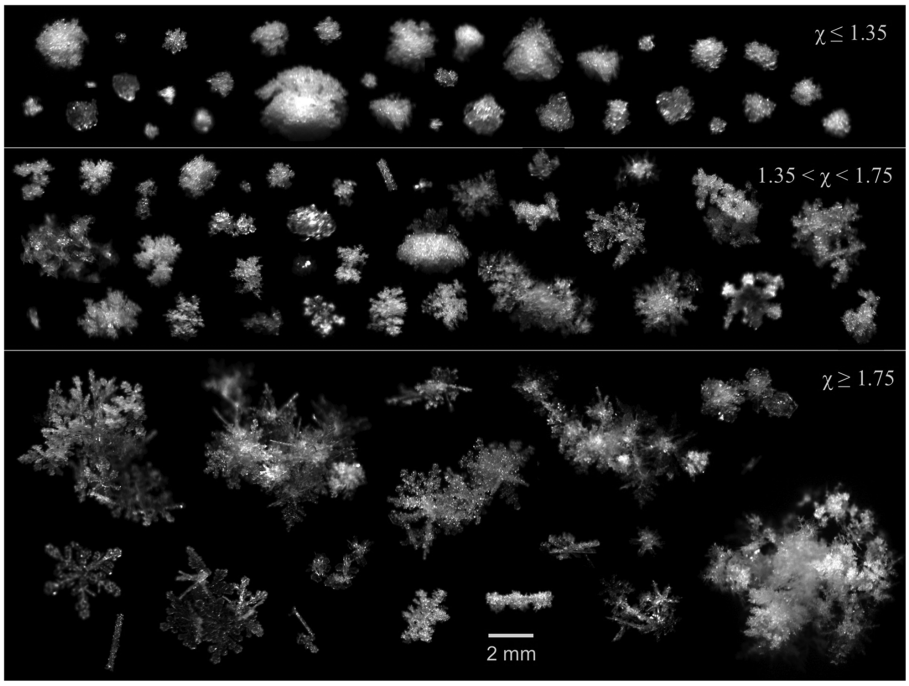

Fig. 3.2 High detailed images of falling snowflakes taken by the MASC instrument (Garrett et al., 2012). The classifying χ parameter is a measure of the particle morphological complexity.

processes takes place exhibit distinctive radiative features which are of prominent interest for the remote sensing of precipitation.

A microphysically based algorithm (named Snow Aggregation and Melting SAM) that models snowflakes composed of a collection of pristine crystals by simulating a random aggregation process is presented. The aggregation phase of the model leverages the most updated scientific information available on the microphysics of snow aggregation (Westbrook et al., 2004a). SAM combines together pristine crystals with multiple dimensions to derive complex aggregates constrained to size-mass relationship obtained by data collected from in situ measurements. The model also simulates the melting processes occurring for environmental temperatures above 0°C and thus define the mixed-phase particles structure.

3.1 Aggregation process

Ideally, one would like to follow the spatial and temporal evolution of any individual particle in a cloud allowing for a precise description of the dynamical and statistical evolution of the ice particle population, but this fine resolved model has many practical difficulties. The typical particle number concentration in ice clouds is around 10^5 m^{-3}, therefore the following of each individual particle requires memory and computational costs that largely exceed the practical available computer resources. Many attempts to construct simplified snowflake aggregation theories has been performed aiming to describe the general and essential physics of the aggregation problem.

While being complex, the structure of aggregate snowflakes exhibit qualitative similarities among the various particles (Westbrook et al., 2004b). In situ observations indicate that aggregate snowflakes are fractals with a particular *fractal dimension* d_f (Ishimoto, 2008; Maruyama and Fujiyoshi, 2005).

The fractal dimension is directly connected to the mass-size relationship. For a general fractal object in the three dimensional euclidean space the particle mass m relates to the linear dimension through a power law

$$m(D) = \alpha_m D^{d_f} \tag{3.1}$$

where $d_f < 3$ and for an aggregated particle the coefficient α_m depends on the shape and size of the monomers that constitute the aggregate. Analogously the particle density decreases with the size as

$$\rho(D) = \alpha_\rho D^{d_f - 3} \tag{3.2}$$

The power law decrease of the snowflake density with the size is confirmed by numerous field studies (Brandes et al., 2007; Fabry and Szyrmer, 1999; Heymsfield et al., 2004; Locatelli and Hobbs, 1974; Magono and Nakamura, 1965; Muramoto et al., 1995)

The fractal properties and the decrease with the size of the snowflake density are peculiar characteristics of the aggregation process. When an aggregate form through the collection of similar-sized parts its overall volume increases as D^3 whereas its mass increase with the number of particles that actually attach each other. Even with the most optimistic case of small equally sized monomers sticking together it is very unlikely that they would fill the entire volume occupied by the growing particle conserving the density of the single monomers as the aggregate size increases. As the aggregation process proceeds, the particle starts collecting fluffier and larger aggregates, reducing the packing efficiency of the aggregation mechanism and thus the particle density gets smaller and smaller. For this reason, not only snowflake density decreases with size, but it is also expected that density in the inner portion of snow aggregate is greater then the exterior part of it.

This somewhat universal properties of snow aggregates provides guidelines for snowflake's model design. Some attempts to model aggregated particles that imitate the fractal characteristics of the snowflakes have been proposed to serve as targets for scattering computations. Hopefully the most interesting microphysical and radiative properties of snow will be found to depend only on the general morphological characteristics of snowflakes and the effects of the particular micro-structural features will vanish when averaged over large populations of ice particles.

Maruyama and Fujiyoshi (2005) proposed a collision-coalescence process for modeling particle aggregates. Their particular model combines a dynamical collision model with a Monte Carlo method (Gillespie, 1975) to select the couple of particles to collide. All constituent particles are low density spheres, i.e. they are considered to be spherical particles composed of a mixture of ice and air. This last assumption simplifies a lot the dynamics of aggregation, but it is not consistent with the fact that snow aggregates are made of ice crystals which resemble hexagonal prisms.

A different approach to model fractal snowflakes has been employed by Ishimoto (2008) to simulate snow scattering properties with the finite difference time domain (FDTD) method. The aggregate construction is based on an iterative *finite subdivision method* which controls the particle growing at a constant and predefined fractal dimension. This method produce indeed realistic looking snowflakes, but it does not model the single ice pristine shapes and does not represent the expected radial distribution of mass density because the fractal dimension is kept constant while the particle is growing. Finally for fluffy particles (fractal dimension ranging from 1.8 to 2.2) it is also probable that, during the aggregate construction,

the particles divides into multiple disconnected clusters as a consequence of the domain subdivision.

Nowell et al. (2013) implemented an ad-hoc *diffusion limited aggregation* (DLA) method to construct snow aggregate model aiming at computing their scattering properties using DDA. The modified DLA technique uses idealized six-bullet rosettes as building blocks of the complex aggregate particle. This model is able to obtain aggregates with controlled physical properties such as mass, dimension and aspect ratio, but it uses a rather coarse and fixed lattice grid. Moreover the constituent crystals are highly simplified (the six-bullet rosettes are composed of just few cubic blocks and all shares the same spatial orientation with respect to the reference frame) and not realistic.

A physically based simulation of ice crystal aggregation was used to generate models of aggregate snowflakes. This algorithm constitutes the aggregation phase of the SAM model and it is based on concept of differential sedimentation (Westbrook et al., 2004a). In contrast with the DLA and the finite subdivision fractal methods, the differential sedimentation algorithm reproduce explicitly the process of aggregate formation by collision-coalescence of ice crystals. Differently from the Maruyama and Fujiyoshi (2005) algorithm this method uses realistically shaped pristine crystals and employs statistical constrains to drive the aggregate to follow predetermined mass-size relationships.

Differential sedimentation

The typical particle number concentration N of 10^5 m^{-3} results in a mean particle separation of $N^{-1/3} = 2.2$ centimeters. Considering that the order of magnitude of ice particle sizes in cloud is 1 millimeter, the mean free path of these particles is larger than $l = (N\pi D^2)^{-1} = 3.2$ m. The fact that the mean free path is much larger then the cloud mean particle separation allows the modeling of the collision events as a statistical process without considering the spatial or temporal dependence.

The first step of the aggregation model is to define the shape of individual crystals. In contrast with previous aggregation models which describes the single crystals as clusters of points (to be used in DDA scattering calculation) the SAM implementation makes use of geometrical objects defined as structures of vertexes, edges and faces. This definition of crystal's shape allows to modify the crystal orientation without loosing accuracy in crystal volume and mass. In order to use the aggregate models in DDA scattering computations, the crystal shape could be transformed in a cluster of equally spaced volume using a point in polyhedron algorithm, which allows to reuse the same snowflake shape at different resolutions of the cubic lattice grid.

Simple crystals like hexagonal columns, plates, bullet rosettes and droxtals can be then described by their geometrical shape taking into account the relative proportions of the crystal's structural lengths and their dependence with respect to the crystal size (Hong, 2007a; Um et al., 2015). More complex crystals like dendrites can be modeled using a cellular growth model (Reiter, 2005) and eventually simplified with a solid object that resemble the envelope of the dendritic crystal. In any case, the pristine ice crystals are considered to be composed of pure ice and the surfaces of their solid geometrical representation are assumed flat and free from roughness.

A representative sample of ice crystals size distribution is created from these monomers. The dimension of the crystals is determined according to in-situ measured PSDs. It is assumed that the ice crystals have random orientation in space. The aggregation of ice particles is then modeled with a step by step procedure.

The ice crystals aggregation is mainly due to the difference between the fall velocities of the ice particles (Heymsfield, 1972; Kajikawa, 1976, 1992). The model implement an estimate of the collision probability between any pair of particles Γ_{ij} which is expected to be proportional to the total impact cross section and the difference between the fall velocities of the couple of particles (i,j).

$$\Gamma_{ij} = \frac{\pi}{4}(D_i + D_j)^2 |v_i - v_j| \tag{3.3}$$

Given a particular PSD $N(D)$, the probability distribution of collision between a couple of particles (i,j) with sizes (D_i,D_j) is proportional to

$$P_{col}(D_i, D_j) = N(D_i) N(D_j) (D_i + D_j)^2 |v_i - v_j| \tag{3.4}$$

where all the constant coefficients have been omitted for seek of simplicity.

The model needs a parameterization of particle fall speed. It could be assumed that the ice particles falls at their terminal fall speed which is the equilibrium state of falling object at which the gravitational force equal the aerodynamic drag force F_d.

$$mg = F_d = \frac{1}{2}\rho_a A v_t^2 C_d \tag{3.5}$$

where ρ_a is the density of air, A is the particle's area projected perpendicular to the flow, v_t is the terminal fall velocity and C_d is the *drag coefficient* which depends on how the air flows around the falling object (i.e. the *Reynolds number* R_e).

The Reynolds number is defined as the ratio of momentum forces to viscous forces and consequently quantifies the relative importance of these two types of forces for given flow conditions. Large values of the Reynolds number identify the so called *inertial flow*

(also known as *turbulent flow*), which is characterized by eddies, vortices and other flow instabilities. In the turbulent flow regime the aerodynamic drag force is known to be a quadratic function of the Reynolds number. The inertial flow is opposed to the small R_e regime, namely the *viscous flow* (or *laminar flow*) where the viscous forces are dominant and is described by a smooth fluid motion. In the limit of a pure laminar flow the aerodynamic drag force vary linearly with the Reynolds number.

Since Reynolds number is dependent on the air viscosity and the falling particle morphology, deeply sophisticated models of the aerodynamic of falling snowflakes has been developed in order to derive snow microphysical properties (bulk density and area ratio) from fall speed measurements (Böhm, 1989; Mitchell, 1996; Mitchell and Heymsfield, 2005). One of these models will be employed in section 5.1.2, but for the purposes of snowflake modeling, there is no need of highly accurate terminal fall velocity models and following Westbrook et al. (2004a), a simple approximation of aerodynamic drag (which analytically approach the behavior of drag forces in the limit viscous and inertial regimes) is used.

The terminal fall speed is then given by

$$v_t \approx \frac{\nu}{r_g}\left(\frac{mg}{\rho_a \nu^2}\right)^{\chi} \tag{3.6}$$

where ν is the kinematic air viscosity and χ is a flow type parameter that ranges from 0.5 (inertial flow) to 1 (viscous flow).

Equation 3.6 requires a characteristic radius r_g of the particle to be provided in order to compute the terminal fall speed. The unique definition of size of non spherical objects is a difficult task. From hexagonal prism to large complex aggregates, there is no theoretical preference for any method defining the particle dimension. Particle size distributions could refer to any definition of size which usually depends on the measuring device. A practical and universal solution is to use the particle maximum dimension D_{max} and the SAM algorithm uses D_{max} when defines particles' size for PSD and geometrical cross section. Conversely, in the equation 3.6 the characteristic radius of the particle is set to be equal to the *radius of gyration* r_g, which is defined as the root mean square distance of the object's internal parts from its center of mass.

$$r_g = \sqrt{\frac{1}{V}\int_V |\mathbf{r} - \mathbf{r}_{\mathrm{cm}}|^2 d\mathbf{r}} \tag{3.7}$$

The radius of gyration has been chosen as characteristic dimension of the particle because it can capture some of the effects of the non-homogeneity of the modeled particle, making the expression 3.6 more consistent with the principles of fluid mechanics (denser particles have smaller radius of gyration and thus fall faster respect to fluffier snowflakes).

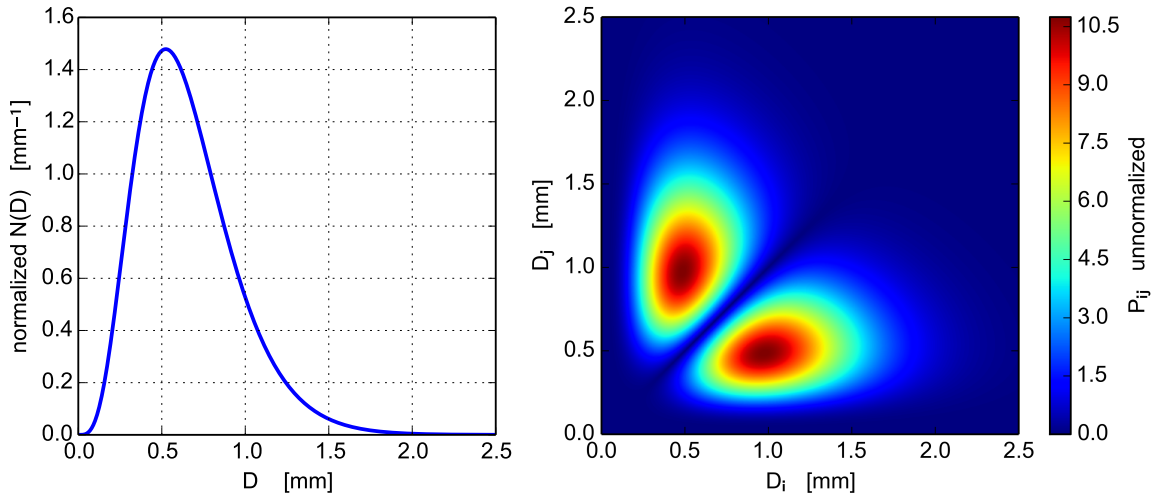

Fig. 3.3 Distribution of aggregation probability with the size of the aggregating particle for a typical stratiform cold cloud PSD (Heymsfield et al., 2013). On the left panel the normalized used for the calculation is shown. The right panel presents the result of the computation of collision probability distribution $P_{col}(D_i, D_j)$ for any couple of particles in the PSD.

From equation 3.6, fall speed is monotonically increasing with the particle size, thus the distribution of collision probability (equation 3.4) tends to favor the aggregation of the large particles with the smaller one due to their differential sedimentation rate. Figure 3.3 show the distribution of aggregation probability with the size of the aggregating particle for a typical stratiform cold cloud PSD (Heymsfield et al., 2013). It is shown that the most probable collision occurs between particles with size equal to 0.5 mm (the most common particle in the PSD) with larger particle with size equal to 1 mm. This model does not allow purely monodisperse PSD as initial condition because that would result in a null collision probability.

Collision coalescence

The aggregation phase of the SAM algorithm is completed by a dynamical simulation of the collision coalescence between pairs of particles. The collision sequence is described by four steps that are graphically represented in figure 3.4.

1. First, a Monte Carlo simulator select a couple of particles to be aggregated according to equation 3.3 using the *inverse transform sampling method*[1]. Specifically, the cumulative collision probability is obtained by calculating equation 3.3 for each pair of particles in the population and normalized by the sum of all collision probability $\Gamma_{i,j}$.

[1] Also known as *Smirnov transform* or *golden rule*

Then, inverse transformation sampling takes the result of a pseudo-random number generator which uniformly sample numbers between 0 and 1, and interprets it as a probability. The particular couple of particles to collide is selected matching the cumulative collision probability distribution with the random sampled probability.

2. The first of the two selected particles, here referred as *core aggregation particle* (CAP) is placed at the center of the reference frame. R_1 is the radius of the smallest sphere centered in the center of mass of the CAP that encloses the whole particle. The CAP is then randomly rotated around its three Cartesian axes (first panel of figure 3.4) simulating the random collision trajectory of the two particles.

   The second particle in the selected pair (the next adding particle, NAP) is randomly rotated around its axes. The radius of the smallest sphere enclosing it, hereafter noted as R_2, is calculated. The NAP is positioned above the CAP with its center of mass randomly placed in the area defined by a cross section of magnitude given by $\pi(R_1+R_2)$ and centered around the z axis. The NAP is afterward forced to fall until it touches the CAP. If the contact occurs, the two particles stick together and a new CAP is generated (second panel figure 3.4).

   If the particles do not touch each other, the two particles are returned to the population of aggregating particles and a new aggregation process is started until a contact occurs.

3. The radius of the minimum sphere enclosing the new CAP R_1, the new D_{max} (the diameter of the smallest sphere enclosing the whole particle) and the radius of gyration of the new cluster of particles are calculated (third panel, figure 3.4). The fall speed of the new CAP is calculated according to the aerodynamic model described by equation 3.6. The geometrical description of the aggregated particle is stored in a permanent file.

4. Once the CAP is returned to the population of particles, the distribution of collision probability is updated, another pair of aggregating particle is selected and the aggregation process starts again (fourth panel of figure 3.4).

The aggregate geometrical shape is converted to a cluster of equally spaced point to be used as input for DDA codes (generally a spacing of 20 μm has been used to meet the accuracy requirements of the DDA at microwave frequencies up to 200 GHz). The conversion to the volume element definition of the particle shape is performed applying a *point in polyhedron* algorithm (Lane et al., 1984) which allows to adjust resolution of the cubic lattice grid according to the accuracy requirements of the scattering study.

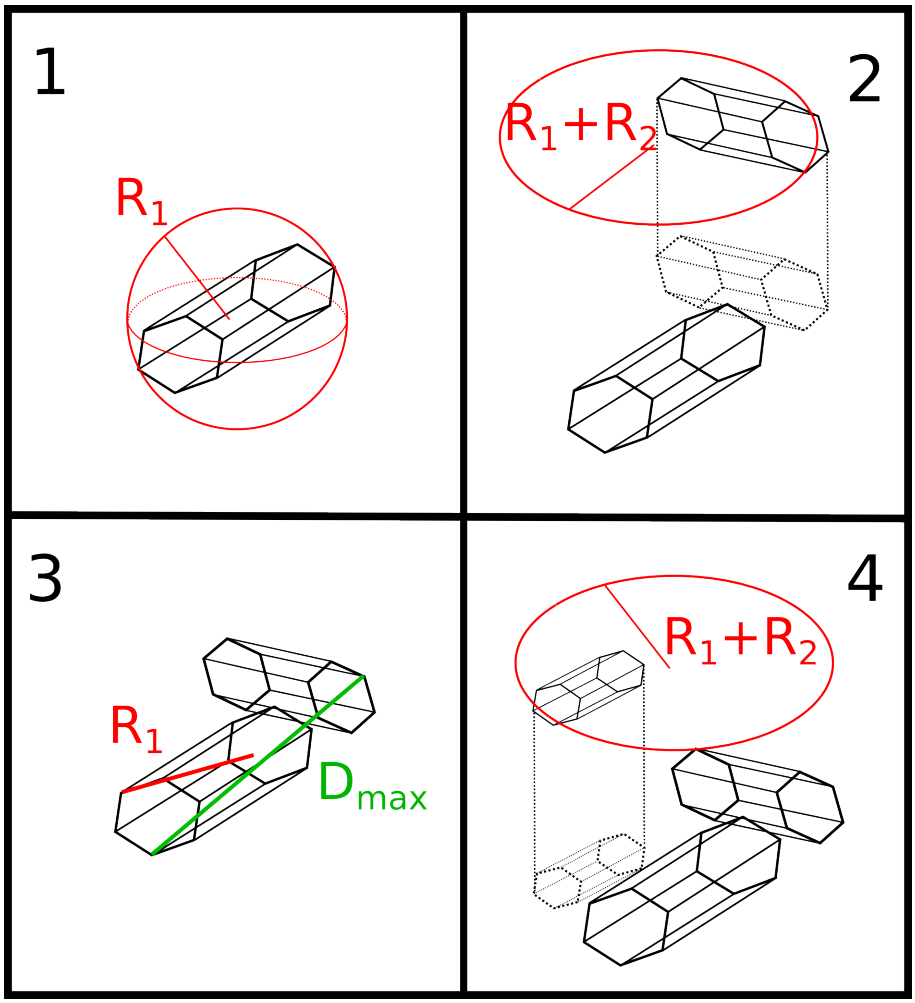

Fig. 3.4 The SAM collision scheme in four steps (from left to right). The geometrical properties of the aggregate, R and D_{max}, are plotted respectively with a red and a green line. In the second and fourth panel the total circular area containing the geometrical cross section of the joint CAP and NAP is shown

Point 2 of the collision process states that the falling trajectory of the NAP may miss the CAP because of the difference between the actual cross section of the two particles and the circumscribing circles that represent them. The fact that the CAP and the NAP may not collide modifies the size dependent collision probability (equation 3.3). It should be noted that in this context, the term "collision probability" is somehow misleading because the differential sedimentation process only accounts for particles whose centers of mass are going to approach at a distance shorter than $R_1 + R_2$ and are not supposed to actually collide with full certain. The term Γ_{ij} is more precisely referred as *probability of short range interaction* or, as it has been named in some literature, *rate of close approach*. The fact that the complex morphology of aggregates can cause two approaching particles to not collide does not change

the collision probability in a sensible way, and the more precise naming convention has been considered quite verbose for the scope of this modeling; for these reasons the more compact and direct name of *collision probability* has been preferred.

The *sticking efficiency*, i.e. the probability by which colliding particle adhere each other, has been assumed to be not dependent on the particle sizes. Therefore, the size dependent collision probability (equation 3.4) does not take into account the sticking efficiency. In support of this assumption, it has been observed that the probability of cohesion between two ice crystals depends more on crystal shape (Hosler and Hallgren, 1960) and environmental temperature (Lin et al., 1983) rather then particle dimension. Indeed the diverse chance of crystal bonding is to take into account when the aggregation model is applied to a population of crystals that considers multiple particle habits.

The CAP and the NAP are assumed to stick together rigidly at first contact. The realism of this assumption is questionable and depends on the shape of monomers and environmental temperature. The coalescence process at ice phase is still a matter of debate and many interpretations has been proposed, including pressure melting, electrical attraction (Dash et al., 2006) and quasi-liquid layers on ice surfaces (Sazaki et al., 2012). Anyway, aggregate snowflakes with very delicate connections between the crystals are commonly seen in nature (Garrett and Yuter, 2014) and thus the contact-stick assumption is considered reasonable for snowflake modeling. Examples of modeled aggregate snowflakes are shown in figure 3.5.

The SAM model also assumes that the aggregating particles are randomly oriented in space. It is well known that in case of inertial flow, pristine ice crystals tends to fall with their maximum projected surface perpendicular to the airflow direction (Klett, 1995). Cloud electrical fields could also align the ice crystals to preferential directions (Foster and Hallett, 2002). However, the collision process itself modifies the orientation of the falling particles and recent snow aggregates observations suggest that the distribution of particle orientation of falling snow is broad and difficult to predict (Garrett et al., 2015).

The SAM aggregation model has been under continuous development. The version presented in this chapter is the most advanced one. A slightly different algorithm has been used to model the snow aggregates analyzed in chapter 4. In that model, instead of considering the aggregation process of a large population of ice particles, one cluster is defined as the growing aggregate and ice monomers are added one at a time (continuous collection of pristine crystals). This method has been used because it allows an enhanced control on the particle radial distribution of mass. However, the continuous collection process does not allows to collide complex aggregates with each other causing large discrepancies in the modeled snowflakes porosity. The most advanced version of the SAM aggregation model reproduce the most realistic behavior of snowflake clustering.

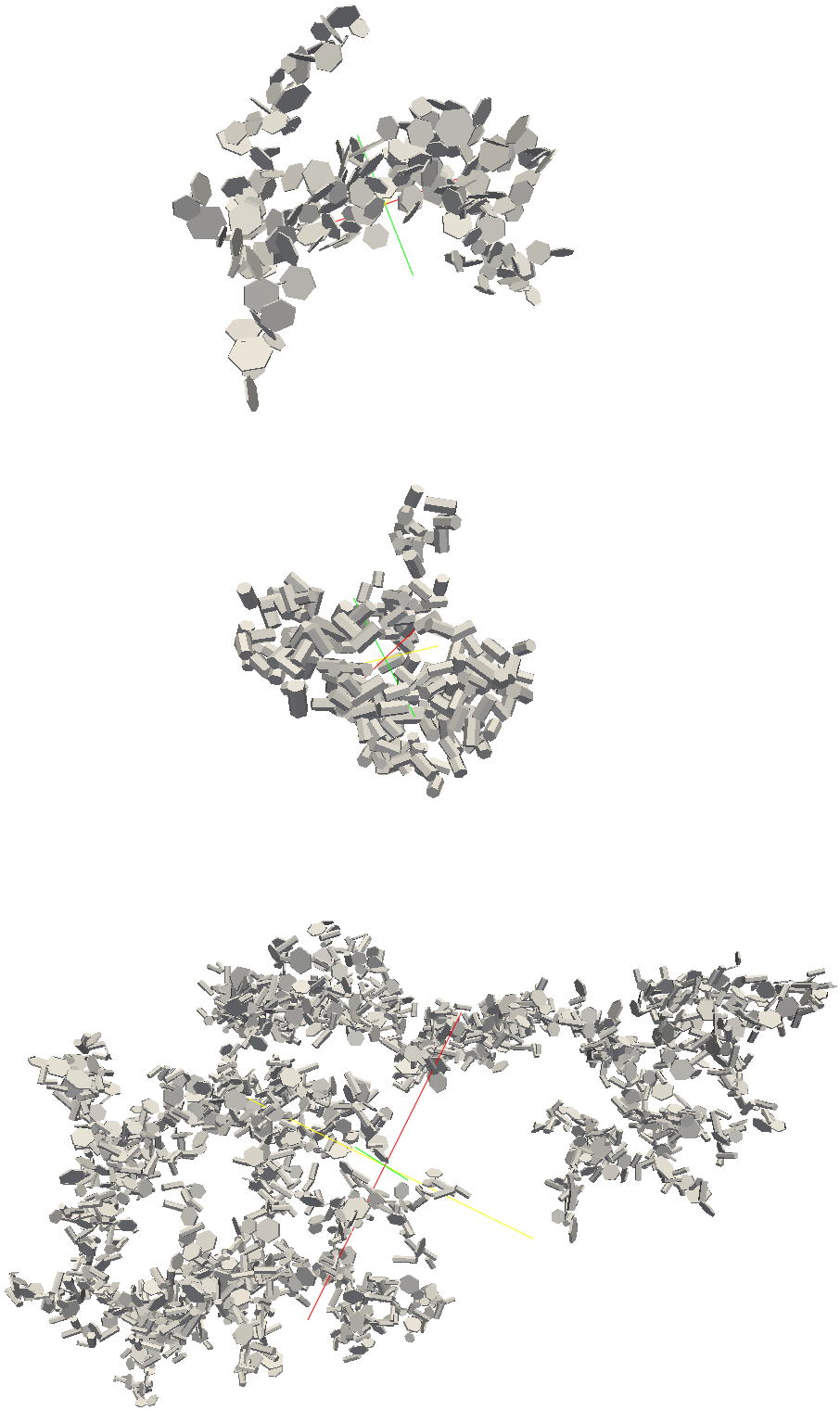

Fig. 3.5 From top to bottom: an aggregate of plates, columns and a mixture of plates and columns; the snowflakes are modeled with the SAM algorithm. The aggregate images are rendered using the ParaView software (Ahrens et al., 2005).

3.2 Melting of ice particles

Recently, the modeling of dry snowflakes scattering properties using realistic snow particle shapes has received much attention from the scientific community. Considering the importance of the melting layer in precipitation detection and quantification, the simulation of the scattering properties of partially melted snowflakes with a realistic spatial distribution of water should be the natural next step. However the computational cost of such investigation has greatly limited the number of studies focusing on this research field. The details in the microphysics of snow melting are also poorly understood, making difficult to design a model that adequately represents the melting process. There are only qualitative information about the melting process. A description on how to link the melted fraction to the distribution of water within the melting snowflake is still lacking. The melting model presented in this section uses all the available information on the melting microphysics and proposes a procedure to address the important problem of simulating the characteristics of the melting snowflakes.

The effect of spatial distribution of liquid water in mixed-phase particles on their scattering properties has been investigated by Fabry and Szyrmer (1999). They defined six different models describing partially melted hydrometeors composed of aggregates of ice crystals and water. It is shown that the scattering model whose melting snow morphology resembles most the one of real snowflakes (discrete ice crystals covered by a thin layer of liquid water) reproduces the available radar observations at X-band with the highest accuracy.

Korkmaz (2004) exploited the Fabry and Szyrmer (1999) six models to simulate radar signatures at S, X, and Ka bands and compared the results with measured radar data. He found that the best performance is achieved for the model of aggregates with the largest ice density near the core. According to these results, among the various configurations considered, it is the model of ice aggregate crystals covered by a thin layer of liquid water that performs best in representing measured radar parameters of partially melted hydrometeors.

Observational studies (Knight, 1979) suggest that the water part of melting snow aggregates tend to fill the corners between ice crystals when they exists. Moreover, laboratory observations of melting snowflakes, performed by Oraltay and Hallett (2005), suggest that the melting process starts from the high-curvature regions of the surface of the crystals and capillary forces move water from high-curvature to low-curvature regions as melting continues.

Based on these results, the SAM model describes the melting process by starting from the ice phase aggregates derived in section 3.1. The dry and mixed-phase aggregates are described as clusters of polarizable regions belonging to a cubic lattice. In contrast to the aggregation phase of the SAM model the melting simulation is in fact based on the description

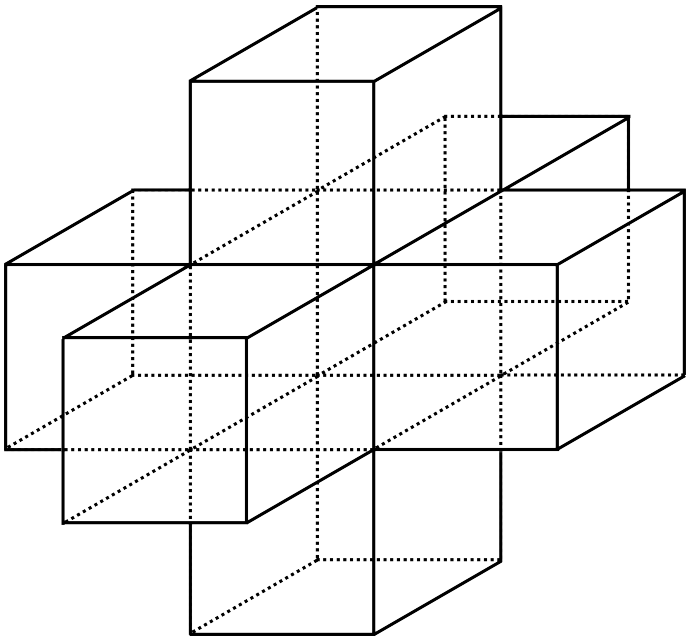

Fig. 3.6 Graphical representation of the regions of the cubic lattice that affects the melting probability of the central region.

of the particle in terms of volume elements and therefore it is not possible to increase the resolution of the lattice grid after the melting process.

A sequence of steps is performed to replace single ice lattice regions (points) with water ones. The aggregate mass and shape is maintained constant during the whole process allowing for a direct comparison of the scattering properties of the partially melted snowflakes with those of its dry counterpart.

Melting probability

For each ice lattice point a probability of melting is defined. The not normalized probability associated to each single ice dipole l in the lattice structure of coordinates (x_l , y_l, z_l) is a function of the physical state (type of material and its phase) of the six regions that share a surface of contact with it. A graphical representation of the regions of the cubic lattice affecting the melting probability of the central polarizable dipole is given in figure 3.6.

This probability of melting is described mathematically in compact way by

$$P^l_{tot}(x_l, y_l, z_l) \propto \sum_{j,k} P_{state}(\mathbf{x}_l + j\,\mathbf{I}_k) \quad i = -1, 1 \quad j = 1, 2, 3 \tag{3.8}$$

where $\mathbf{I}_k$ is the k-th row of the 3×3 identity matrix.

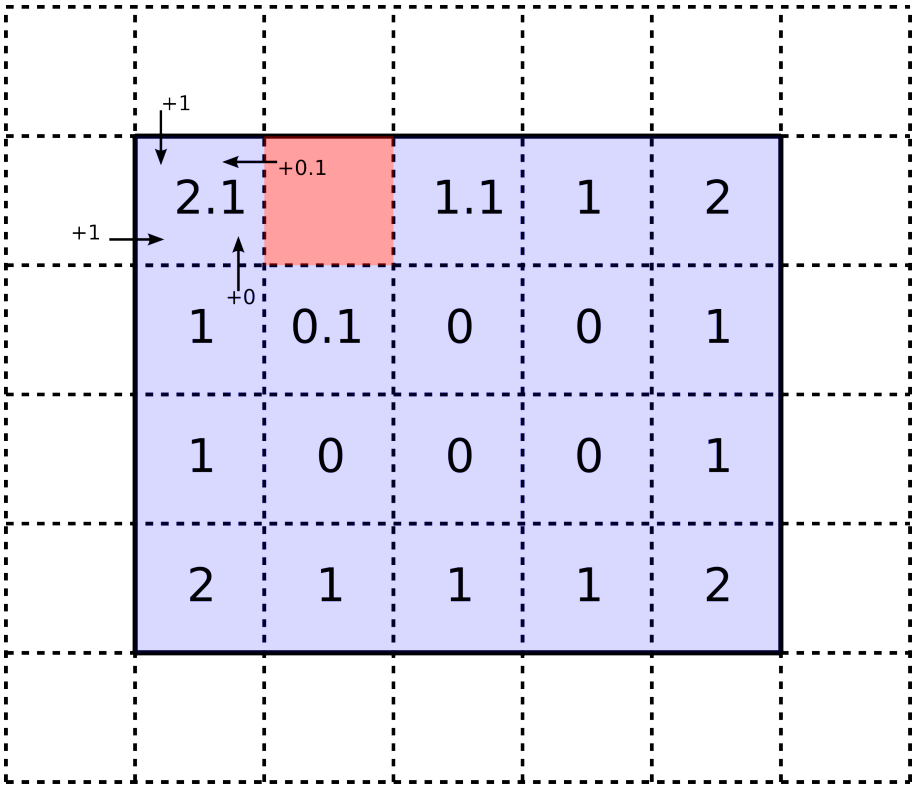

Fig. 3.7 A two-dimensional representation of the technical procedure used to compute the melting probability. The color code for the type of material and phase of the lattice regions are as follows: blue for ice, red for water, and white for air. For each lattice region the melting probability is shown. As an example for the ice cell in the upper left corner the methodology that calculates the melting probability P_{tot} is specified.

Any lattice region might be composed of air, ice, or water (state index in equation 3.8). Only the six regions that have a non-null area of contact with the central region are accounted for in the computation of the melting probability of the central region in accordance with the Fourier's law of heat conduction. The SAM algorithm was run setting $P_{air} = 1$, $P_{water} = 0.1$, and $P_{ice} = 0$. A two-dimensional example of the computational scheme of the probability of melting associated at each dipole region is given in figure 3.7.

The melting process algorithm statistically advantages the melting of the aggregate surface regions with respect to the inner parts of the particle since, at the initial steps, internal points, being surrounded only by other iced regions, have an associated probability to melt that is zero. The melting procedure is performed until the number of water regions reaches the value set by the user. The final configuration shows that the melted points are randomly distributed mostly on the particle surface (an example is given in figure 3.8).

The mixed-phase particle has the same mass and shape of the corresponding dry particle so that a direct comparison among the radar-derived parameters is possible. Since the natural

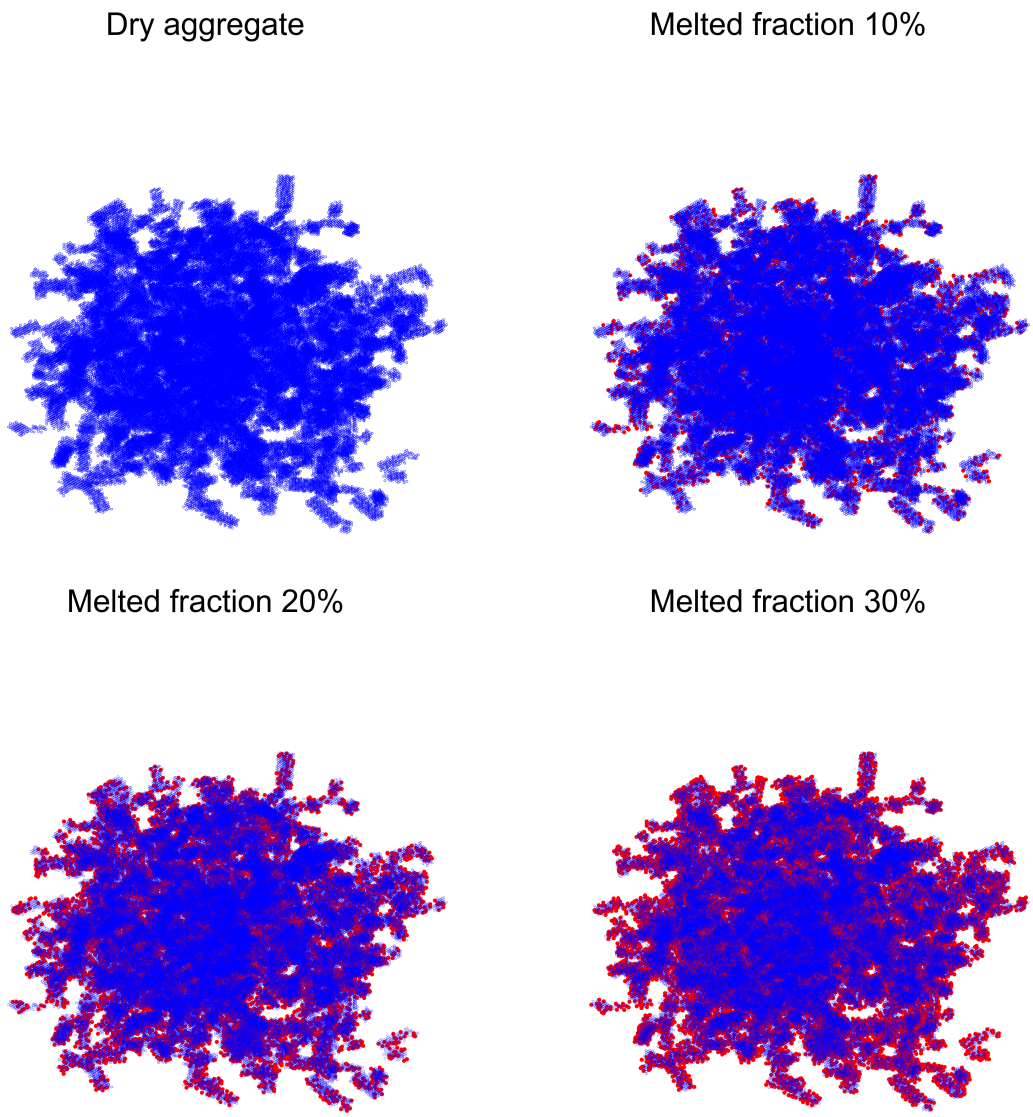

Fig. 3.8 Images of dry and partially melted aggregates snowflake with D_{max} = 3 mm. The same aggregate is shown with melted fraction equal to 0% (completely dry aggregate), 10%, 20% and 30%. The snowflakes are represented as a cluster of points with the lattice regions composed of ice colored with blue and the water ones are drawn in red.

melting process changes the morphology of the snowflake, this method is not appropriate to model mixed-phase particles with large values of melted fraction. However, Figure 3.8 shows that 10% of melted fraction covers just a small part of the total particle surface; thus, the use of the same shape in the computations is an acceptable assumption. For larger values of melted fraction this assumption becomes questionable and the migration of the water mass to the inner parts of the snowflake should be taken into account.

Although the melting behavior is mostly guided by the snow crystal habit, observational studies have suggested the early stages of melting to be more intense on the lower part of the snowflake (Fujiyoshi, 1986; Mitra et al., 1990). This spatial enhanced melting has been described only qualitatively, and there is neither an indication for the early melting stage time extent nor for the melted mass fraction. Perhaps this differential melting between the upper and the lower part of the snowflake could increase the polarimetric signature of melting snowflakes and the study of this particular characteristic of snow melting is left for further studies.

Chapter 4

Scattering computations

The main purpose for snowflake shape modeling is to evaluate the sensitivity of snow particles' single scattering properties to the non-homogeneous distribution of ice mass within the snowflake volume. In this chapter the single-scattering properties of the snowflakes modeled with the SAM algorithm (dry and mixed phased) are computed by using a discrete dipole approximation (DDA) code which allows to model irregularly shaped targets. In case of mixed-phased particles, realistic radiative properties are obtained by assuming snow aggregates with a 10% of melted fraction. The single-scattering properties are compared with those calculated through Mie theory together with Maxwell-Garnett effective medium approximation using both a homogeneous sphere and a layered-sphere models.

The single scattering properties analysis focus on the effects of internal mass radial distribution. It is known that due to the aggregation process not only the only snowflake density decreases with size, but it is also expected that density in the inner portion of snow aggregate is greater then the exterior part of it. This will likely have important effects on the scattering from a dry and melting snowflake: for example, since a greater proportion of the mass is confined in a small volume (considered for simplicity to be at the center of the snowflake), more of the melted mass will be closer to the center, resulting in smaller enhancements in the bright band than if it were distributed uniformly throughout the melting hydrometeor.

Some applications to quantitative precipitation estimation using radar data are presented to show how the resulting differences in the basic optical properties would propagate into radar measurable. Large discrepancies in the derivation of the equivalent water content and snowfall rate from radar measurements could be observed when large-size parameters are accounted for. The results of the present analysis has been published in an international peer reviewed scientific journal (Ori et al., 2014).

4.1 Snowflake models

Different microphysical models are considered to evaluate the effect of shape, mass distribution, and size-mass relation on the single-scattering properties and main radar parameters in case of snow precipitation. The models' configurations are as follows: (1) the SAM model applied to ice aggregates, (2) the soft-sphere model (3) the layered-sphere model, and (4) the layered-sphere model that exactly maps the radial mass distribution of SAM aggregates.

SAM complex aggregates

The SAM algorithm (chapter 3), is used to model the aggregation of snowflakes. Since the present study focuses on the effects of the radial distribution of mass to snowflake scattering properties, the aggregation process is tuned to simulate the snowflake's growth (core aggregation particle CAP) through a continuous collection of pristine ice crystals (next adding particles NAP).

A realistic internal mass distribution is obtained by clustering particles with increasing dimension as the maximum size of the aggregate increases. For this work, hexagonal columns are selected as the basic shape that composes the aggregates in accordance with previous studies (Magono and Lee, 1966) reporting that one of the basic habit of the ice crystal within clouds is the hexagonal column.

The size of the NAP varies during the aggregation process and becomes larger as the aggregates maximum dimension (D_{max}) increases. The NAP dimension is, in fact, extracted randomly from a population of hexagonal columns described by a gamma particle size distribution that evolves in accordance with the maximum size of the aggregate (CAP). The gamma distribution is defined as

$$f_{\theta,k}(x) = \frac{x^{k-1}\, e^{-x/\theta}}{\theta^k\, \Gamma(k)} \tag{4.1}$$

where k is the shape parameter, θ is the scale parameter, and Γ(k) is the *complete gamma function* (the analytic continuation of the factorial in the complex number domain).

The expected value and the variance of $f_{\theta,k}(x)$ are respectively $E[x] = k\theta$ and $V[x] = k\theta^2$. In our model we assume that both these parameters vary linearly with the aggregate maximum dimension so that

$$E[x] = k\theta = A\, D_{max} \quad V[x] = k\theta^2 = B\, D_{max} \tag{4.2}$$

where A and B are constants to be defined according to the microphysical characteristic that are expected to be found in the modeled aggregates.

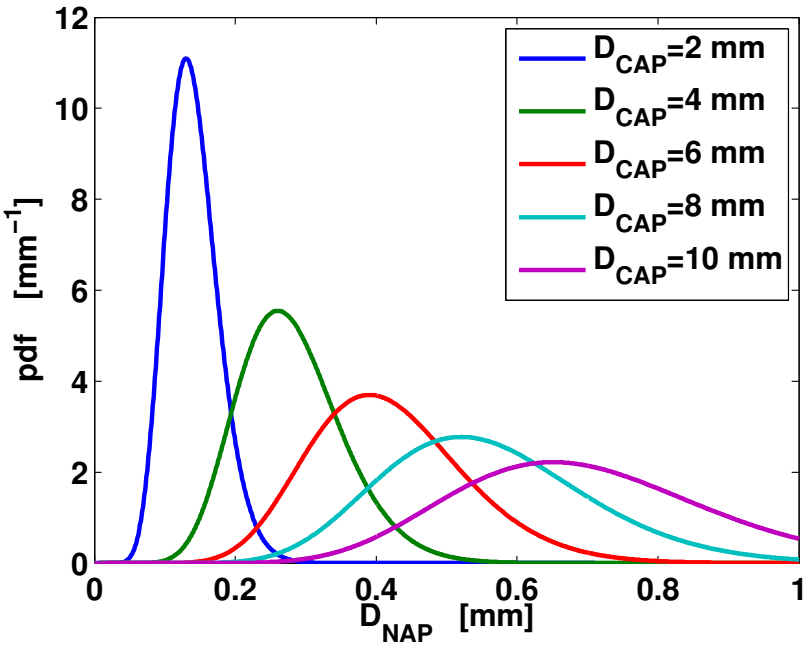

Fig. 4.1 Evolution of the probability density functions of the size of the NAP for increasing maximum dimension of the CAP, for the continuous collection aggregation model.

A graphical representation of the evolution of the size distribution of the NAP is given in figure 4.1. The two constants A and B are determined so that the final aggregate fits the available data concerning snowflakes size-mass relation and in particular that proposed by Brandes et al. (2007) that is here reported:

$$m(D_{max}) = 8.9 \cdot 10^{-5} \, D_{max}^{2.1} \tag{4.3}$$

where the particle dimension D_{max} is in millimeters and its mass m is in grams. It should be noted that Brandes et al. (2007) mass-size relationship is not based on the individual particle D_{max}, but on the *median volume diameter*[1] D_0 of a size distribution based on D_{max}. Equation 4.3 actually catches a description of the bulk characteristics of the snowflake distribution, but as long as the underling PSD is based on the D_{max} it should be safe to consider equation 4.3 as representative of mass to D_{max} measured relation.

[1] Given a certain particle size distribution $N(D)$, the median volume diameter D_0 refers to the midpoint of the PSD, where half of the particle volume is in particles smaller than the mean and the other half is in particles larger than the mean. In mathematical form

$$\int_{\min D}^{D_0} D^3 N(D) \mathrm{d}D = \int_{D_0}^{\max D} D^3 N(D) \mathrm{d}D$$

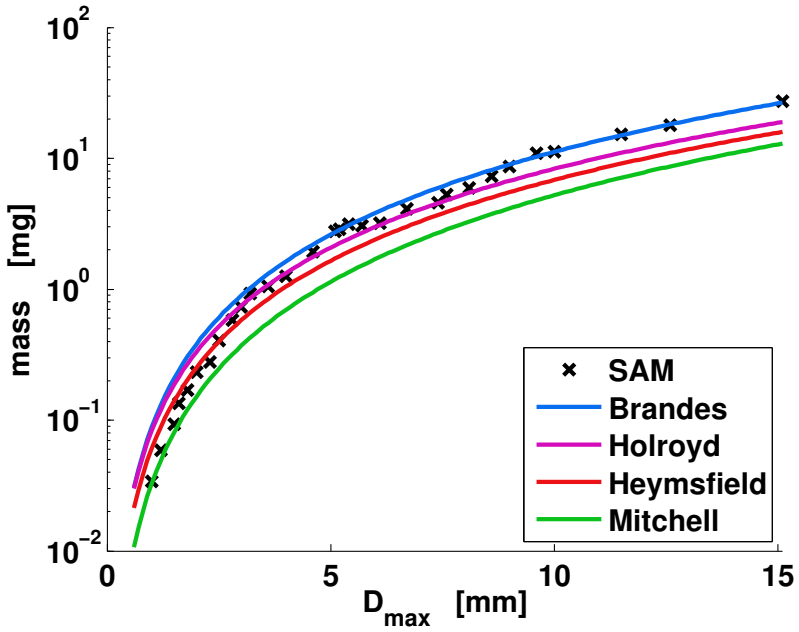

Fig. 4.2 Aggregate mass as a function of the size. The colored curves represent multiple size-mass relations derived from measured data: Brandes et al. (2007) (blue), Holroyd (1971) (magenta), Heymsfield et al. (2004) (red), and Mitchell (1996) (green). Black crosses are the values of the simulated aggregates.

Figure 4.2 shows the evolution of the mass of the simulated aggregates for $A = 0.07$ and $B = 1$ mm as a function of their maximum dimension. The SAM solution is compared with the Brandes mass-size relation and with other relationships found in literature. Note that the SAM solution falls within the spread of the measured relations except for the lowest-particle dimensions. Equation 4.3 has been derived by Brandes as a least squares fit applied to measured data. Because of the larger variability in the bulk density of small snowflakes, the Brandes relation, obtained through a data interpolation process, best represents the microphysical properties of large particles while representation of the densities of very small snowflakes is less accurate. As a consequence, the mass value of the aggregated particle simulated by SAM with maximum dimension smaller than 3 mm is lower than the mass calculated through equation 4.3.

Since the shapes of the largest particles are obtained by aggregating additional crystals to an agglomerate of smaller ones, equation 4.3 not only represents the mass of the aggregate as a function of its size, but also describes the radial mass distribution (or density) within each particle. The smaller particles of the considered collection are in fact the inner parts of the larger ones and thus the radial distribution of the mass within each particle should follow the mass-size relation determined by the individual particles.

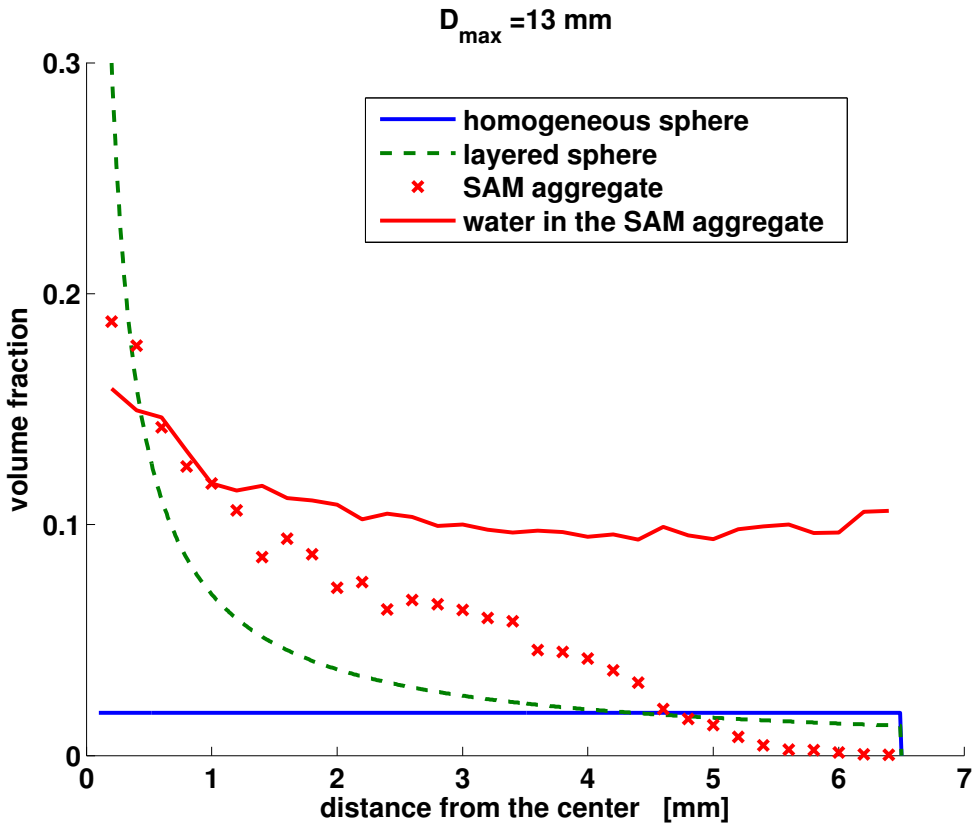

Fig. 4.3 Radial distribution of volume fraction (ratio between mass density and ice mass density) for an aggregate with D_{max} of 13 mm. The volume fraction is plotted for homogeneous sphere (blue), layered sphere (dotted green), and SAM aggregate (red crosses) models. The figure also shows the liquid water fraction (red line) for the corresponding partially melted snowflakes. In order to calculate the effective density of the aggregate models (SAM), the space is divided in spherical shells of equal thickness (0.2 mm) and the number of dipoles belonging to each spherical shell are counted. The water fraction is computed dividing the number of water dipoles in each shell by the total number of dipoles belonging to that shell.

Some important physical and geometrical characteristics such as the radial density distribution and the aspect ratio of the aggregates are briefly analyzed. Figure 4.3 shows the ratio between mass density and the mass density of pure ice (0.917 g/cm^3), as a function of the distance from the center, of a SAM aggregate with maximum dimension equal to 13 mm. The result obtained for the SAM aggregate is compared to a homogeneous radial density distribution (soft-sphere model) and to a density distribution within a layered sphere following exactly equation 4.3. The radial mass distribution of the SAM aggregate follows the radial distribution derived from equation 4.3 with some expected discrepancies due to the random nature of the algorithm describing the aggregation process.

Brandes et al. (2007) defined the aspect ratio a_r of the observed snowflakes as the ratio between the maximum vertical length and the maximum horizontal dimension measured by a two-dimensional video disdrometer. The measured mean aspect ratio is given as a function of the maximum dimension:

$$a_r(D_{max}) = 0.01714\,D_{max} + 0.8467 \tag{4.4}$$

Equation 4.4 indicates that the flakes are nearly spherical on average (with mean values that increase from 0.84 at the smaller dimensions to about 1 at 10 mm). Obviously the fitted a_r curve is just a rough representation of the mean aspect ratio features of the observed particles and looking at the raw date the complex characteristics of the natural snowflakes are evident. All possible value of a_r are encountered and the distribution is particularly wide for small particles.

Since the aggregates modeled by SAM do not account for any preferential falling orientation, a_r values are calculated using a different methodology. For a given aggregated snowflake the major axis has been found. The second axis is the longest dimension in the orthogonal plane to the first axis. Finally, the third axis is the maximum dimension in the perpendicular direction to the plane defined by the other two axes. The aspect ratio value is calculated as the ratio of the minor axis to the major axis. Computed a_r values for SAM aggregates range from 0.8 to 1. The results are consistent with the values found by Brandes et al. (2007). Certainly the few modeled aggregates are not aiming at resembling the properties of all possible natural snowflakes, but considering also the fact that the scattering simulations are performed using orientation averaging of the particles, the a_r features of the snowflake population should be of minor importance in determining the radiative properties of snow.

The melting model of the SAM algorithm has been used to convert the aggregate snowflakes into partially melted particles. For the present work a 10% of the total aggregate mass is water and the remaining is ice. The conservative value of 10% of melted fraction allows a direct comparison of scattering properties between dry and partially melted particles keeping constant the particle mass and morphology. Figure 3.8 shows that 10% of melted fraction covers just a small part of the total particle surface; thus, the use of the same shape in the computations is an acceptable assumption. Modeling larger values of melted fraction would need to take into account the migration of water drops from the high-curvature regions (where the melting process is most likely to take place) to the low-curvature regions of snowflake and eventually the collapse of the ice structure.

Another important issue encountered in the simulation of scattering properties at larger melted fractions the computational cost of DDA. This algorithm is really resource intensive

and the time required to complete the computations increases with respect to the real part of the index of refraction of the material. Because the water index of refraction is much larger than the index of refraction of ice the simulation of the scattering properties of more melted snowflakes with DDA would require either a much powerful computing infrastructure or a more efficient simulation technique. A possible solution targeting this problem has been developed and it is presented in section 4.4.

The melting fraction distribution inside a partially melted aggregate with maximum dimension of 13 mm is shown in figure 4.3 by the red solid line. Details on the computation of the melted fraction are given in the figure caption. As expected values around 10% are encountered all along the aggregate's dimension. Slightly larger values are found near the core where the total particle density is very large due to the aggregation of small ice crystals; this is in accordance with (Fabry and Szyrmer, 1999).

Homogeneous and layered sphere models

The simplest microphysical description for snowflake modeling relies on the assumption that snow particles are approximated by homogeneous spheres and the scattering properties are computed using the Mie analytical solution. These models are commonly known as the soft-sphere models (Liu, 2004). In this work the dielectric properties of the ice sphere are calculated using the Maxwell-Garnett mixing formula. The length of the sphere diameter is chosen to be equal to the maximum dimension of the corresponding aggregated particle. The soft-sphere model is also used to represent wet snowflakes. In this case a fraction of the ice mass is replaced with liquid water and the Maxwell-Garnett approximation is applied to the new mixture of three materials (water, ice,and air).

A more complex model accounts for a core sphere surrounded by multiple shells. This type of geometrical model was developed to improve the modeling of radiative properties of nonhomogeneous particles accounting for a radially stratified structure (Yang, 2003). We use the code developed by Pena and Pal (2009) with spherical layers with equal thickness (figure 4.4). Each layer is characterized by a specific index of refraction computed using the Maxwell-Garnett mixing formula. The layered-sphere model is run in two different configurations:

- Mie-500. In this configuration it is assumed that the mass-size relation follows exactly equation 4.3 (Brandes et al., 2007). A number of 500 spherical shells are assumed. It is important to note that the choice of 500 layers allows to simulate a highly stratified sphere. Different numbers of layers have been tested, and no significant differences in the resulting radiative properties have been found for numbers larger than 50. Partially

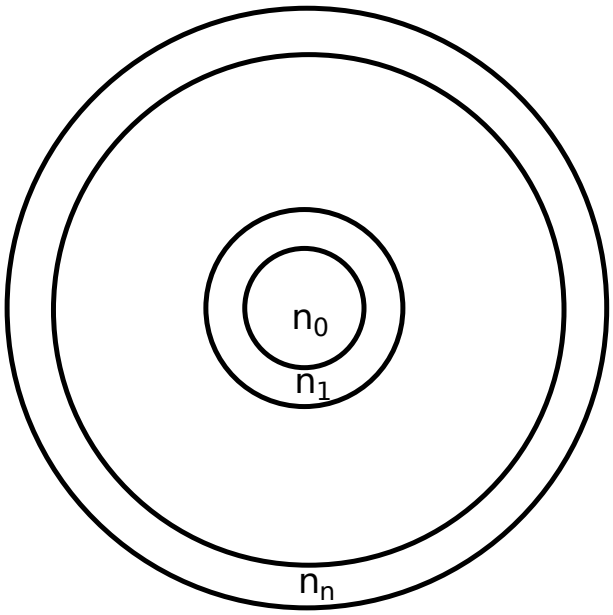

Fig. 4.4 Scheme of a layered-sphere model. Simulations has been performed with the number of layers is n = 500 for the Mie-500 configuration and n = 50 for the Mie-SAM configuration. All the layers have the same thickness

melted snowflakes are modeled by converting an equal fraction of ice mass into water for each layer. The Maxwell-Garnett formula is used to compute the effective dielectric constant of the mixture of ice, water, and air.

- Mie-SAM model. In this configuration a 50-layer sphere model with the exact radial mass distribution of the aggregates modeled by SAM is assumed. This allows a better comparison with the results obtained using the SAM algorithm that does not perfectly follows equation 4.3. In case of mixed-phase particles the same distribution of melted fraction of mixed-phase aggregates is used.

4.2 Simulated scattering properties

4.2.1 Scattering codes and methodology

Simulated single-scattering properties of snowflakes are presented for seven typical radar frequencies (first column of table 4.1). The refractive indexes used in the computations (table 4.1) are derived from the model of Meissner and Wentz (2004) for pure water at 0 °C and from the Matzler (2006) model for ice at -40 °C and 0 °C.

Table 4.1 Microwave frequencies and dielectric properties used for scattering calculations

MW band	Temp [°C]	n Water	n Ice	ε Water	ε Ice
C 5.6 GHz	0	8.34+i2.22	1.79+i7.76e-4	64.6+i37.1	3.19+i6.28e-4
	-40		1.77+i1.16e-5		3.15+i2.54e-4
X 9.6 GHz	0	7.20+i2.85	1.79+i2.65e-4	43.8+i41.0	3.19+i9.46e-4
	-40		1.77+i1.22e-4		3.15+i4.34e-4
Ku 13.6 GHz	0	6.28+i3.01	1.79+i3.62e-4	30.4+i37.8	3.19+i1.29e-3
	-40		1.77+i1.73e-4		3.15+i6.14e-4
Ka 35.6 GHz	0	4.04+i2.42	1.79+i9.18e-4	10.5+i19.6	3.19+i3.28e-3
	-40		1.77+i4.52e-4		3.15+i1.61e-3
W 89 GHz	0	2.93+i1.48	1.79+i2.41e-4	6.40+i8.68	3.19+i8.17e-3
	-40		1.77+i1.19e-3		3.15+i4.02e-3
W 94 GHz	0	2.89+i1.43	1.79+i2.41e-4	6.30+i8.28	3.19+i8.63e-3
	-40		1.77+i1.19e-3		3.15+i4.25e-3
157 GHz	0	2.59+i1.05	1.79+i4.04e-3	5.60+i5.47	3.19+i1.44e-2
	-40		1.77+i2.00e-3		3.15+i7.13e-3

Scattering computation of the homogeneous sphere and of the layered soft-sphere models are performed using the *scattnlay* code by Pena and Pal (2009). Scattnlay is a publicly available implementation of the algorithm for the calculation of the Mie scattering coefficients of a multilayered sphere developed byYang (2003).

The dielectric properties of mixtures of materials are computed using the Maxwell-Garnett mixing formula. In the case of dry snowflakes ice is considered inclusion in air matrix, while for mixed-phase particles water is considered inclusion in ice matrix and as a second interaction the ice-liquid water mixture is considered as inclusion in air matrix. The dielectric mixing formula of Bruggeman and that of Sihvola (Petty and Huang, 2010) have also been tested. The discrepancies between the resulting radiative properties obtained when assuming the different dielectric mixing formula are of negligible importance with respect to the differences obtained using the diverse microphysical descriptions. Thus, for simplicity, only the Maxwell-Garnett mixing formula is assumed in the present study.

Scattering computations concerning the dry and mixed-phase aggregate obtained with the SAM model are performed using the ADDA (Amsterdam DDA) code by Yurkin and Hoekstra (2010) which is a publicly available and memory efficient implementation of the DDA technique (Penttilä et al., 2007). The results obtained with this combination of methodologies are referred as ADDA-SAM in the subsequent figures.

The accuracy of DDA is determined by the number of dipoles used to describe the shape of the scattering particle. To approximate homogeneous medium, the spacing d within

the dipoles must be small relative to the wavelength; Draine and Flatau (1994) propose, as a rule of thumb for the correctness of the methodology, that $|n|kd \ll 1$ where k is the wave vector in the vacuum and n is the complex index of refraction of the medium. The correct representation of the target shape requires also that the dipole spacing must be smaller than any structural length of the target. In order to properly represent the hexagonal columns, which are the constituent particles of the simulated snow aggregates, a dipole spacing of 20 μm is used. For this configuration, the maximum frequencies of the incoming electromagnetic wave allowed by the model are 660 GHz.

The computed radiative properties, for all the simulations, are the total scattering cross section C_s , the total absorption cross section C_a and the radar backscattering cross section σ_{bk} . The radiative quantities are averaged over 1800 uniformly distributed orientations of the scattering particle.

4.2.2 Radiative properties of individual particles

Figures 4.5 and 4.6 show respectively the total absorption and scattering cross section of the simulated aggregates, at four different frequencies, as a function of the size parameter ($x = \pi D_{max}/\lambda$) and compare these quantities with those derived for equivalent homogeneous and layered spheres. The total scattering and absorption cross sections computed with Mie theory assuming one-layer homogeneous spheres or a 500 layered spheres, for particles with D max < 3 mm (x = 1.1 at 35.6 GHz and x = 4.9 at 157 GHz), show larger values than those computed for the complex aggregates with DDA model.

The reason is related with the assumption made on the density distribution within the particle. As illustrated in section 3.1, the SAM model simulates complex-shaped particles with small dimensions that have smaller mass density than those predicted by equation 4.3 On the contrary, for particles modeled as soft spheres (one homogeneous layer) or 500 layered spheres (Mie-500 layers in the plots) it is assumed that the internal mass distribution follows exactly equation 4.3. That explains why the total scattering and absorption cross sections of the spherical models for small particles are larger than those computed with the complex aggregate models. This fact is confirmed by the comparison of the results of the ADDA-SAM model with those of the Mie-SAM model for which the density distribution is the same. The two models show closer computed scattering and absorption cross sections. The differences among results for the homogeneous spheres, the 500 layered spheres, and the 50 layered sphere Mie-SAM allow to evaluate the effect of the density distribution on main radiative properties.

For maximum dimensions larger than 5 mm (x = 1.9 at 35.6 GHz and x = 8.2 at 157 GHz) the total scattering cross section C_s computed for the aggregates with DDA model becomes

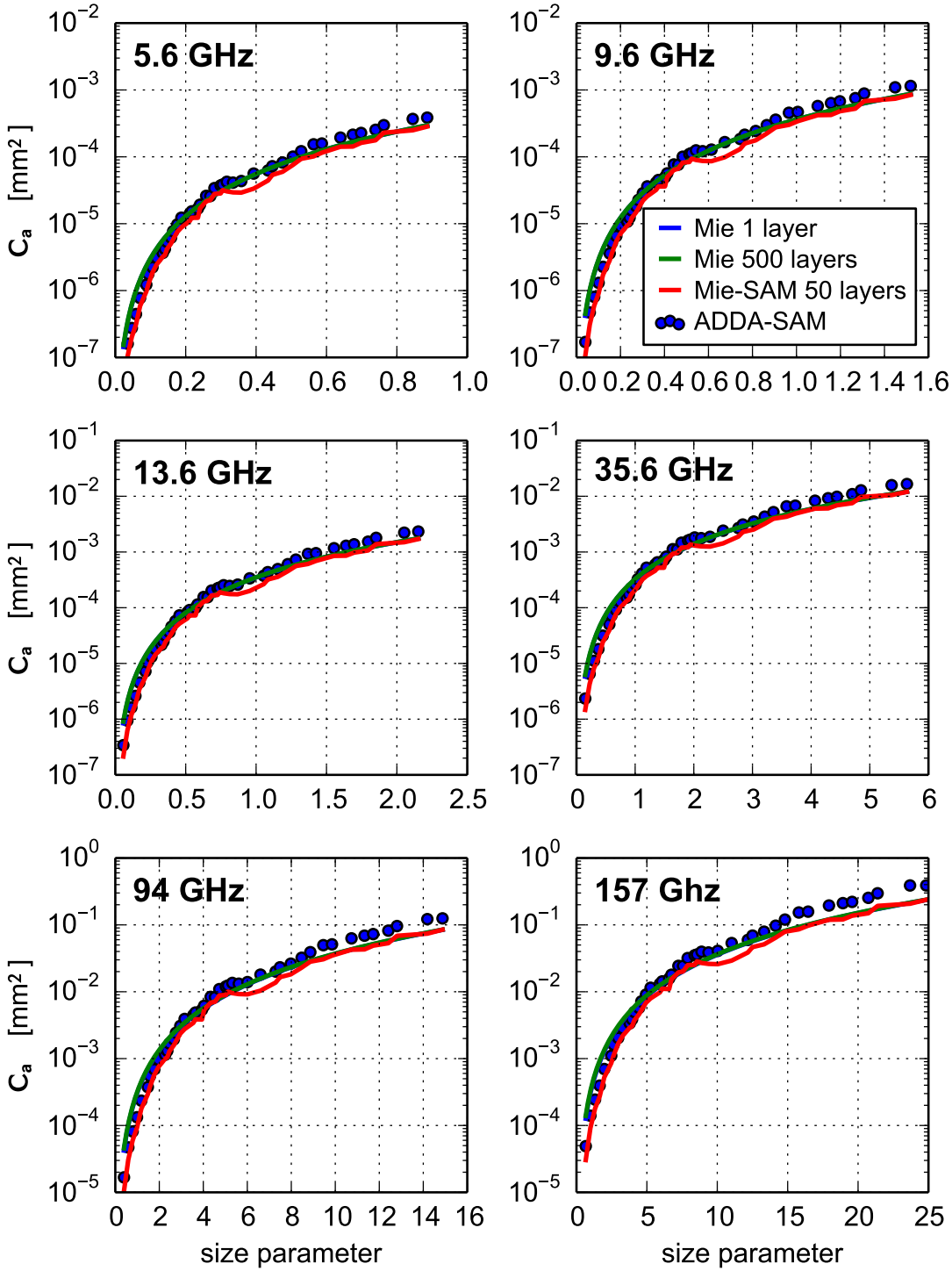

Fig. 4.5 Total absorption cross section as a function of the size parameter of the particle for frequencies of 5.6, 35.6, 94 and 157 GHz. Results from Mie-1 homogeneous soft sphere (blue), Mie-500 layered sphere (green), 50-layered Mie-SAM (red), and complex ADDA-SAM (blue circles) are compared.

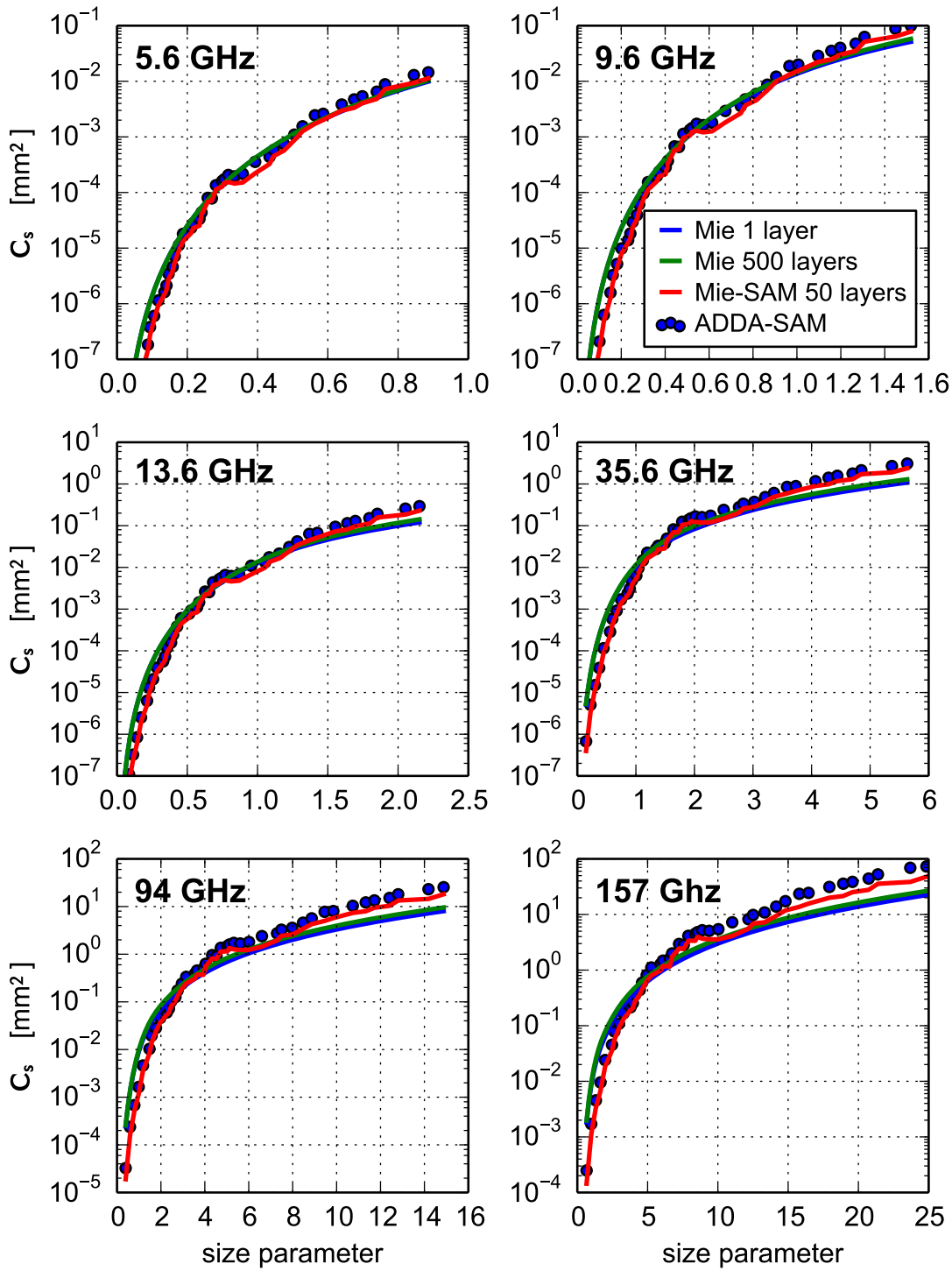

Fig. 4.6 Total scattering cross section as a function of the size parameter of the particle for frequencies of 5.6, 35.6, 94 and 157 GHz. Results from Mie-1 homogeneous soft sphere (blue), Mie-500 layered sphere (green), 50-layered Mie-SAM (red), and complex ADDA-SAM (blue circles) are compared.

larger than that computed for spheres with Mie theory (figure 4.6); the differences are significantly larger in case of homogeneous sphere or 500 layered sphere. A similar behavior occurs for the total absorption cross section C_a but with lesser discrepancies (figure 4.5). The differences are mainly related to the diverse microphysical structures of the particles produced by the considered models.

In the SAM model the ice mass occupies only the volume defined by the pristine ice crystals that compose the aggregate, and the particle can be thought as a sum of discrete scatterers having dielectric constant of solid ice in a volume filled with air. In the soft-sphere and layered-sphere case the ice mass of the modeled snowflake is distributed in a spherical volume and in multiple spherical shells, respectively. The ice mass is diluted all over the volume, and the particle total density is lower than that of pure ice.

The total dielectric properties of the spherical snowflake are obtained by a composition of the dielectric properties of ice with those of air that is supposed to be trapped in the spherical structure of the particle. As a consequence, the value of the index of refraction of the spherical target is closer to the value of the index of refraction of the air, and thus, the interaction with the incoming electromagnetic waves is less intense. This fact is more and more significant as the dimension increases.

The absorption and scattering cross sections calculated using the ADDA-SAM model are at about 30% larger than those obtained with the Mie-SAM model and are significant for all the investigated size parameters. Since these two models have the same radial mass distribution, the greater values of scattering and absorption cross sections for the ADDA-SAM models are imputable to the different microphysical structure.

Shape-dependent effects in the backscattering cross section σ_{bk} are encountered for size parameters larger than 2. Figure 4.7 shows the radar backscattering cross section σ_{bk} as a function of the snowflake size parameter at six different wavelengths. The backscattering cross section computed using the Mie theory presents the typical Mie resonance behavior that, otherwise, is strongly attenuated for results obtained using the ADDA-SAM model in case of aggregates. The backscattering cross section of complex aggregates shows only the first-order Mie resonance minimum, and this minimum is encountered for a larger size parameter with respect to that expected for the homogeneous soft sphere.

Comparing the results obtained from the soft-sphere and the layered sphere models, the effect of the internal mass distribution of the particle on σ_{bk} can be evaluated. The modification of the Mie resonance structure of the layered-sphere model reflects the fact that in a layered sphere each layer is characterized by a proper refractive index and thus by a characteristic length for the backscattering resonance; the result is a composite contribution from each layer leading to a modification of the positions in the Mie's resonance minima

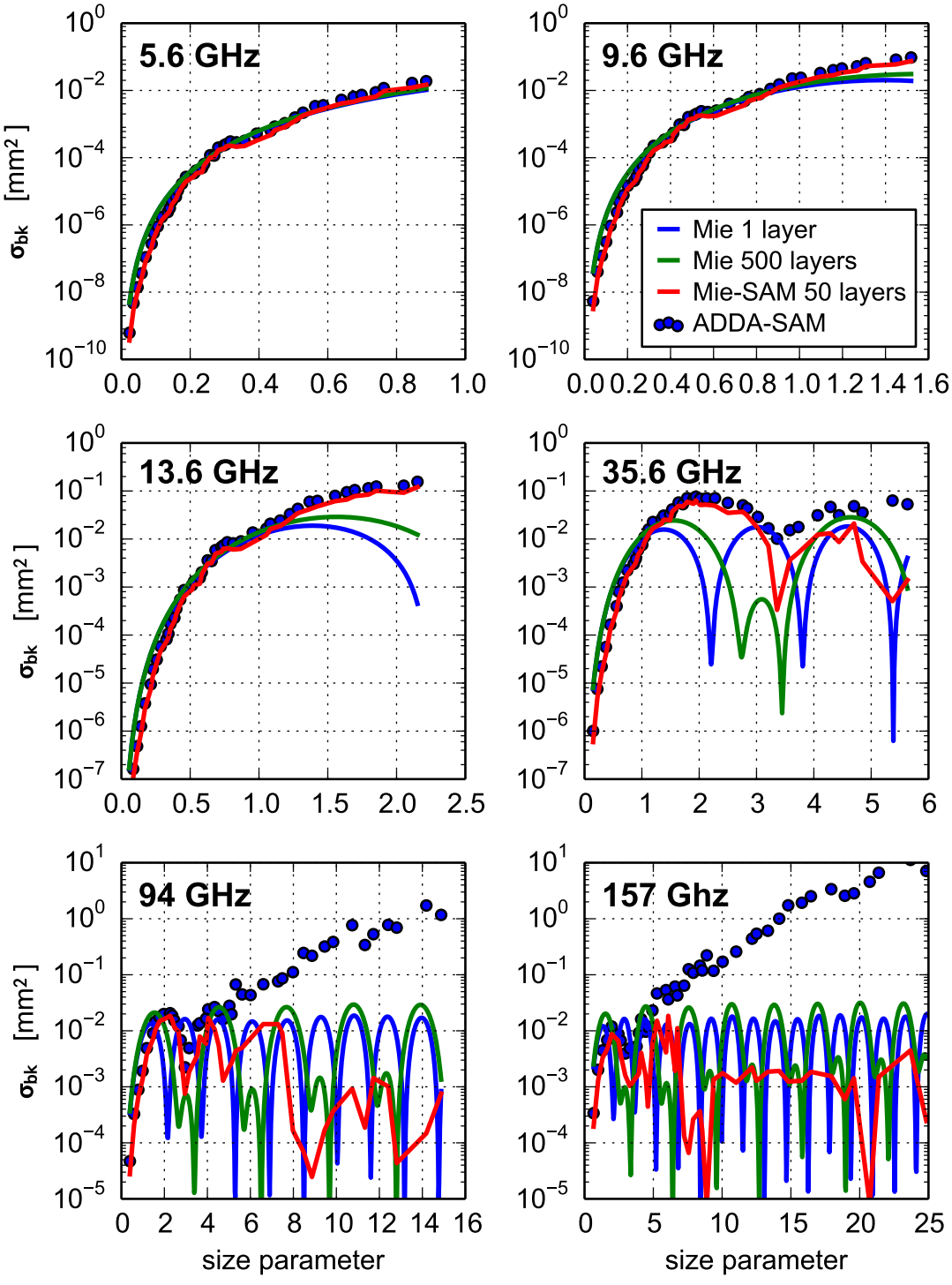

Fig. 4.7 Radar backscattering cross section as a function of the size parameter of the particle for six different frequencies from 5.6 to 157 GHz. Results from Mie-1 homogeneous soft sphere (blue), Mie-500 layered sphere (green), 50-layered Mie-SAM (red), and complex ADDA-SAM (blue circles) are compared.

typical of homogeneous spheres. The introduction of a stratified morphology with the layered-sphere model causes therefore the modification of the Mie's resonance structure. The ADDA-SAM model does not present a well-recognizable resonance behavior due to a lack of symmetry in the geometrical structure of the particle. Nevertheless, a singular minimum is still present when the size parameter is equal to 3.

The backscattering cross sections computed with the ADDA-SAM model is in good agreement with those obtained with the Mie-SAM model for size parameter smaller than about 3. This fact suggests that the radial mass distribution has a leading role on the determination of the backscattering cross section for this range of size parameters.

For particles with size parameter greater than 3, σ_{bk} computed with the ADDA-SAM model show increasing deviations (up to 3 orders of magnitude) from the results obtained with every assumed spherical approximation. The corresponding differences in the total scattering cross section are much smaller. The main parameter influencing the differences is the value of the phase function at 180°. Figure 4.8 (left) shows the value of the phase function at 180°, as a function of size parameter, computed for dry snowflakes at 94 GHz using the different models. In Figure 4.8 (right) the phase functions of particles with D_{max} = 13 mm at 94 GHz (corresponding to x = 12.8) are presented. Very large differences are encountered at the backscatter angle of 180° where the phase function computed for different models spans over about 5 orders of magnitudes. The larger values are found in case of ADDA-SAM model and are consistent with results shown in figure 4.7.

Scattering properties of partially melted snow particles

The ratio between the radiative properties at 5.6 and 35.6 GHz for mixed-phase particles and dry snowflakes are shown in figure 4.9.

As expected the most prominent difference between the dry and the partially-melted snowflakes radiative properties is found in the absorption power. As it has already illustrated the completely frozen hydrometeors are one of the most transparent media microwave frequencies and ice exhibit a very low dielectric attenuation. On the contrary water interacts strongly with microwave radiation leading to an appreciable absorption of electromagnetic energy. The top row of figure 4.9 shows that the total absorption cross section of 10% melted snowflakes could be as large as 300 times the absorption cross section of their dry counterparts when C-band (5.6 GHz) and spherical models are considered. Higher frequencies leads to lower absorption gain because the imaginary part of the water index of refraction decreases with the frequency in the microwave regime (table 4.1).

Even if the melted fraction of the wet snowflake is only 10%, the scattering simulations show an increase in the total scattering cross section that is of the order of 20% to 60%

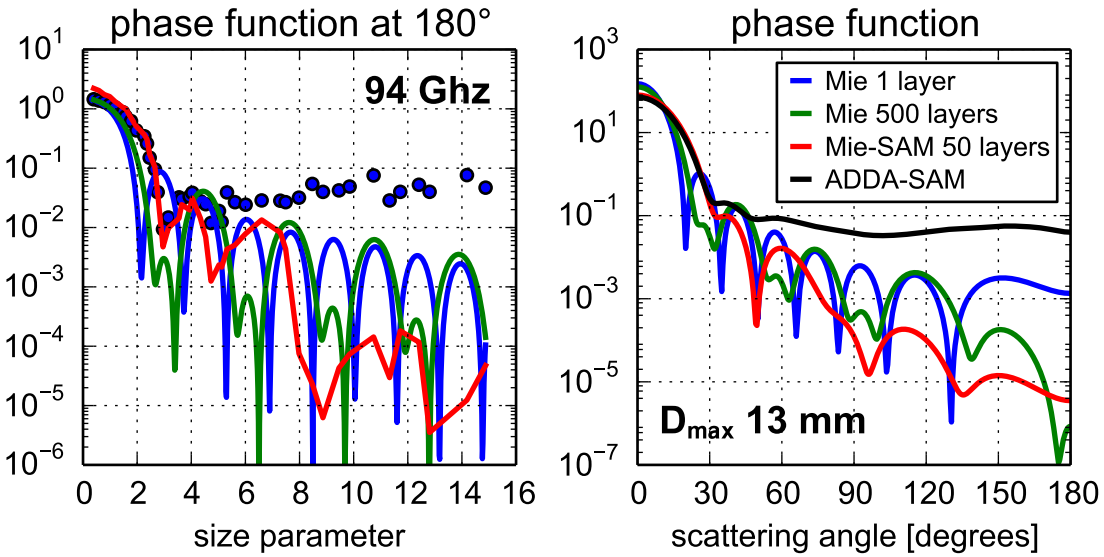

Fig. 4.8 (left panel) Value of the phase function at 180° (backscattering) as a function of the particle maximum dimension at 94 GHz. (right panel) Phase function at 94 GHz of snowflakes with D_{max} = 13 mm.

with respect to the dry particle (central row of figure 4.9) depending on the frequency investigated and the snowflake model used. The cross-section difference is larger for the lowest frequencies because the real part of the water refraction index at microwave increases as the frequency of the incoming electromagnetic wave decreases (table 4.1). Looking at the results for the ADDA-SAM model, it is interesting to see that the largest gains in the scattering cross section are achieved for the most small particles. This is probably because for really small particles the most of the water fraction is exposed to the incoming radiation on the exterior part of the aggregate, whereas for larger snowflakes an increasing portion of water is "hidden" in the interior part.

The partial melting of the snowflakes increases their effective refractive index. As a consequence, the positions of the resonance minima of the backscattering cross section, computed using the spherical models, shift to lower size parameters. This shift is responsible for the strong oscillating behavior of the difference between the radar backscattering cross section of the wet and the dry particles for all the spherical models (bottom row of figure 4.9) at 35.6 GHz and higher frequencies. When complex aggregate models are used, the resonance effect is mostly suppressed and therefore it is easier to see that the backscattering cross section increases of 40% because of the 10% partial melt of the particle.

The difference between the scattering properties of mixed-phase particles and dry snowflakes is larger for the spherical models than for the ADDA-SAM model as a con-

sequence of change in the effective refractive index of the overall spherical volume that is otherwise a localized effect in case of aggregate.

4.3 Quantitative precipitation estimation

The equivalent copolar radar reflectivity at horizontal polarization[2] Z_{hh} is calculated, at each frequency, by integrating the horizontal copolar radar backscattering cross section σ_{hh} as a function of the maximum particle size over the whole particle size distribution (PSD).

$$Z_{hh} = \frac{\lambda^4}{\pi^5 |K_w|^2} \int_{\min(D_{max})}^{\max(D_{max})} \sigma_{hh}(D_{max})\, N(D_{max})\, dD_{max} \tag{4.5}$$

In equation 4.5, σ_{hh} is the copolar backscattering cross section at horizontal polarization, and the characteristic size of the particles is assumed to be their maximum dimension D_{max}.

Following Straka et al. (2000) it is assumed an inverse exponential PSD

$$N(D) = N_0\, e^{-\Lambda D_{max}} \tag{4.6}$$

where the distribution parameters N_0 [$\mathrm{mm}^{-1}\ \mathrm{m}^{-3}$] and Λ [mm^{-1}] are derived from Marzano et al. (2010, 2007) and reported in table 4.2 for dry and wet aggregate distributions.

The ice water content IWC [$\mathrm{g/m}^3$] can be expressed as

$$IWC = \int_{\min(D_{max})}^{\max(D_{max})} m(D_{max})\, N(D_{max})\, dD_{max} \tag{4.7}$$

where $m(D_{max})$ is the mass of the particles as a function of their maximum dimension (equation 4.3) and $N(D_{max})dD_{max}$ is the particle concentration within the size bin of width dD_{max} around D_{max}.

Z_{hh} and IWC are calculated for 1632 different PSDs. The PSD parameters used for these computations have been selected by uniformly sampling values between the parameters' limit expressed in table 4.2. The numerical integration has been performed using the Simpson quadrature rule. The PSDs have been truncated at $\min(D_{max}) = 1$ mm and $\max(D_{max}) = 15$ mm as in Marzano et al. (2010). The results of these calculations are shown in figure 4.10.

[2]The equivalent copolar radar reflectivity is the equivalent reflectivity factor (see equation 2.31) where measured radar signal is specified to be at the horizontal polarization state at both transmitting and receiving phase.

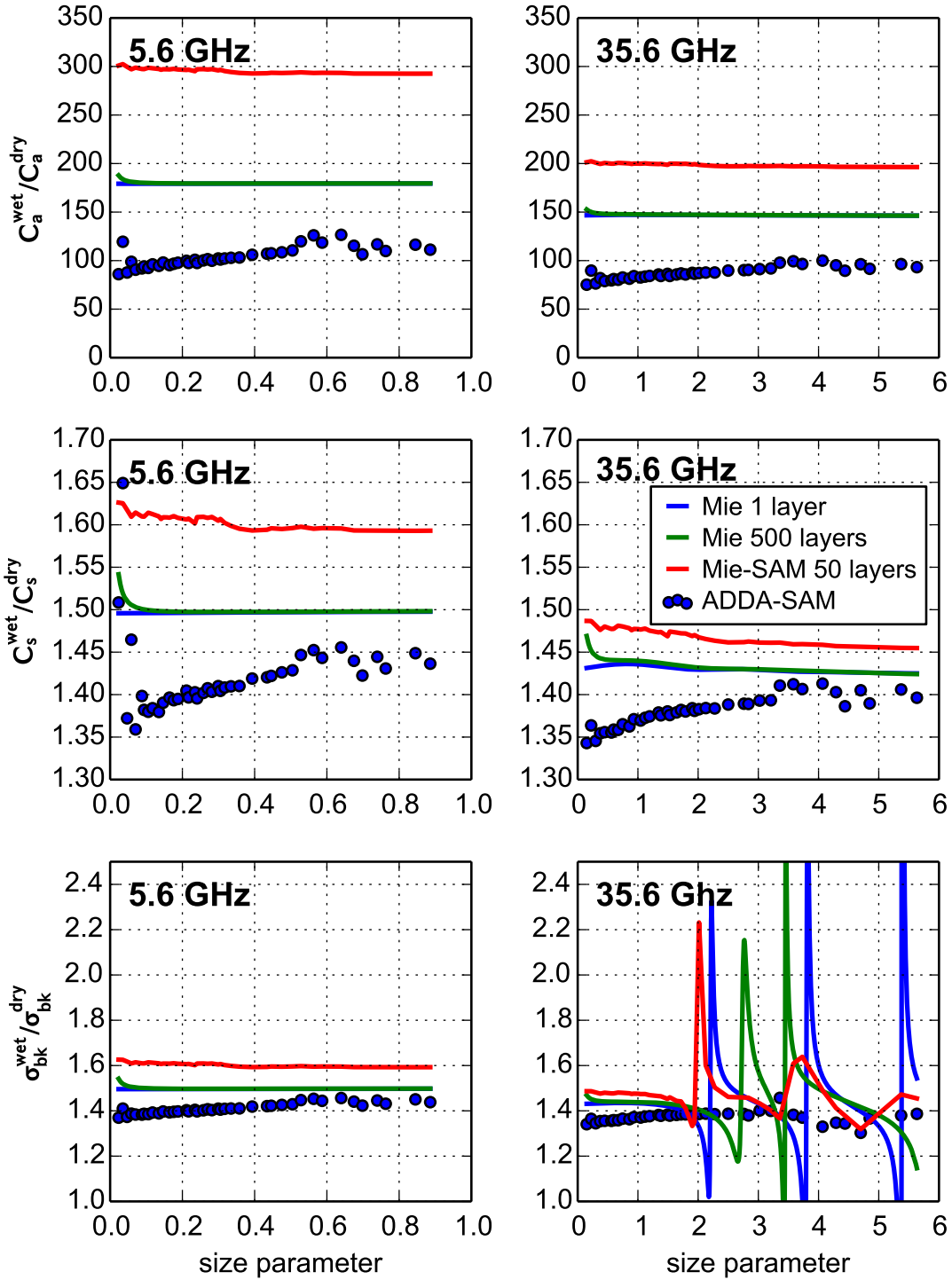

Fig. 4.9 Differences in the (top row) total absorption, (middle row) total scattering (bottom row) backscattering cross sections between wet and dry snowflakes as a function of the maximum dimension of the particles. Results are for (left column) C-band 5.6 GHz and (right column) Ka-band 35.6 GHz

Table 4.2 Particle Size Distribution parameters adopted for the computation of dry and wet snow equivalent radar reflectivity

DRY	WET
$2.2 \leq \Lambda \leq 8.8 mm^{-1}$	$1.8 \leq \Lambda \leq 3.1 mm^{-1}$
$2380 \leq N_0 \leq 42000 mm^{-1} m^{-3}$	$1515 \leq N_0 \leq 4800 mm^{-1} m^{-3}$
$1.0 \leq D \leq 15.0 mm$	

Z_{hh} of dry snowfall obtained from the radiative properties of the ADDA-SAM model and the Mie-SAM model (figure 4.10) are very similar as a consequence of the relatively small differences in the computed σ_{hh}.

The copolar reflectivity of dry snowfall obtained from the scattering data of the ADDA-SAM model are lower than those obtained with the Mie-1 and Mie-500 layer models. The differences between the data sets are of the order of 5 dBZ for all the frequencies investigated and for values of IWC of the order of 10^{-4} g/m^3 and reduces as the ice content increases. These differences at small values of IWC are mainly due to the features of the PSDs used for the comparisons.

The inverse exponential PSD implies a large number of small particles. Since, for small particles, the sphere-Mie data sets show larger backscattering cross sections with respect to the ADDA-SAM model, larger reflectivity values are computed for distribution of spherical scatterers. As the PSD mean shifts to larger values the difference between the two data sets reduces due to the larger amount of large snowflakes included in the PSD. Note that aircraft measurements of the snow size distribution are generally affected by particles shattering at the optical probes (Heymsfield et al., 2008) and the relative importance of small particles to the total reflectivity could be generally overestimated. For an unbiased calculation of the snow reflectivity it is thus necessary to properly represent both the particle's radiative properties and the PSD characteristics.

The difference between the ADDA-SAM and the Mie radar reflectivities in the case of wet snowflakes are of the order of 2 dBZ for all the frequencies. The reduced difference between the two data sets with respect to the dry case is explained by considering the fact that the difference of the backscattering cross section between wet and dry snowflakes for small particles (figure 4.9) is larger in the spherical models than in the ADDA-SAM model.

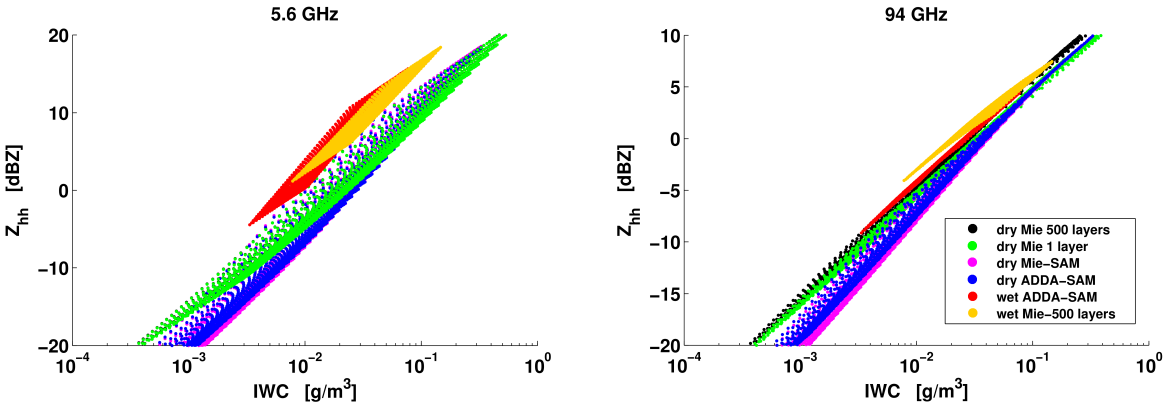

Fig. 4.10 Copolar radar equivalent reflectivity at horizontal polarization for (left) C and (right) W frequencies as a function of IWC. Each dot is a computation of Z hh for one of the 1632 PSD. Blue and red dots are obtained using ADDA-SAM for dry and mixed-phase particles (with 10% of melted mass), respectively; black and yellow dots are obtained for dry and wet Mie-500 layered sphere (with 10% of melted mass); green dots are obtained with the homogeneous Mie-1 models (in the left the black dots are completely overlapped by the green ones); magenta dots are obtained with the 50-layered Mie-SAM model (in both panels magenta dots are almost completely overlapped by the blue ones).

Snowfall rate

Liquid equivalent snowfall rate (SR) can be expressed as

$$SR = \rho_w^{-1} \int_{\min(D_{max})}^{\max(D_{max})} m(D_{max})\, v_t(D_{max} N(D_{max})\, dD_{max} \tag{4.8}$$

where $m(D_{max})$ is the mass size relation of the snowflakes (equation 4.3 in this study), ρ_w is the mass density of water, and $v_t(D_{max})$ is the terminal fall velocity-size relation. Equation 4.8 is expressed in general units of measure as in Matrosov (2007); given units of measure for the operands used in the text (grams for masses, m/s for terminal fall velocities, mm^{-1} m^{-3} for PSD, and millimeters for D_{max}) a factor of 3.6 10^6 should be applied to convert the resulting m/s to the most commonly used mm/h.

The relationship between falling speed and size of snowflakes is a complicate relation of the type and shape (and other properties) of the snowflakes. Numerous studies have modeled the terminal fall velocity of aggregate snowflakes with a power law relationship as a function of the maximum dimension of the falling particle. The equations describing the falling speed as a function of the size of the snowflakes are just simplified formulas, and the accuracy of these relationships is not guaranteed.

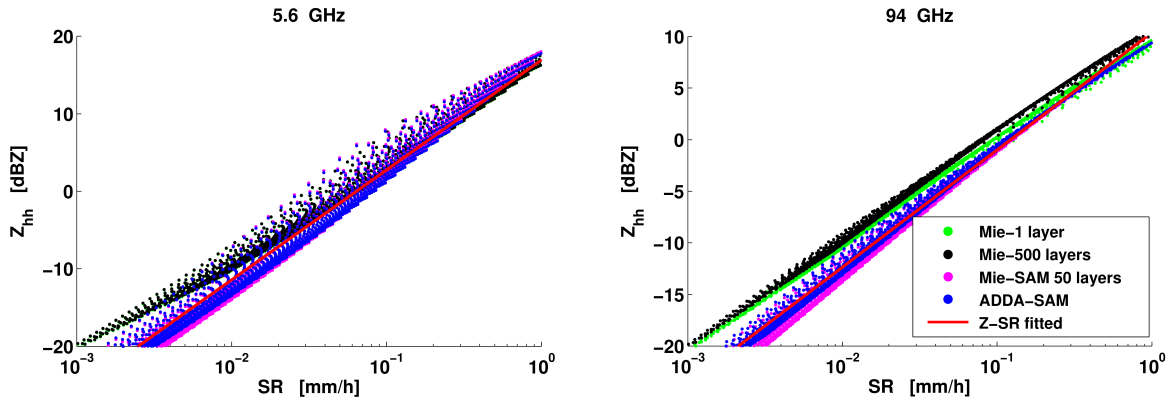

Fig. 4.11 Copolar radar equivalent reflectivity at horizontal polarization for (left) C and (right) W frequency bands as a function of the snow rate. Each blue dot represent a different PSD of dry snow in the ADDA-SAM model. The overlapped red line is a power law fit of the results of the ADDA-SAM model. Black and green dots represents the results obtained using the Mie-1 homogeneous sphere and the Mie-500 layered-sphere models, respectively (in the left the green dots are completely overlapped by the black ones); magenta dots are obtained with the 50-layered Mie-SAM model (in both panels magenta dots are almost completely overlapped by the blue ones).

Brandes et al. (2007) published two speed-size relationships that come from fitting data sets from two different snow events:

$$\begin{aligned} v_t(D_{max}) &= 2.076\, D_{max}^{0.141} \\ v_t(D_{max}) &= 2.958\, D_{max}^{0.157} \end{aligned} \tag{4.9}$$

Another speed-size relation from Straka et al. (2000) is also introduced to evaluate the sensitivity of SR to the fall speed-size relation

$$v_t(D_{max}) = 4.836\, D_{max}^{0.25} \tag{4.10}$$

For the three fall speed-size relations shown the D_{max} is expressed in meters. For particle dimension less than 5 mm (that represent the majority of the considered PSDs) equation 4.10 falls in between the two Brandes' relationships (equations 4.9).

The $Z_{hh} - SR$ relationships are particularly important because they give the opportunity to directly measure the amount of precipitation from radar measurements. Figure 4.11 shows the computed copolar reflectivity as a function of the sampled PSD for two radar frequencies. A power law's fit (red line) of the $Z_{hh} - SR$ results is also shown in case of dry aggregates.

In C-band (5.6 GHz) the differences between the Z_{hh} computed with the homogeneous sphere model and the 500 layered-sphere model are minimal. The differences against ADDA-

SAM results decrease from 5 to 0 dBZ as the liquid equivalent snowfall rate increases from 0.001 to 0.1 mm/h. As discussed in the previous section for the $Z_{hh} - IWC$ relations this characteristic is due to the relative importance of small particles in the used PSDs. For more significant amounts of precipitation rate (larger than 0.1 mm/h) the Z_{hh} computed with the ADDA-SAM model are larger than those computed with the soft-sphere model. The observed differences increases up to 3 dBZ as the snow rate increases to 1 mm/h, due to the larger amount of particles with size parameter larger than 3 included in the PSD.

For W band the reflectivity computed using the 500 layered-sphere model is 3 dBZ greater than that computed using the homogeneous sphere model. The ADDA-SAM results are equivalent to the homogeneous sphere results for liquid-equivalent snowfall rates of the order of 0.01 mm/h and become equivalent to those obtained with the 500 layered-sphere model for snowfall rates of the order of 1 mm/h. The Mie-SAM and ADDA-SAM computed Z_{hh} are very similar principally due to the large amount of small particles included in the considered particle size distributions. A sufficiently large number of particles with size parameters larger than 5 are necessary to originate significant differences between the two models.

Given the importance of the $Z - SR$ relation at W-band (94 GHz), which is the frequency of the cloud profiling radar on board the CloudSat satellite and the planned EarthCARE and ACE missions, in figure 4.12 the calculated $Z - SR$ relationship derived for the aggregates (and using all the three fall speed-size relations discussed above) is compared to other results published in literature. This comparison shows that the sensitivity of the derived Z-SR relationship to the assumed fall speed-size parameterization is much less than the spread observed for the other Z-SR relationships.

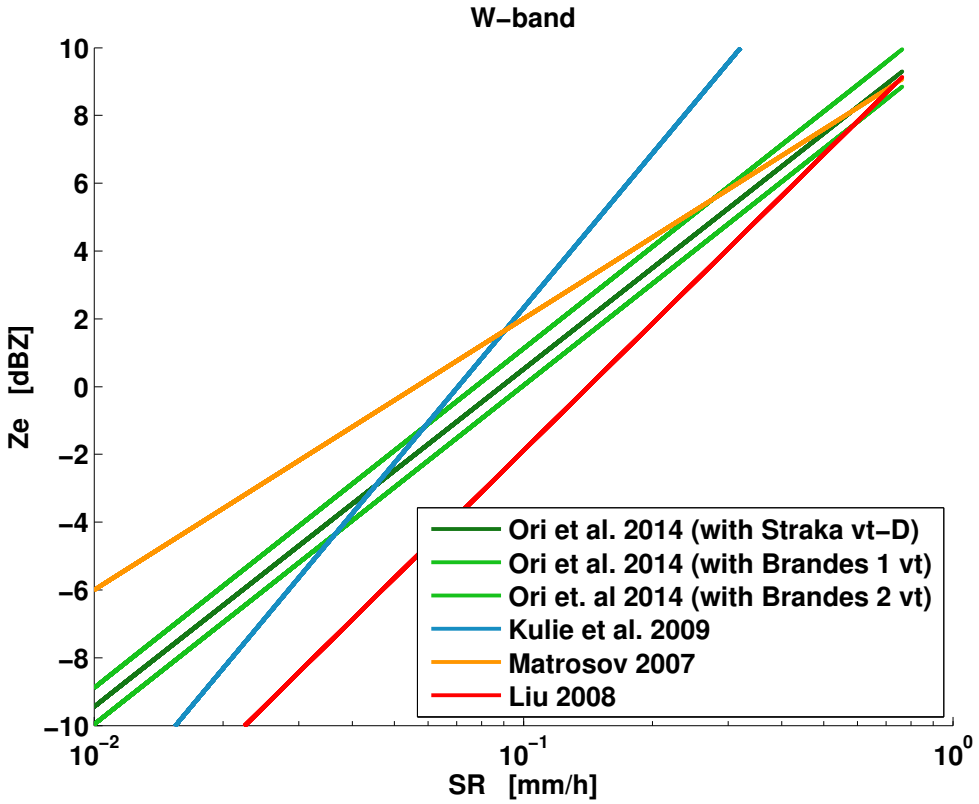

Fig. 4.12 Various Z -SR relationships at W band are compared. The SAM aggregates Z-SR relation is evaluated for the different fall speed-size formulas (green lines). The Z-SR relationships of Kulie and Bennartz (2009) (blue line) Matrosov (2007) (orange line) and Liu (2008b) (red line) are shown for comparison.

4.4 Acceleration of scattering computation

The flexibility of the DDA algorithm to simulate arbitrary shaped particles makes it a perfect choice for investigating the scattering properties of complex aggregate snowflakes. This advantage comes with the payback of a huge algorithmic complexity and thus a large computational cost.

Even though the ADDA code is one of the most efficient implementation of the DDA methodology (Penttilä et al., 2007) the solution for the wet aggregate problem with maximum size of 15 mm required 450 core hours of computation for a single frequency. This fact constitutes a huge limitation in the applicability of DDA to large amount of different particles. A more efficient implementation of the DDA algorithm is required to address this problem.

Recently the use of computing accelerators with massively parallel architectures has become more and more popular in the field of high performance computing. One of the most utilized accelerator architecture is the general purpose graphic processing unit. This architecture makes use of the computing capabilities of graphic processing units (GPUs) to solve generic algebra problems. The large availability of GPU on consumer level workstations makes easy to develop and prototyping scientific codes without the need to have access of large scale computing infrastructures.

The main difference between a GPU and a CPU is that the former has an extremely fine grained computing core along with an extremely fast access, but small sized memory (table 4.3). GPUs performs best on algebra problems that involves large matrices and vector. Basically, an enormous amount of simple tasks to be performed on tiny data.

The memory limitation of GPU computing constitutes the principal limitation to the applicability of DDA to GPU acceleration. The DDA algorithm for snowflakes with a maximum dimension of 15 mm required 110 GB of memory to be run. The memory requirement of the DDA is generally solved with the use of clusters of CPUs that can access a large amount of distributed memory. Unfortunately GPUs are mostly intended to work alone. The communications between different GPUs in a computing cluster usually requires a large overhead penalty. Moreover the computing efficiency parallel GPU computing rapidly decrease with the increase of the number of GPUs due to the large scalability requirements of GPU computing.

It has already been discussed (section 2.2.2) that the huge memory requirements of the DDA comes from the application of the FFT algorithm to solve the DDA problem as a convolution. This improvement in the DDA formulation changes the computational cost of the algorithm from $O(n^2)$ to $O(N\log(N))$ and at the same time changes the memory occupancy from $O(n)$ to $O(N)$, where n is the number of dipoles that constitutes the scattering

Table 4.3 Summary of the principal characteristics of low performance and high performance consumer grade CPUs and GPUs. The low performance devices has been used to develop and test sparse_ocl the high performance chips have been selected has reference for possible production implementations, with the same price point in the consumer market (currently around 210€). All performance data has been tested with the *clpeak*[4] testing software and has to be considered as peak performance. The performance measuring unit is the billions (Giga) of FLoating Point Operations Per Second (GFLOPS)

	CPU		GPU	
	i3-3217U	i5-4570	GF820M	R9-280X
Compute Units	4	4	2x48	32x64
Clock freq. [GHz]	1.8	3.2	1.5	1.1
Mem. Bandwidth [GB/s]	10	18	12	250
Mem. Capacity [GB]	4-8	8-32	1	3
Single Prec. GFLOPS	40	160	300	3800
Double Prec. GFLOPS	20	80	25	900

particle and N is the number of cells of the cubic lattice required to define the space occupied by the particles.

In cases when $n \ll N$, i.e. for very sparse (porous) particles, as it is the case for snow aggregates, the computational advantage of the FFT algorithm reduces and eventually vanishes. The lower memory occupancy of the non-FFT algorithm also allows to exploit the GPU architecture for DDA acceleration.

An experimental version of the non-FFT solution of the DDA algorithm has been implemented[3] and integrated in the existing ADDA software. For the implementation, the open computing language (OpenCL) has been chosen among other GPUs programming languages because it is an open standard, it is not dependent on specific vendor and it ensure the portability of the code to different architectures such as MICs and FPGAs. This implementation has been named *sparse_ocl*.

The performance of the sparse_ocl implementation of the ADDA code has been tested on a low grade laptop CPU (Intel i3-3217U) and GPU (Nvidia GeForce 820M) which are the "low performance" devices in table 4.3. Unfortunately it has not been possible to have access to a high power GPU to test the performance of the code in a case of use scenario.

[3] https://github.com/DaveOri/adda/tree/sparse_ocl
[4] https://github.com/krrishnarraj/clpeak

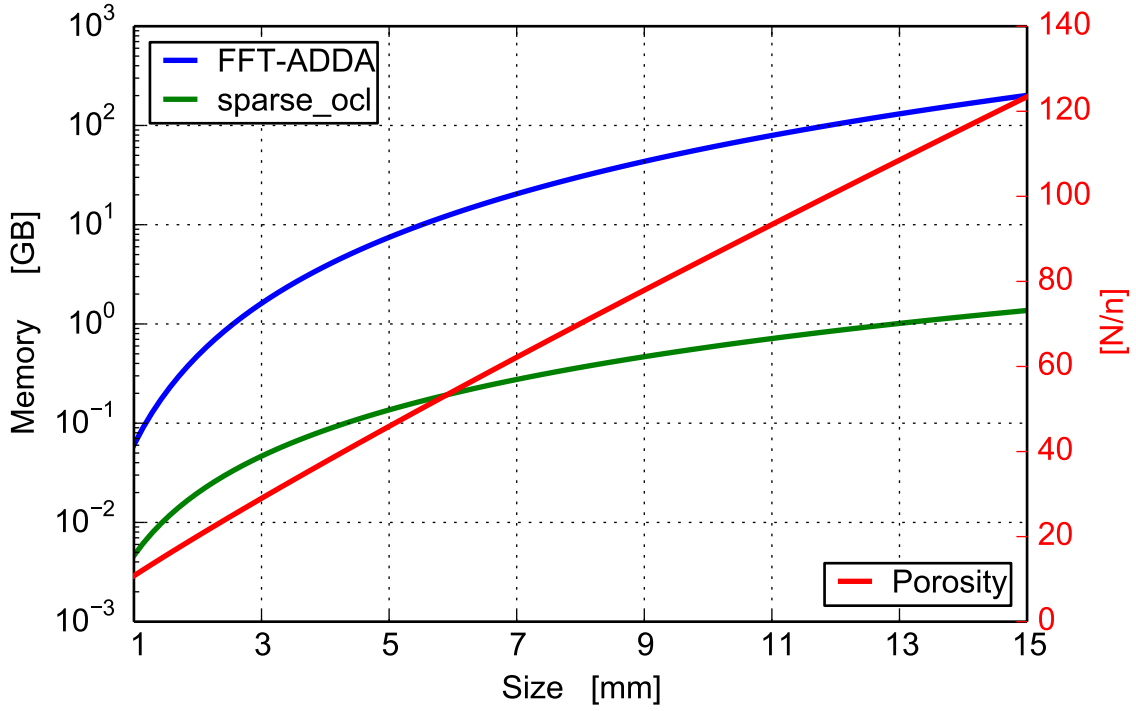

Fig. 4.13 Memory occupancy and porosity as a function of the snowflake size for the sparse_ocl and the ordinary FFT-ADDA implementations. The Brandes et al. (2007) mass-size relation is used to estimate the snowflake porosity

The relative computational cost of the sparse_ocl respect to the ordinary FFT-ADDA implementation depend on the grade "sparseness" (or porosity) of the target which will be defined as $R = N/n$.

It has been tested the memory occupancy required to perform the DDA computation with the two algorithm considering scattering particles that have a mass (number of occupied dipoles n) that follows equation 4.3. Considering a quasi-spherical particle the number N is determined by $(D/d)^3$ where d is the resolution of the cubic lattice grid. In this real case scenario the particle porosity is almost linearly increasing with the particle size. The results of this test are shown in figure 4.13. The memory occupancy of the sparse_ocl implementation increases as $O(D^{2.1})$ and remains smaller than 1 GB until D = 13 mm. On the contrary the ordinary FFT-ADDA routine breaks the 100 GB threshold for D =11 mm; at this scale of memory occupancy large computer clusters are needed to compute the DDA algorithm.

The relative performance of the two implementations from the computational time point of view are more difficult to measure. It is not straightforward to implement a computational test that involves different architectures and different codes at the same time. The most useful

test would be the application of the different strategies to actual snowflake targets, but since the computational power of the available GPU is very limited the test of the sparse_ocl code would take an enormous amount of time.

The sparse_ocl code is tested on the same hardware against an available OpenCL implementation of the ADDA code (Huntemann et al., 2011). The results of this comparison shows that the performance of the sparse_ocl implementation is larger than the FFT algorithm when the porosity of the particle N/n is larger than 80 (which corresponds to a snowflake of 9.5 mm with the considered mass-size relation). For porosity values smaller than 80 the FFT implementation is up to 2 times faster than sparse_ocl this maximum performance value is reached when the porosity is 40 (snowflake with maximum diameter of 3.5 mm).

The OpenCL implementation of the FFT-ADDA algorithm is reported to be 5 times faster than the corresponding CPU code on modern hardware, which is consistent with the different peak performance of the two architectures (table 4.3). Unfortunately the OpenCL implementation of the FFT-ADDA algorithm is bounded to be used for snowflakes with maximum dimension up to 3 mm due to the memory limitations, for larger snowflakes the sparse_ocl implementation is needed to exploit the GPU acceleration. Even if the sparse_ocl is less efficient than the OpenCL FFT-ADDA, for snowflakes with maximum diameter ranging from 3 to 9 mm it is expected to perform better than the CPU implementation.

The discussion on the possible performance of the implementation of sparse_ocl on a high power GPU highly speculative and it is based just based on relative performance respect to the actual implementation tested, but it gives some insight on the possible advantage given by the use of accelerators in scattering simulations.

Chapter 5

Retrieval of snow microphysical properties

Radar based quantitative precipitation estimation and microphysical characteristics retrievals rely on the knowledge of connection existing between the physical and scattering properties of hydrometeors. For liquid water droplets, because the relation between size and shape is unambiguous and well understood, only the drop size is needed to calculate its scattering properties. For frozen hydrometeors, on the other hand, the relation between particle dimension, shape and mass is not unique and depends on the snow type (Pruppacher and Klett, 1997).

When all the listed ice particle properties are known, it is customary to link microphysical and scattering properties of ice particles through an effective medium approximations (Sihvola, 1999). The degree of complexity needed both for describing snowflakes physical properties and their corresponding representation in the modeled scatterers depends on radar frequency.

At lower frequencies, where the Rayleigh approximation holds, only mass of ice particles is needed to calculate radar cross sections. At higher frequencies, also the shape starts to play a role and should be taken into account (Hogan et al., 2012; Matrosov et al., 2005a).

Various studies have proven that simple representation of snowflakes as spheroids with dielectric properties defined by an effective medium approximation may lead to significant errors, especially at cloud radar frequencies. Kulie et al. (2014); Leinonen et al. (2012), following the methodology described in Kneifel et al. (2011), have demonstrated that triple frequency (13 GHz, 35 GHz and 95 GHz) radar observations cannot be explained if only the simple spheroid models of ice particles are used.

Recently, Kneifel et al. (2015) have shown that deviations from the spheroid model occur in cases where large aggregates are present. This result is consistent with findings of Leinonen et al. (2013), showing that the back-scattering properties of ice particles at multiple frequencies can be described by and linked to the mass distribution in the snowflake. These studies demonstrate that the relation between physical snowfall properties and multi-frequency radar observations is not always straightforward.

Estimates of snowflakes microphysical properties performed with surface observations typically involve measurements of individual particles (Kajikawa, 1972; Mitchell et al., 1990; Nakaya and Tereda, 1935). These methods provide highly detailed descriptions of particles, but the inquired samples have necessarily been limited in number and short in duration due to the demanding technical effort. The development of automated methods for the retrieval of snow microphysical properties is therefore of uttermost importance to achieve a comprehensive knowledge of the natural variability of snow types.

In this chapter an automatic method for snow microphysical retrieval is presented. The developed strategy is based on the observed differences between two definitions of snow bulk densities. The procedure aims at retrieving snowflake mass-dimensional relations from co-located measurements of effective radar reflectivity factor in Rayleigh regime, liquid water equivalent accumulation and ice particle volume flux.

The proposed method yields mass-dimensional relations that are consistent with radar, gauge and particle video imager observations. The retrieved relations are than compared with those obtained by applying general hydrodynamic theory to 2D-video disdrometer (2DVD) measurements (Böhm, 1989; Huang et al., 2015). Since the 2DVD hydrodynamic method relies on a completely different instrumentation and retrieving methodology, this comparison is a significant cross validation test of both procedures.

An ad-hoc procedure was appointed to test the robustness of the relation between snow microphysical and scattering properties across multiple radar frequencies. Ka- and W- band radar reflectivity observations were calculated using T-matrix method from retrieved mass-dimensional relations and particle video observations. These reflectivity simulations has been compared against Ka- and W-band cloud radar measurements. It is shown that there are instances where this relation breaks, especially for the higher frequency band. The evaluation of the method performance is addressed using data collected during the Biogenic Aerosols Effects on Clouds and Climate field campaign (BAECC) that took place in Finland in 2014.

The work presented in this chapter is expected to be published in a scientific journal article currently under preparation (Ori et al., prep) and to be submitted to *Atmospheric Measurement Techniques*.

5.1 Methodology

The theoretical aspects of the retrieval methods are introduced to emphasize the importance of the physical basis of the methodology. The instrumentation setup and the actual implementation of the retrieval processes is described in the next section.

5.1.1 Moments ratio

The proposed retrieval algorithm, namely the Moment's Ratio Retrieval Method (MRRM) makes use of measured PSDs, fall velocities, snow accumulations and near Rayleigh radar reflectivities.

The general precipitation accumulation measured by a snow gauge during a certain time interval Δt is given by

$$G(t,\Delta T) = \frac{1}{\Delta T}\int_{t}^{t+\Delta t}\int_{\min(D)}^{\max(D)} m(D,t)\, v(D,t)\, N(D,t)\; dD\, dt \tag{5.1}$$

where $N(D)$ is the particle size distribution, $m(D)$ is the mass-size relation and $v(D)$ is the velocity-size relation of the precipitating particles. In equation 5.1 and through the rest of the chapter the characteristic size of the particle D is the equivalent volume diameter D_{vol}, so that the volume of the particle is defined as $V = \frac{\pi}{6}D^3$.

According to general assumption validated by numerous field studies, mass-size and velocity-size relations obey to power law expressions

$$\begin{aligned} m(D) &= \alpha D^{\beta} \\ v(D) &= \gamma D^{\delta} \end{aligned} \tag{5.2}$$

As a consequence the precipitation accumulation $G(t,\Delta t)$ could be expressed in terms of moments of the particle size distribution

$$\begin{aligned} G(t,\Delta T) &= \frac{1}{\Delta T}\int_{t}^{t+\Delta t}\int_{\min(D)}^{\max(D)} \alpha D^{\beta}\, \gamma D^{\delta}\, N(D,t)\; dD\, dt \\ &= \frac{1}{\Delta T}\int_{t}^{t+\Delta t} \alpha\, \gamma M_{\beta+\delta}\; dt \end{aligned} \tag{5.3}$$

Where the general definition of the k-th order moment M_k of distribution $f(x)$ has been applied

$$M_k = \int_{-\infty}^{\infty} x^k\, f(x) dx \tag{5.4}$$

From PSD and fall velocity measurements, the time averaged snow volume flux $V_f(t,\Delta T)$ is defined and expressed in terms of moments of the particle size distribution

$$\begin{aligned} V_f(t,\Delta T) &= \frac{1}{\Delta T}\int_t^{t+\Delta t}\int_{D_{min}}^{D_{max}} \frac{\pi}{6} D^3 v(D,t) N(D,t)\, dD\, dt \\ &= \frac{1}{\Delta T}\int_t^{t+\Delta t}\int_{D_{min}}^{D_{max}} \frac{\pi}{6} D^3 \gamma D^\delta N(D,t)\, dD\, dt = \frac{1}{\Delta T}\int_t^{t+\Delta t} \frac{\pi}{6}\gamma M_{3+\delta}\, dt \end{aligned} \tag{5.5}$$

Combining equations 5.3 and 5.5 and assuming that microphysical characteristics of snowfall do not change too much over the time interval $(t,t+\Delta t)$ it is possible to write the snow rate weighted bulk density in terms of ratio of moments of the particle size distribution

$$\rho_{SR} = \frac{G(t,\Delta T)}{V_f(t,\Delta T)} = \frac{6\alpha}{\pi}\frac{M_{\beta+\delta}}{M_{3+\delta}} \tag{5.6}$$

It is well known that for Rayleigh scattering, and using the Maxwell-Garnet mixing formula (ice inclusion i air matrix), the equivalent radar reflectivity factor can be expressed as

$$Z_e(t,\Delta T) = \frac{1}{\Delta T}\int_t^{t+\Delta t} \frac{|K_{ice}|^2}{\rho_{ice}^2 |K_w|^2}\int_{D_{min}}^{D_{max}} \rho_{snow}^2(D)\, D^6 N(D,t)\; dD\, dt \tag{5.7}$$

The general derivation of equation 5.7 can be found in appendix A.1. Equation 5.7 is equivalent to the integral over the particle size distribution of the squared mass-size relation.

$$\begin{aligned} Z(t,\Delta T) &= \frac{1}{\Delta T}\int_t^{t+\Delta t} \frac{|K_{ice}|^2}{\rho_{ice}^2 |K_w|^2}\int_{D_{min}}^{D_{max}} \left(\frac{6}{\pi}\right)^2 \alpha^2 D^{2\beta} N(D,t)\, dD\, dt \\ &= \frac{1}{\Delta T}\int_t^{t+\Delta t} \frac{|K_{ice}|^2}{\rho_{ice}^2 |K_w|^2}\left(\frac{6}{\pi}\right)^2 \alpha^2 M_{2\beta}\, dt \end{aligned} \tag{5.8}$$

Equation 5.7 is commonly used to derive the reflectivity weighted bulk density ρ_Z from PSD and Z measurements (Bringi and Chandrasekar, 2001, pp.234-235). First, we define Z_{ice}, which corresponds to equation 5.7 where $\rho_{snow}(D) = 1$

$$Z_{ice} = \frac{1}{\Delta T}\int_t^{t+\Delta t} \frac{|K_{ice}|^2}{\rho_{ice}^2 |K_w|^2}\int_{\min(D)}^{\max(D)} D^6 N(D,t)\, dD\, dt = \frac{1}{\Delta T}\frac{|K_{ice}|^2}{\rho_{ice}^2 |K_w|^2}\int_t^{t+\Delta t} M_6\, dt \tag{5.9}$$

It is now straightforward to define the square of the reflectivity weighted bulk density and to express it in terms of moments of the particle size distribution

$$\rho_Z^2 = \frac{Z(t,\Delta T)}{Z_{ice}(t,\Delta T)} = \left(\frac{6}{\pi}\right)^2 \alpha^2 \frac{M_{2\beta}}{M_6} \tag{5.10}$$

Eq. 5.6 and 5.10 are both a representation of the snowflake bulk density, but since they are weighted with distinct moments of the particle size distribution they are inherently different.

The difference between ρ_{SR} and ρ_Z is strictly related to the snow microphysical parameters. In particular when the ratio between the squared values of these two quantities is calculated, the dependence to the α parameter vanishes. This ratio is particularly useful because it represents the difference between the Rayleigh reflectivity calculated with the two different definitions of bulk density.

$$\frac{\rho_{SR}^2}{\rho_Z^2} = \frac{M_{\beta+\delta}^2 M_6}{M_{3+\delta}^2 M_{2\beta}} = \Delta Z \tag{5.11}$$

It is possible to give a rough estimate of the ratio ΔZ considering a PSD in the general shape of inverse exponential which has been found to adequately represent the size distribution of snow (Heymsfield et al., 2008).

$$N(D) = N_0 \, e^{-\Lambda D} \tag{5.12}$$

Under this assumption, the general moment M_k of the PSD reads

$$M_k = \int_0^\infty N_0 \, D^k \, e^{-\Lambda D} \, dD = \frac{N_0 \Gamma(k+1)}{\Lambda^{k+1}} \tag{5.13}$$

where $\Gamma(k+1)$ is the complete gamma function.

Equation 5.11 can then be expressed in analytic form in terms of β and δ.

$$\frac{\rho_{SR}^2}{\rho_Z^2} = \Delta Z = \left(\frac{\Gamma(\beta+\delta+1)}{\Gamma(4+\delta)} \right)^2 \frac{\Gamma(7)}{\Gamma(2\beta+1)} \tag{5.14}$$

When the PSD assumes the form of an inverse exponential, equation 5.11 depends on β and δ only and all PSD related parameters vanish. The theoretical results of equation 5.14 are shown in figure 5.1. ΔZ is always positive for values of β and δ commonly observed in nature and thus ρ_Z is always smaller than ρ_{SR}. The minimum values of ΔZ are reached when β is close to 3, i.e. when snow is mainly composed of dense ice particles such as tiny crystals or heavily rimed snowflakes. Conversely, when snow is composed of large fluffy aggregates β values are expected to decrease to values around 2 leading to a ΔZ increment up to 6 dBZ.

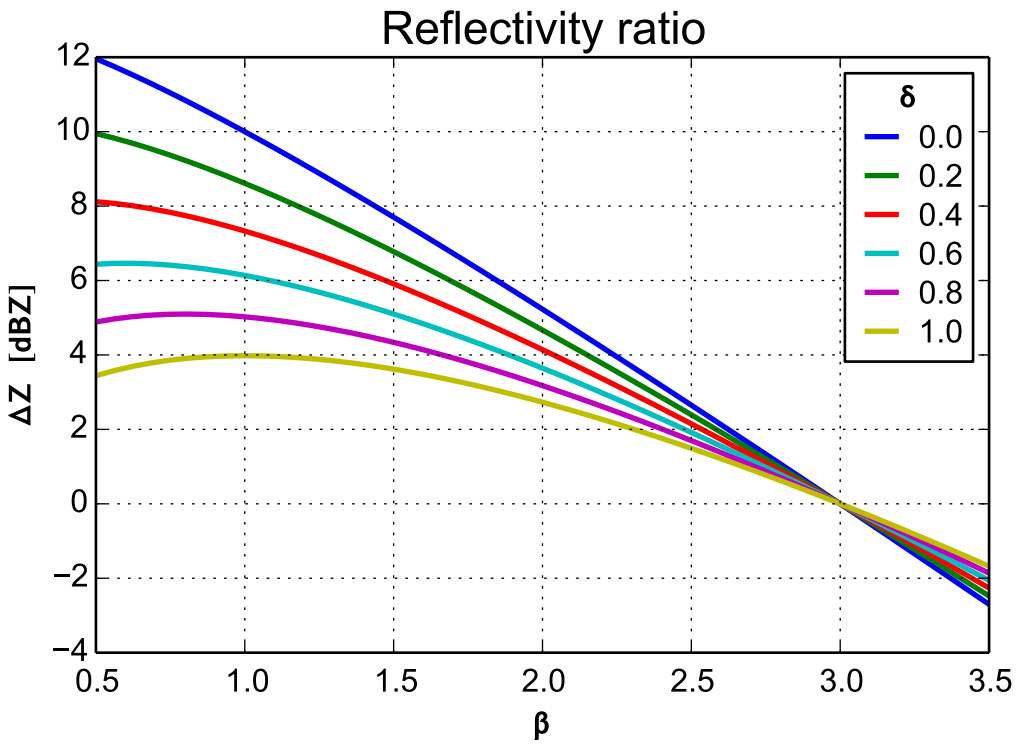

Fig. 5.1 Theoretical relation between ΔZ and β for various values of δ. β and δ are exponents of respectively the mass-size and velocity-size relation for snowflakes in the power law form. ΔZ is the difference between the radar reflectivity calculated with PSD integrated snow bulk density and the measured radar reflectivity in the Rayleigh scattering regime. This theoretical study assumes that snow PSD takes the inverse exponential form.

Uncertainties

The presented MRRM algorithm lacks of a rigorous estimation of the uncertainties associated with the retrieval results. Subsequent section will describe the utilized observation instruments, discussing the possible sources of measurement errors and the strategies adopted to minimize them. However the retrieval process is based on equation 5.11 which is highly non linear and not invertible. This fact implies that it is not possible to perform an error propagation analysis and a numerical experiment should be performed instead.

The presented study used the independent 2DVD instrument and Böhm's method to validate the performance of the MRRM algorithm and is primarily focused on the consistency of independent snow measurement including high-frequency Ka and W-band radar reflectivity simulations using DDA-calculated scattering properties (section 6.1).

Equation 5.14 gives the analytic solution of the MRRM algorithm under common observed snowfall conditions (i.e. PSD nearly inverse exponential). The analysis shows that the

methodology is not sensitive to the PSD parameters. It is also shown that the β parameter is not much sensitive to the value of δ. In the worst case scenario of extremely low dense snowflakes β is expected to be approximately 1.5, $\Delta Z \approx 7$ dBZ and $\delta \approx 0.1$; an error in the estimation of the δ parameter of the order of 0.1 would cause a deviation in the retrieved β value of $\delta\beta \approx 0.15$. The retrieval of the β parameter is more sensitive to the value of ΔZ. An error in the estimation of ΔZ of 1 dBZ could cause uncertainties in the retrieved β parameter up to 0.5. The estimated uncertainties are worst case conditions and are similar to those found in other methods (Wood et al., 2015). However, any bulk microphysical retrieval method is based upon assumption about the mathematical form of the mass-size relation (power-law). The actual population of particles hardly follows exactly a power-law fit, especially when multiple types of particles are present at the same time. An assessment of the possible impacts of such oversimplified assumptions is still lacking.

Other microphysical retrieval schemes are under rapid development and address the problem of estimate the retrieval uncertainties. Wood (2011) proposed a sophisticated methodology based on Bayesian optimal retrieval method which provides retrieval of snow microphysical parameters in terms of probability density functions (PDF). The PDF information brings both the best estimate and the associated uncertainty of a given parameter. The Wood (2011) procedure makes use of advanced statistical methods that hides the mathematical foundation of the microphysical retrieval (i.e. the sensitivity of different measuring technique to distinct moments of the particle size distribution). The MRRM algorithm gives deeper insights on the physical principle that provides the possibility to estimate the mass-size relation from multiple bulk measurements. Moreover, respect to the Wood (2011) technique the MRRM does not require the availability of a 2DVD instrument, which is still not affordable to many operational weather institutions.

5.1.2 Böhm's method

Böhm (1989) developed a hydrodynamic model which makes use of the particle mass and the mean effective projected area in the direction of the air flow to predict the terminal fall velocity of solid hydrometeors. Since the 2-dimensional video disdrometer can measure both particles fall speed and their projected areas, the 2DVD observation can be used to retrieve particle mass value by inverting Böhm's model.

The first step of the Böhm's method is the calculation of the *Reynolds number* R_e

$$R_e = \frac{2\,\rho_a\, v_t}{\nu_k}\sqrt{\frac{A}{\pi}} \tag{5.15}$$

where A is the characteristic area of the particle, in this case the area of the smallest circumscribed ellipse that completely encloses the particle image (silhouette). The air cinematic viscosity ν_k and density ρ_a are computed from measured air pressure, temperature and humidity (Weast et al., 1989). Then, a fixed relation between R_e and the Davies[1] number X is assumed.

$$X = \left[\frac{\left(\sqrt{R_e/8.5} + 1 \right)^2 - 1}{0.1519} \right]^2 \tag{5.16}$$

Finally, the particle mass can be derived from the definition of the Davies number

$$m = \frac{\pi \nu_k^2 X}{8 g \rho_a} \sqrt[4]{\frac{A_e}{A}} \tag{5.17}$$

where g is the mean terrestrial gravity acceleration and A_e is the particle projected area in the flow direction. Mass data along with the particles fall speed and diameter are collected for a certain period of time, so that a power law fit of the form $m = \alpha D^\beta$ can be estimated with a general least-square fitting method.

As it will be shown in section 5.2.1 the effective projected area measured by the 2DVD is observed from a side of the falling particle and not from the falling direction. However, Szyrmer and Zawadzki (2010) have demonstrated that it is reasonable to assume the area ratio $A_r = A_e/A$ of falling snowflakes projected to a plane normal to the air flow (which is the quantity that appears in equation 5.17) to be equal to the area ratio observed from a side view. The method also assumes that the measured fall speed equals the terminal fall speed of the precipitating particle. The 2DVD should be protected by a wind fence to avoid measurement errors related to wind drifts and turbulence.

5.2 The BAECC campaign

The data used in this study were collected during the Biogenic Aerosols Effects on Clouds and Climate (BAECC) field campaign that took place at the University of Helsinki Hyytiälä Forestry Field Station, Finland (61° 50'37.114"N, 24° 17'15.709"E, 150 m above mean sea level). BAECC was organized in collaboration between the University of Helsinki (UH), the Finnish Meteorological Institute (FMI), and the United States Department of Energy Atmospheric Radiation Measurement (ARM) program, which deployed the second Mobile Facility (AMF2) from 1 February to 12 September 2014. The AMF2 remote sensing

[1]The Davies number X is also known as the Best number

Fig. 5.2 Photo of the measurement site taken on Jan 29, 2014 showing in-situ and remote sensing instruments deployed during the BAECC campaign 2014.

instruments and part of the in situ precipitation sensors are shown in figure 5.2. Three snow events has been selected to test the moment ratio retrieval method (MRRM), namely those occured on February 12nd, 15-16th and 21-22nd, 2014.

5.2.1 Installation and instruments

The measurement field is a 60 by 70 m unvegetated surrounded by trees. Most of the ground instruments were located in the middle of the field at about 20 m distance from the nearest trees. These last act as a wind shield, protecting the measurement site from strong wind and making it favorable for snow measurements. In addiction a Double-Fence Intercomparison Reference (DFIR) wind protection (Rasmussen et al., 2011) was built in loco to protect the 2DVD instrument. The ground-based precipitation data set includes PSDs, terminal fall velocities, and particle shapes measured with 1-D and 2-D optical disdrometers and a 2-D imaging video camera. Furthermore, liquid equivalent precipitation rate, total accumulation, and snow depth were measured. Close to the two disdrometers two 3D-anemometers have been installed to quantify the wind drift and turbulence. Generally the wind conditions are very moderate at the site because of shelter of the nearby trees. During the three events discussed in this study the mean wind speed was about 2 m/s or lower.

The remote sensing instruments were located nearby the ground precipitation measurement equipment and include two scanning cloud radars (X-, Ka- bands) and two vertically pointing cloud radar (Ka-, W- bands). The remote sensing equipment is completed with the ARM microwave radiometers (MWR). The atmospheric state profile was derived four times per day from radio soundings (RS). The subset of BAECC instruments used in this

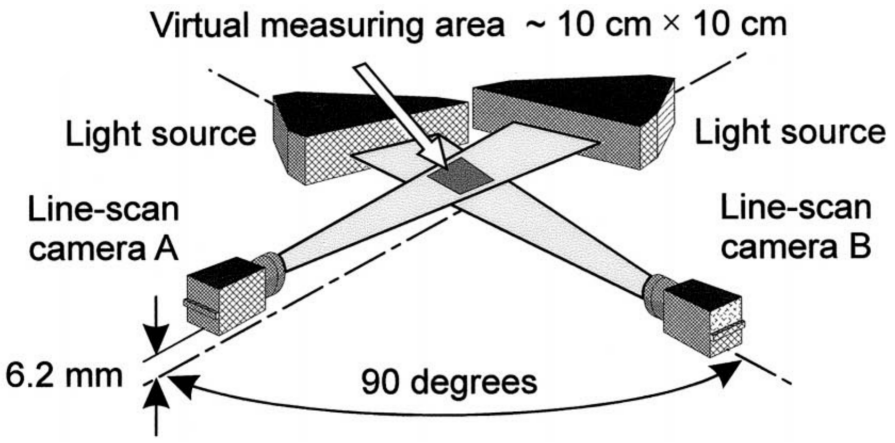

Fig. 5.3 Scheme of the observation geometry and measurement principle of the 2DVD. Image taken from Kruger and Krajewski (2002)

study (snow gauge, particle video imager, cloud radar and 2D-video disdrometer) and data processing methods adopted are presented in more detail in the following.

2-Dimension Video Disdrometer (2DVD)

The 2DVD (Kruger and Krajewski, 2002) uses two orthogonal optical paths to measure hydrometeors shape and fall velocity. Both paths are generated from a generic light source in series with a Fresnel lens giving a collimated uniform light emission. A line scan camera measures the shadow projected by hydrometeors falling through the light rays. The two optical paths are vertically separated, and by measuring the difference in respective time passages it is possible to determine the particle fall velocities. A schematic representation of the 2DVD observation principle is given in figure 5.3.

The 2DVD gives front and side views (silhouettes) of falling particles. It is worth to note that the field of view of the two distinct cameras does not coincide and the instrument software needs to discriminate the particles detected at both planes from the general single camera signals. The measuring area of each camera is approximately 250 cm^2 and the virtual measuring area of the 2DVD where the fields of view of the two cameras cross each other is 100 cm^2 (figure 5.3). Fall speeds and particle count are measured only if the two camera record images of the same particle. The improved matching algorithm of Huang et al. (2010) is used to avoid incorrect particle matching which can cause substantial errors in the measured PSDs and velocities.

An ad-hoc image processing software has been installed to make the 2DVD measuring the particle equivalent volume diameter $V = \pi D_{vol}^3/6$. At first, the minimum ellipses that

Fig. 5.4 PIP instrument installation. The camera is located in the heated housing on the right of the image, while the lamp is on the left. Image taken from Newman and Kucera (2009)

enclose the two projected silhouettes are defined, than it is estimated the volume of the 3D minimum ellipsoid that encloses the particle.

The mean PSD, velocity-size and mass-size relationships derived with the Böhm's method are calculated averaging the observations over a fixed 5-minute time interval.

The 2DVD has been installed inside a Double-Fence Intercomparison Reference (DFIR) wind protection (Rasmussen et al., 2011) and on top 3 m tall pedestal to protect the instrument from wind drift and near ground turbulence. During the BAECC campaign, precise measurement of 3D wind direction and speed inside the wind fence was performed continuously with a high temporal resolution 3D sonic anemometer.

Particle Image Packaging (PIP)

For the present study, the most important instrument is probably the Particle Imaging Package (PIP), which is an upgraded version of the Particle Video Imager (PVI), also known as Snow Video Imager (SVI) (Newman and Kucera, 2009).

The PIP instrument includes a halogen lamp and a charge-coupled device (CCD) video camera that captures pictures of backlit hydrometeors within its focal area (figure 5.4). The frame rate of PIP is 380 frames per second enabling the measurement of particle fall velocities. The distance between the camera and the lamp is approximately 2 m, and the focal plane is 1.3 m from the camera. The field of view at the focal distance is 64 x 48 mm and the image resolution is 0.1 mm.

Terminal fall velocity and other particle image properties are derived according to the SVI particle detection algorithm described in Newman and Kucera (2009). The image processing

algorithm excludes the particles which are out of focus according to thresholds based on increased blurring and reduced contrast values.

PIP measurements are minimally affected by wind-induced errors due to the open structure of the instrument and the spatial measurement technique, thus the PIP instrument is installed in the open field. Nonetheless 3D wind speed and direction are continuously measured with a sonic anemometer.

Since PIP measures particles in a volume, not in a plane like the 2DVD previously described, it allows evaluating the concentration of the particles in the air rather then the rainfall or snowfall rate at the ground. As a camera-based system, the PIP can also record the images (actually the video) of falling snowflakes and thus, it can be used to distinguish between the different types of snowflakes (crystals, aggregates of needles, aggregates of spatial crystal or rimed particles).

PSD is recorded by the PIP instrument in minute intervals for size ranging from 0.125 to 26.125 mm, but particles smaller than 0.375 mm have been excluded since it has been reported that their size could be inaccurate. Spurious large individual particles have been also excluded before averaging the PSD.

PIP measures equivalent area diameter D_{ec} which is defined as the diameter of a disk that has the same area as the shadow of the particle. For consistency with the 2DVD data, the estimated particle sizes are converted to the *volume-equivalent diameter*[2] with a constant correction factor $D_{vol} \approx 1.11 D_{ec}$. This correction term is estimated with a theoretical and statistical analysis by rotating tri-axial ellipsoids and examining the mean difference produced by the two diameter definitions, in analogy with Wood et al. (2013). The ellipsoid size, aspect ratio and orientation are varied among the natural range of observed snowflakes. Details of this study can be found in appendix B.

From the real time PIP observations of fall velocities v and particle size D_{vol}, fall velocity-diameter power law relations in the form $v(D_{vol}) = \gamma D_{vol}^{\delta}$ are calculated. Prior to carrying out the nonlinear regression fit with Levenberg-Marquardt algorithm, a two-dimensional probability density distribution of velocity-diameter observations is calculated with the kernel density estimation method (Silverman, 1986).

This method was selected since it provides a consistent approach to reduce the impact of limited observations of large particles and outliers. In particular, to minimize the influence of outliers on the $v - D$ fit, while preserving most of reliable observations, the regression is evaluated only over those velocity records which, for each diameter bin, fall within the half width from each side of the peak of the measured velocity density function. It should

[2] In analogy with the equivalent area diameter D_{ec}, the volume-equivalent diameter is defined as the diameter of a sphere that has the same volume of the minimum ellipsoid that encloses the particle

be noted that the half widths are calculated for each side of the distribution, allowing for non-symmetrical density functions.

Snow gauge

Along with the two optical disdrometers, the snow rate and snow accumulation is measured by two OTT-Pluvio^2 all-weather weighting gauges, which allows measuring the amount and intensity of rain, snow, and hail. The Pluvio200, with an area of the orifice A_G = 200 cm^2, and Tretyakov wind shield (Lanza et al., 2006) were placed inside the DFIR wind fence; the Pluvio400, with an orifice A_G = 400 cm^2, and a combination of Tretyakov and Alter wind shields (Lanza et al., 2006) were installed on the measurement field outside the DFIR fence. On average, the differences in snowfall rate or snowfall accumulation, as measured with the two gauges, are found to be smaller than 10% during the all BAECC campaign and of very minor influence within the snow events analyzed in this study.

It should be pointed out that the factory-made filtered data output non-real time accumulation is utilized. This output has a time delay of 5 minutes from the precipitation event, but it provides higher accuracy in measured accumulation. Due to problems with the clock synchronization of the data acquiring computer for the gauges, data timings needed to be corrected from the drifting system offset by cross correlating the time series of precipitation rate with the values derived from PIP for each case.

Radars

For this analysis, data from the scanning X-band ARM cloud radar system (XSACR), from the Ka band zenith pointing radar (KAZR) and from the Marine W-band ARM cloud radar (MWACR) were used. The technical specification of the radars employed in this study are given in table 5.1. All ARM radars were mounted on top of containers to prevent the signal of scanning radars to be disturbed by the surrounding trees and also to accommodate the electrical and computing infrastructures needed to operate the systems.

All radar observations used in this study were collected during zenith-pointing operations. The KAZR and MWACR were continuously vertically pointing during the campaign. The XSACR performed alternating scans and vertically pointing observations. In order to increase the amount of data, the observations collected during the zenith passage of the range height indicator (RHI) are used along with the pure vertically pointing measurements.

The two-way attenuation profile due to water vapor has been derived by Kneifel et al. (2015), using the measurements from the closest RS and the molecular absorption model by Rosenkranz (1998) updated with the most recent findings on the water vapor spectral

Table 5.1 Technical Specifications of the AMF2 precipitation and cloud radars installed at the Hyytiälä forestry field station during the BAECC campaign

Specifications	XSACR	KAZR	MWACR
Frequency (GHz)	9.7	34.9	95.1
Waveform	Short	Pulse compression, short	Short
Pulse width (ns)	333	4000, 333	333
3dB Beam Width (°)	1.4	0.3	0.3
Sensitivity [3]at 2km (dBZ)	-12	-29, -13	-29
Range resolution (m)	50	60, 50	50
Gate spacing (m)	25	25	25
Dwell Time (s)	2	2	2

absorption. Due to the relatively moist atmosphere (vertically integrated water vapor amounts were in the range of 10-13 kg/m^2), the attenuation especially affects the W-band with PIA up to 1 dBZ within the lowest 5 km. At Ka and X-band the water vapor attenuates the signal by less than 0.2 dBZ and 0.02 dBZ respectively and can thus be neglected.

The attenuation due to snowfall has been estimated using the available snow rate data. Since the present study uses only the reflectivity measurement at the first coincident gate available for the three radars (approximately 400 meters above the ground) and the analyzed precipitation events are of relatively low intensity, the attenuation due to two-way path in the snowfall is negligible for X and Ka band. The observed path integrated W-band attenuation values are in the order of 1 dBZ which is similar to the findings of Matrosov (2007). Also the attenuation due to supercooled liquid water has been evaluated and corrected using liquid water path data derived from the colocated MWR (Cadeddu et al., 2013), the temperature profile from the closest RS and the absorption model of Ellison (2007).

The offset due to radome attenuation has been analyzed looking at the radar noise floor at range gates without cloud particles, which can be expected to vary due to emission by the liquid water included in a wet snow layer accumulating on the radome; during all three cases and for all three radars, the noise floor indicated no significant changes and thus no significant radome attenuation.

Relative attenuation and calibration differences between the three radars have been constantly monitored by comparing the radar measurements in regions close to cloud top where we can expect the ice hydrometeors to be mostly Rayleigh scatterers and thus their equivalent reflectivity factors are expected to be independent from frequency (section 2.3.1). The resulting discrepancies are in the order of 1 dBZ.

[3]Radar sensitivity is calculated for a single pulse

The absolute calibration of the radar systems, that have been performed at the beginning of the campaign with a corner reflector, failed for technical difficulties. The radar reflectivity profile measured by XSACR has been compared with the C-band reflectivity measured by the nearby Ikaalinen scanning radar of the Finnish weather radar network. A nearly perfect match between the two profiles has been found; details of this comparison are given in appendix A.2. The absolute calibration of the Finnish radar network has been recently tested using the *self-consistency theory* (Gorgucci et al., 1992). These tests found that the C-band radar used for the comparison is out of calibration by -3 dBZ. The reflectivity values given by the BAECC radar has been then corrected according to this result.

Depending on the horizontal precipitation advection speed, a temporal lag between the radar signal and the ground measurements is expected. The simultaneous measurement of reflectivity, snow accumulation and particle size distribution is vital for the performance of the retrieval method, therefore, the time lag between radar and ground observation has been estimated with two different methods (Kneifel et al., 2015) for each snow event.

First, the theoretical Rayleigh reflectivity time series are calculated from the sixth moment of the ground observed PSD and the time lag is estimated from the maximum value of the lagged cross correlation between the estimated Z time series and the observed X band radar time series. In the second method, the horizontal wind profile, from the nearest RS, has been used along with observed mean Doppler vertical velocity (MDV) to simulate the resulting fall streak pattern in the radar time-height observation space similar to (Hogan and Kew, 2005). The time lag is calculated by extrapolating the fall streak pattern to the ground level.

The time lag estimates, obtained by these methods, differ by less than 0.5 min for the three analyzed cases. The measured reflectivity time series has been shifted forward according to the average lag obtained by the three methods of 3.0, 3.8, and 1.0 min for the 12nd, 15th-16th, and 21-22 of February 2014 respectively.

5.2.2 Methodology

To combine observations from precipitation sensors and X-band cloud radar, data are averaged over variable time intervals determined by fixed amount of snow accumulation recorded by the precipitation gauge. Since the gauge minimum detectable liquid water equivalent accumulation is 0.1 mm (Brandes et al., 2007), the threshold value is typically selected as an integer multiple of this quantity, and in this study a value of 0.2 mm is used. It has been decided to select the integration periods as short as possible while limiting measurement errors.

According to this averaging time interval the MRRM is applied. The value of δ is derived from PIP velocity fits. Equation 5.11 is used to retrieve the value of β through an iterative

minimization procedure. After β is obtained, the α coefficient is then calculated using equation 5.1 and matching gauge observations.

The retrieval procedure could be described with the following steps:

1. The series of temporal integration intervals $(t, t+\Delta t)$ are defined by the snow gauge data. For each time interval, a fixed amount of liquid water equivalent accumulation of $G = 0.2$ mm is measured.

2. The particle count and size data recorded by the PIP instrument are averaged over the defined time intervals obtaining the time averaged PSDs $N(D)$. Also the reflectivity time series $Z_e(t, t+\Delta t)$ are obtained averaging the radar measurements according to the same time intervals.

3. For each time interval $(t, t+\Delta t)$, a power law velocity fit $v(D) = \gamma D^{\delta}$ is obtained from the PIP velocity measurements applying the Levenberg-Marquardt nonlinear regression algorithm.

4. The snow rate weighted bulk density $\rho_{SR}(t, t+\Delta t)$ and the reflectivity weighted bulk density $\rho_Z(t, t+\Delta t)$ are calculated using equation 5.6 and equation 5.10 respectively. The ΔZ parameter is obtained from the ratio ρ_{SR}^2/ρ_Z^2.

5. Using the estimated ΔZ and δ quantities, the β parameter of the mass-size relation is calculated applying the iterative root-finding Brent's method (Stage, 2013) to equation 5.11. The remaining α parameter is than easily found from equation 5.1, which is linear respect to α, by matching the accumulation G with the results of equation 5.1.

The 2DVD measurements are averaged over a fixed time interval of 5 minutes. The Böhm's method is applied to the 2DVD data time series providing a completely independent estimation of snow particles mass-size relations. The 2DVD data are also used to check PIP fall velocity and PSD measurements. Given the complementary limitations of the used particle imaging instruments the cross-comparison of the measured data provides a reliable validation of the accuracy of both measurements.

The mass dimensional relations obtained from the moment's ratio and the Böhm's method are cross checked against the observed data. Equation 5.1 is used to calculate the expected gauge accumulation. T-matrix computations (Leinonen, 2014) are performed to simulate radar reflectivity at X-, Ka- and W-band. The T-matrix code simulate the backscattering from spheroids illuminated by a vertical pointing radar beam. The dielectric properties of the spheroid are derived from the retrieved mass-size relations using a Maxwell-Garnett effective medium approximation (ice inclusions in air matrix). The comparison of the computed

X-band reflectivity with the radar measurement are used to show the self-consistency of the microphysical retrieval, Ka and W -band comparison tests the validity of the spheroidal scattering model against multifrequency radar analysis.

5.2.3 Experimental data and results

Three snow events that took place during BAECC campaign on 12, 15-16 and 21-22 of February are used to demonstrate the proposed snowflake mass-dimensional relation retrieval method. All precipitation episodes are synoptic-scale snow events. The equivalent reflectivity factor plane position indicator (PPI) displays of these events, taken from the nearby C-band radar of Ikaalinen, are shown in figure 5.5 and closest radio sounding are shown in figure 5.6. Unfortunately, the 2014 winter season in Finland has been exceptionally mild and dry, therefore, despite the 6 months duration of the BAECC campaign only the presented three snowfall events are available to test the performance of the microphysical retrieval.

The environmental parameters,temperature and relative humidity, are measured with AMF2 The ARM Surface Meteorology Systems at 10 m height above the measurement field in the vicinity of remote sensors (Kyrouac and Holdridge, 2014). Data is stored in 1-minute statistics. The relative humidity is reported with respect to ice below freezing point and correspondingly with respect to water above freezing point. The derived PSD parameters, total particle concentration N_t, median volume diameter $D_{0,PIP}$ and maximum diameter $D_{max,PIP}$, are shown for 5 minute time period in Fig. 5.7, 5.9 and 5.11.

The results of the microphysical retrieval scheme applied to snow cases 12, 15-16 and 21-22 are shown in figure 5.8, 5.10 and 5.12 respectively. The obtained microphysical parameters (mass-dimensional relations and densities) are compared to those given by the 2DVD instrument. The mass-dimensional relations and bulk density from 2DVD measurements and Böhm (1989) method are averaged over 5 minutes time intervals.

The MRRM and the Böhm's method are in general in good agreement among all the analyzed snow cases. The Böhm's method suffers from larger variability due to small total number of particles recorded during the fixed 5 min averaging period. On the other hand the MRRM becomes unstable during low accumulation period. In such cases the longer time averaging period allows to observe a larger number of falling particle, but the validity of the assumption of no change in the snow microphysical properties within the time averaging period is not guaranteed.

The comparison between the different definitions of the bulk densities confirms the theoretical analysis (section 5.1.1) expectations. The snow rate averaged bulk density ρ_{SR} is always larger then the reflectivity averaged bulk density ρ_Z. Figures figure 5.8, 5.10 and 5.12

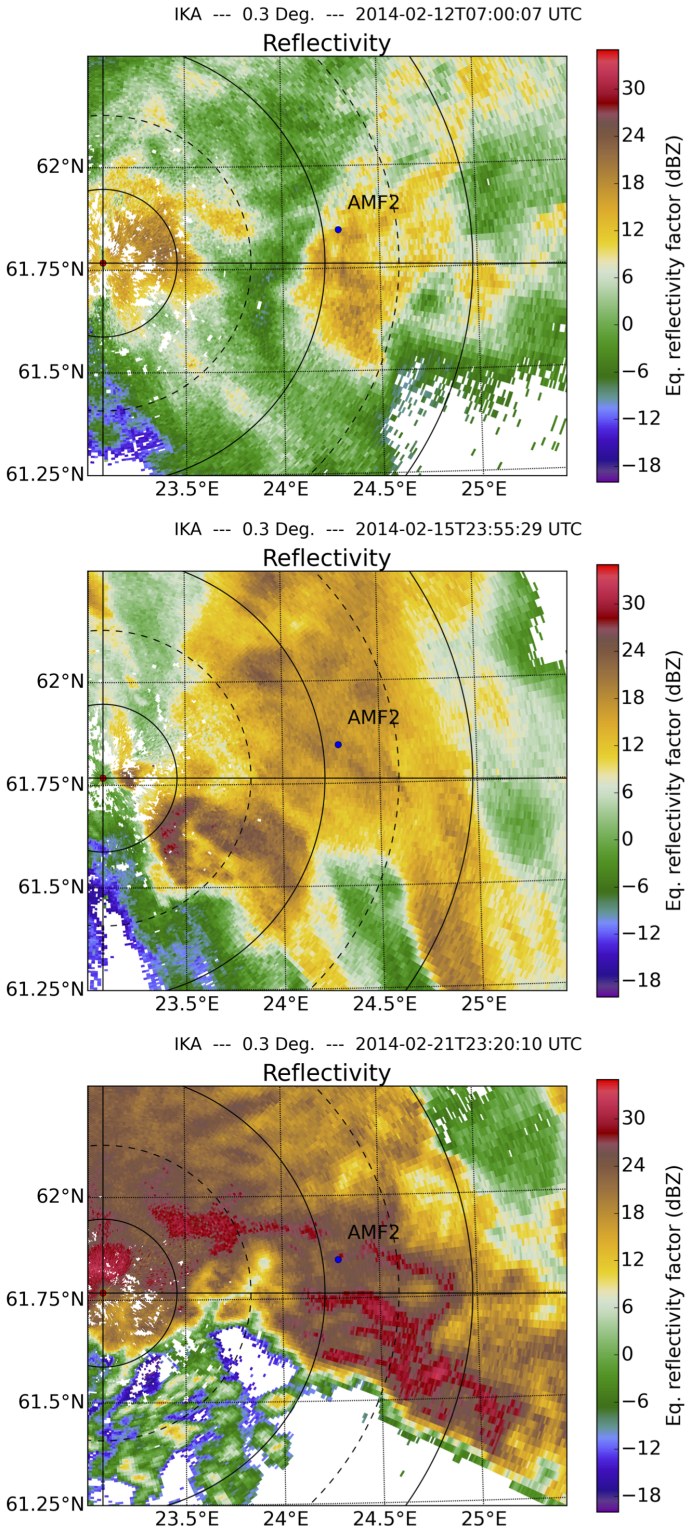

Fig. 5.5 PPI displays of the three snow events of 12, 15-16 and 21-22 February 2014 measured by the Finnish Meteorological Institute Ikaalinen radar. The range rings are plotted every 20 km. The location of the Hyytiälä station, where AMF2 was deployed is shown by a circle.

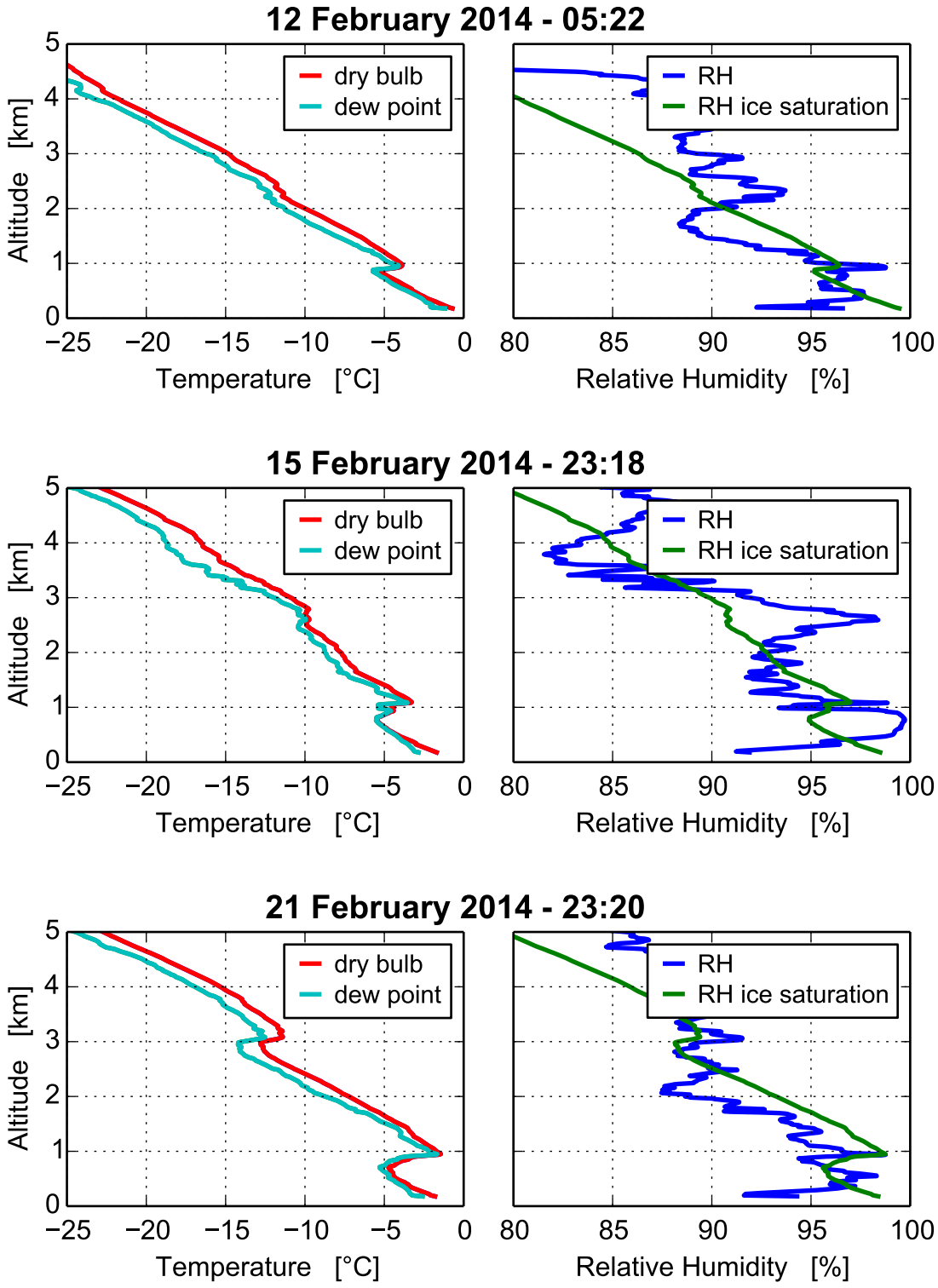

Fig. 5.6 Vertical profiles obtained from the RS closet to the investigated snow events. Left panels show vertical profiles of air temperature and dew point. Right panels show vertical profile of relative humidity; the vertical profile of RH at which the air would be saturated with respect to an ice surface is also drawn.

shows also the volume averaged bulk density given by the 2DVD calculation ρ_{2DVD} which is the largest of the three and is expected to be really close to the value of ρ_{SR}.

When the multifrequency radar estimates are compared, the MRRM gives generally the best results. The MRRM is designed to estimate the mass-size relation that, given the measured fall velocity relation and PSD, reproduces accurately the measured precipitation accumulation and Rayleigh radar reflectivity. Therefore it is not surprising that the MRRM retrieved radar reflectivity at X-band almost perfectly matches the XSACR measurements. The X-band reflectivity time series derived with the Böhm's method microphysical parameters are in general good agreement with the XSACR observation and most of discrepancies can be attributed to the different averaging time periods, but its performance always degrades in case of low accumulations.

At higher frequencies (Ka and W bands) the performance of the two retrieval methods are generally comparable. As it was expected the spheroidal model is not able to reproduce the high frequency scattering properties of frozen hydrometeors (especially at W-band) and the retrieved reflectivities are constantly lower than the measured ones. This fact further confirm the needs of databases of scattering properties of realistically shaped snowflakes.

More specific detail on the results given by the three different snow cases analyzed are given in the following.

Case 12 February 2014

On 12 February 2014, a cyclonic system, with its low pressure center located South of Iceland, causes a southerly flow advecting relatively mild air over Finland. Radio sounding shows a thin supersaturated layer at 1 km and a deeper supersaturated layer above 2 km.

February 12 case is a low intensity event lasting from 05:00 UTC to 09:00 UTC with a total accumulation of 0.8 mm (Fig. 5.7). The temperature raised during the event from -0.7 °C reaching 0 °C around 09:00 UTC.

The first part of the precipitation event was characterized by a really low precipitation intensity (less than 0.1 mm/h) with $N_t \approx 1000$ m^{-3} and $D_0 \approx 1$ mm. The retrieved mean β value of 2.5 and the low bulk density of ≈ 150 kg/m^3 indicates that the precipitation was mainly composed of small particles, such as irregular crystals and small aggregates as confirmed by the PIP images.

Most of precipitation occurred between 07:30 and 07:45. Unfortunately during this period the XSACR was not operational due to a technical failure and the MRRM cannot be applied. During this period the temperature increased and got close to 0 °C. These conditions were favorable for the ice aggregation and in fact β values as low as 1.8 were calculated. The PIP instrument reveled also the presence of large aggregates (with sizes up to 1 cm).

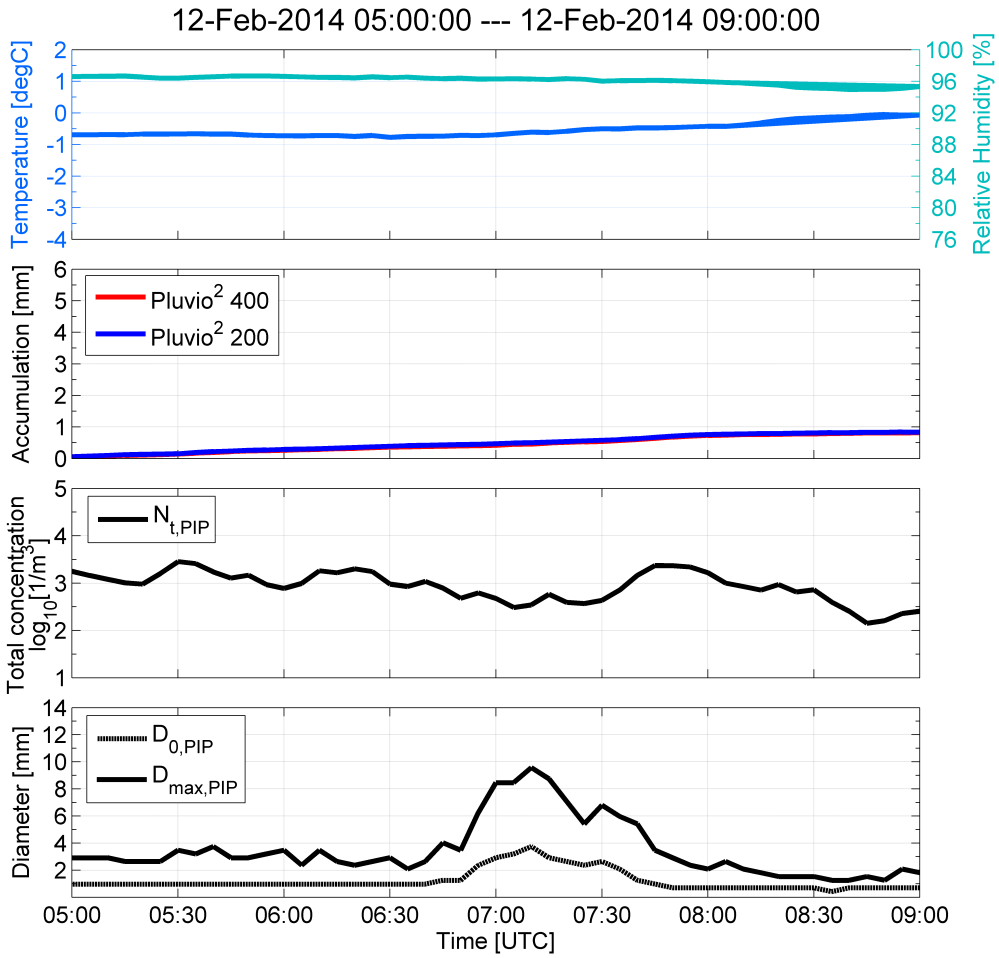

Fig. 5.7 Temperature and relative humidity,liquid equivalent snow accumulation measured with both Pluvio^2 gauges and the PSD parameters, total particle concentration N_t, median volume diameter D_0 and the maximum diameter D_{max} during the event on 12 February 2014 in Hyytiälä.

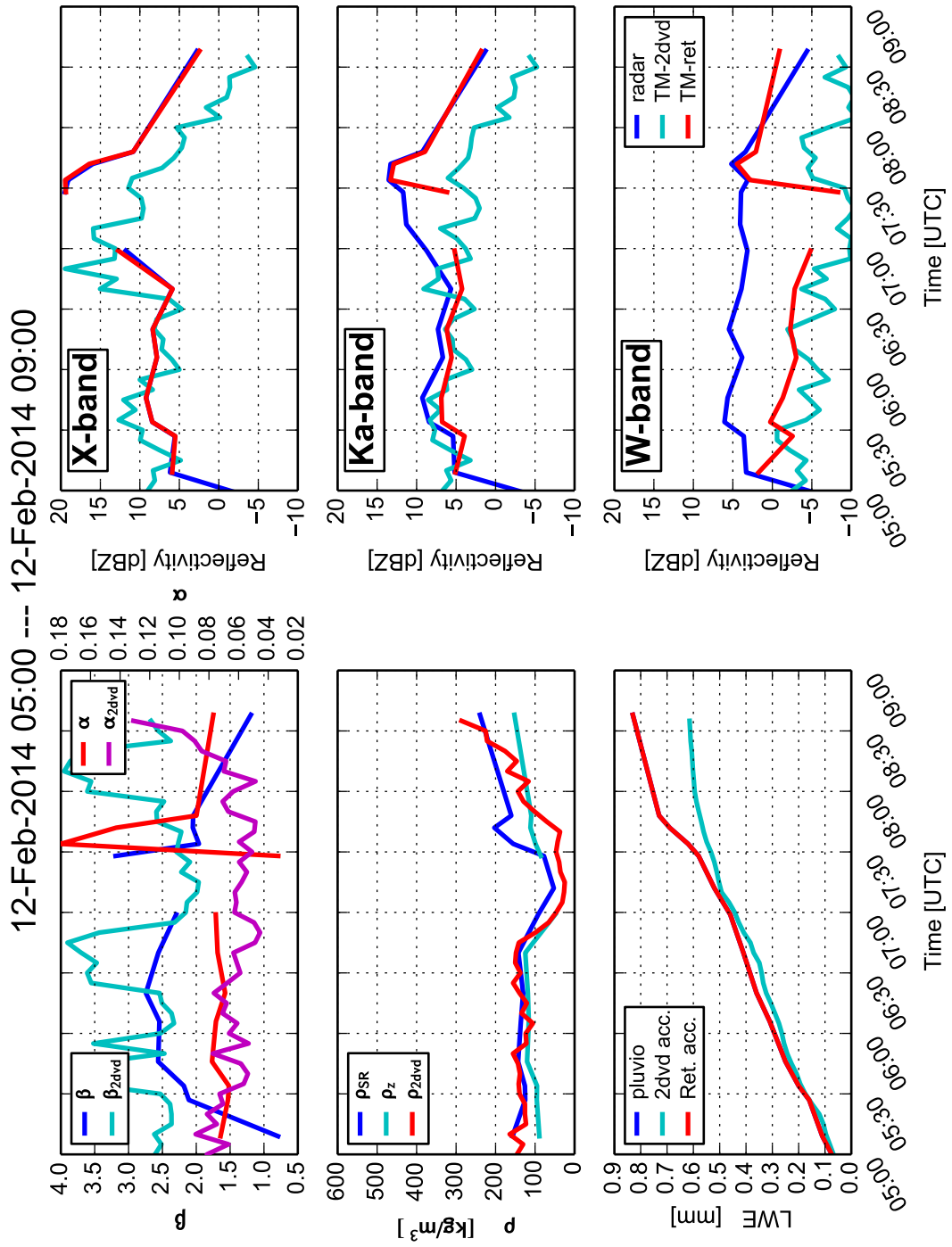

Fig. 5.8 Summary of the retrieval results for the test case of 12 February 2014.

Case 15-16 February 2014

The synoptic scale weather conditions during the night of 15 to 16 February 2014 over Hyytiälä were influenced by a weakening low pressure system with its center located over Scotland which moved further in northeasterly direction towards Norway. A well-developed warm type occlusion associated with the cyclone moved across Finland from SW to NE. A low-level mixed-phase cloud could be identified in the radar PPI. Upper ice clouds appeared in the radar images at 12:00 UTC of 15 February. These clouds deepen and lowered with time until at 21:00 UTC the frozen particles felt into the mixed-phase cloud causing precipitation of rimed snowflakes.

On February 15 snow started falling at 21:30 UTC and continued until 01:30 UTC on February 16 (Fig. 5.9). The study focuses on the time period from 22:30 UTC to 01:00 UTC. During this interval, gauges recorded 2.2 mm of LWE accumulation. Temperature varied between -1.8 and -1.3 °C. The 2DVD instrument was operational just after 00:00 of 16 February. Around the 23:45 and 23:55 of 15 February also the PIP instrument experienced a technical failure that produced two spurious peaks in the calculated bulk densities.

From 23:00 to 23:30 of 15 February the mean snow rate was 0.5 mm/h. D_0, D_{max} and N_{tot} reached quite large values of 2 mm, 7 mm and 1000 m^{-3} respectively. The MRRM method has computed a mean β value of 2 that predicts the presence of unrimed assemblages of ice crystals as confirmed by the PIP images.

The observed snowfall rates at the surface reached their maximum values of 1.6 mm/h from 00:30 and 01:00 UTC, February 16. In this period of time, D_0 and D_{max} also reached their maximum values of 3.4 mm, 12 mm. The particle number concentration N_{tot} was constantly around 10000 m^{-3}. The measured bulk densities reached their minimum value of 80 kg m^{-3} when the other parameters reached their peaks. This fact should be an indication of really fluffy (i.e. low density) particles like aggregates of needles.

The Böhm's method indicates a rather constant β value of 2.5 for this period whereas the MRRM algorithm gives β values oscillating between extreme values of 3.0 and 2.0. Visual analysis of the PIP images revealed the presence of three major particle populations: Single needles (1-2 mm), small (1.5-2 mm) nearly spherical aggregates, and larger (2 mm) needle aggregates. This mixture of rimed particles, needles, and needle aggregates could be related to ice multiplication mechanisms like the rime splintering (Hallett-Mossop) process (Hallett, 1974; Mossop, 1976).

For this interval, the MRRM assumption of non-mixing particle population during the averaging time period breaks. This explain the large variability of MRRM results. However the method correctly reproduces the measured precipitation accumulation and X-band radar reflectivity.

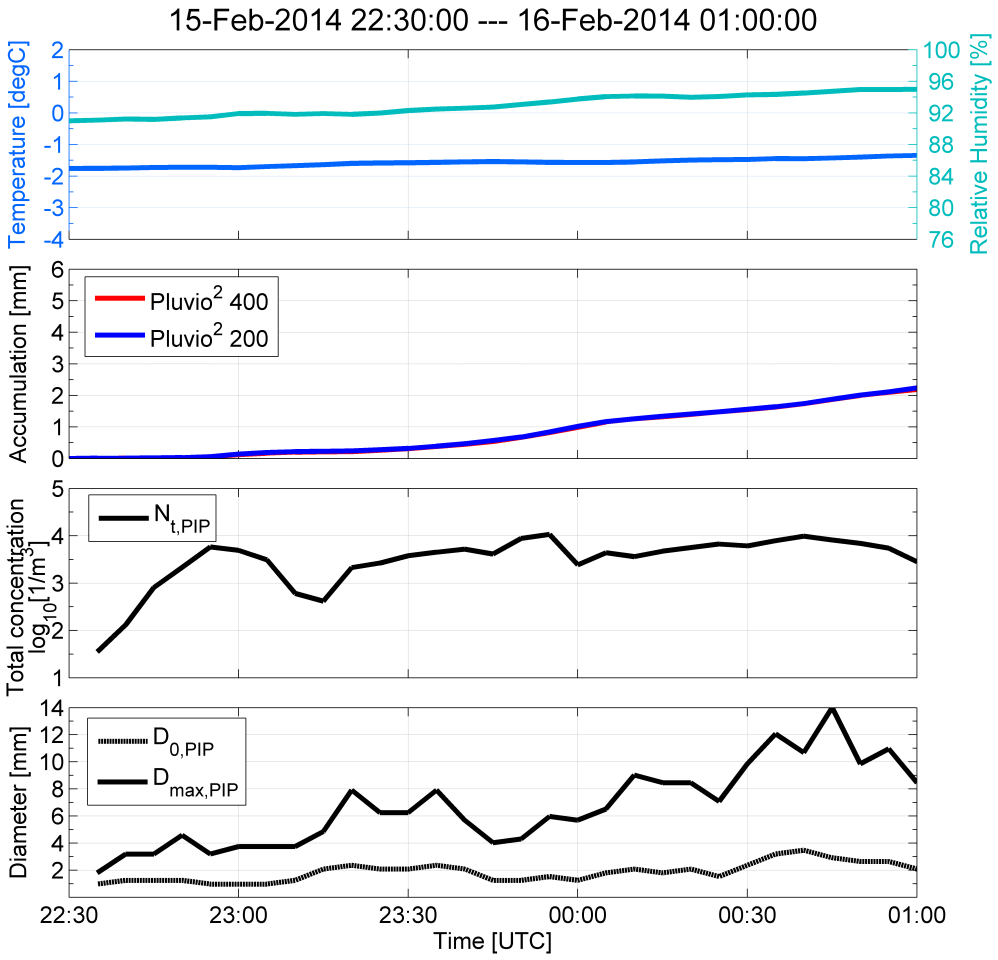

Fig. 5.9 Same as Fig. 5.7 for the event on 15-16 February 2014.

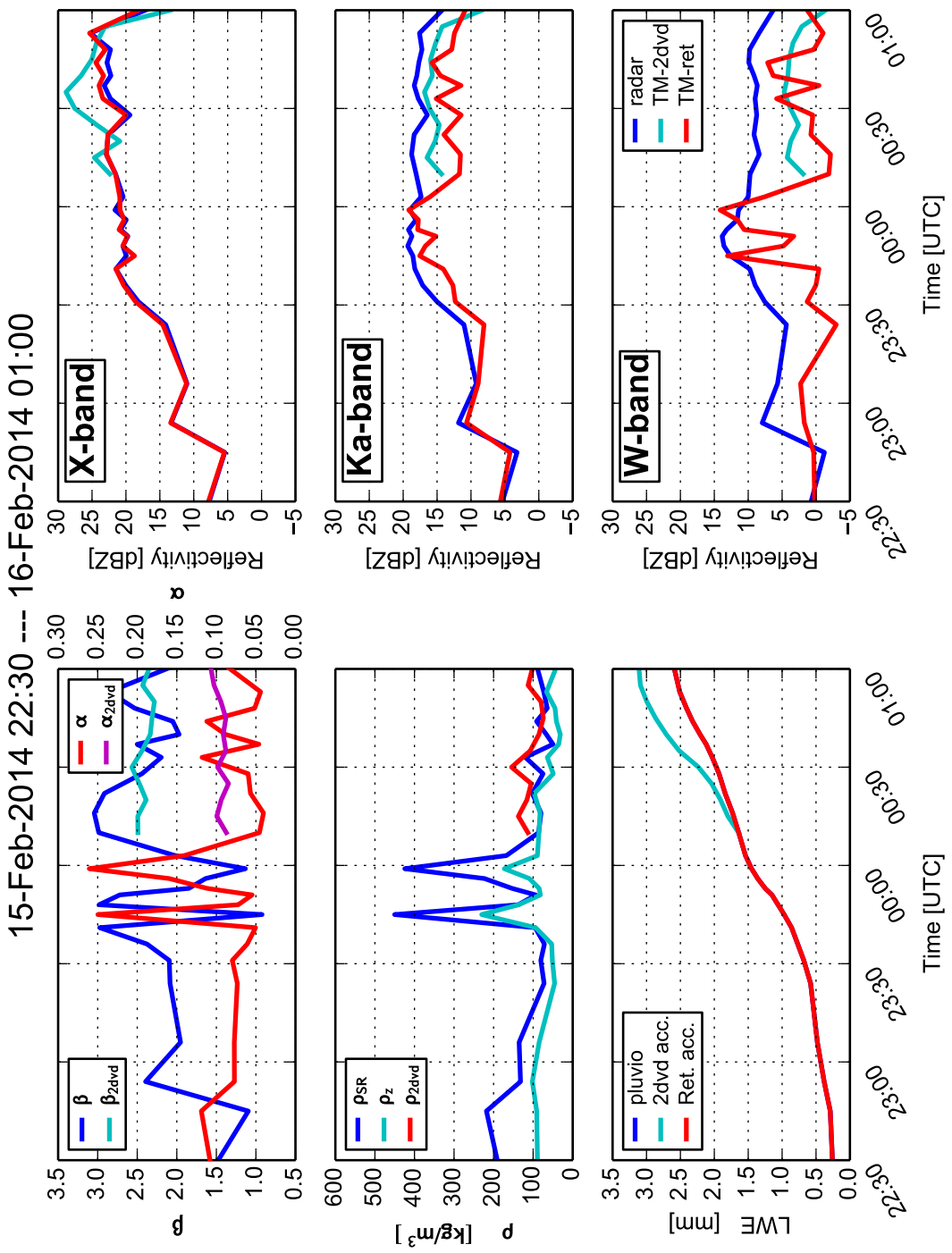

Fig. 5.10 Same as Fig. 5.8, but for test case 15-16 February 2014

Case 21-22 February 2014

The weather situation on 21 February is characterized by a cyclone located over Norwegian sea and a warm-type occlusion moving in northeasterly direction over the field station. Similar to the 15-16 February event, a thin mixed-phase cloud can be identified at low-level and lasted almost continuously during the snowfall event. At 5:00 UTC, thicker ice clouds can be seen in the radar images, slowly descending and deepening before they merge with the low mixed-phase layer at 16:00 UTC. The precipitation event is heavily characterized by this embedded cloud system. The RS show two temperature inversions coupled with local peaks of RH at 600 m and 3 km which are associated with mixed-phase cloud layers.

February 21 snow case is a moderate to heavy snow event that lasted fourteen hours from 16:00 UTC on February 21 through 07:00 UTC on February 22 and resulted altogether in LWE accumulation of 8 mm. The results of the present study are shown for the time period between 19:00 UTC and 06:00 UTC, with LWE accumulation of 6.7 mm (Fig. 5.11). The temperatures close to surface during the 21 February part of the event were close to -2 °C. After midnight the temperature raised continuously reaching 0 °C at 5:00 UTC.

An intense snow event, has been measured from 22:50 of 21 February to 00:00 of 22 February. During the first part of this case (before 23:00 UTC), the snowfall rate is relatively low (below 0.5 mm/h) and composed by a low concentration (less than 1000 m^{-3}) of small-sized (D_{max} < 3 mm) particles with high bulk density (up to 600 kg/m^3). The PIP images, in fact, indicates the presence of almost spherical rimed particles. A further confirmation of strong riming is given by the microphysical properties retrieval algorithms that indicate values of β ranging from 2.5 to 2.8.

The peak of snowfall rate (2.2 mm/h), registered between 23:10 and 23:40 is the largest value observed for all three cases included in this study. Such maximum was accompanied by a strong broadening of the PSD. D_0 reached up to 4.7 mm and D_{max} was as large as 12 mm. The particle number concentration also increases up to 10000 m^{-3} and at the same time, the calculated bulk density decreased to 100 kg/m^3. According to the MRRM and the Böhm's method, β values ranged from 2.3 to 2.5, indicating the presence of really large and moderately rimed aggregates. This expectation was further confirmed by the PIP images.

After 03:30 UTC on February 22, temperature turned positive, but because of the subsaturated conditions (relative humidity 97%) melting started just at 04:30 UTC (Matsuo and Sasyo, 1981). During this period, the precipitation is characterized by snow particles with characteristics similar to those observed during the 23:00 - 23:40 interval of February 21.

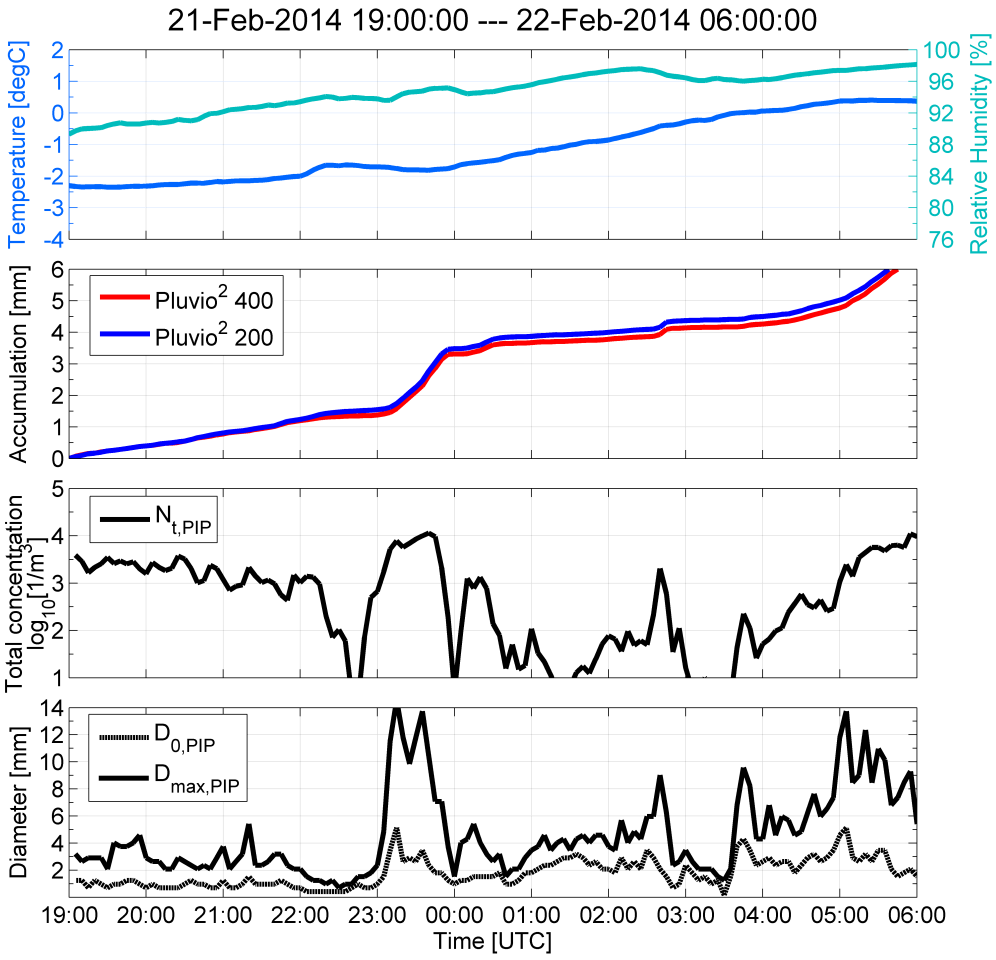

Fig. 5.11 Same as Fig. 5.7 for the event on 21-22 February 2014.

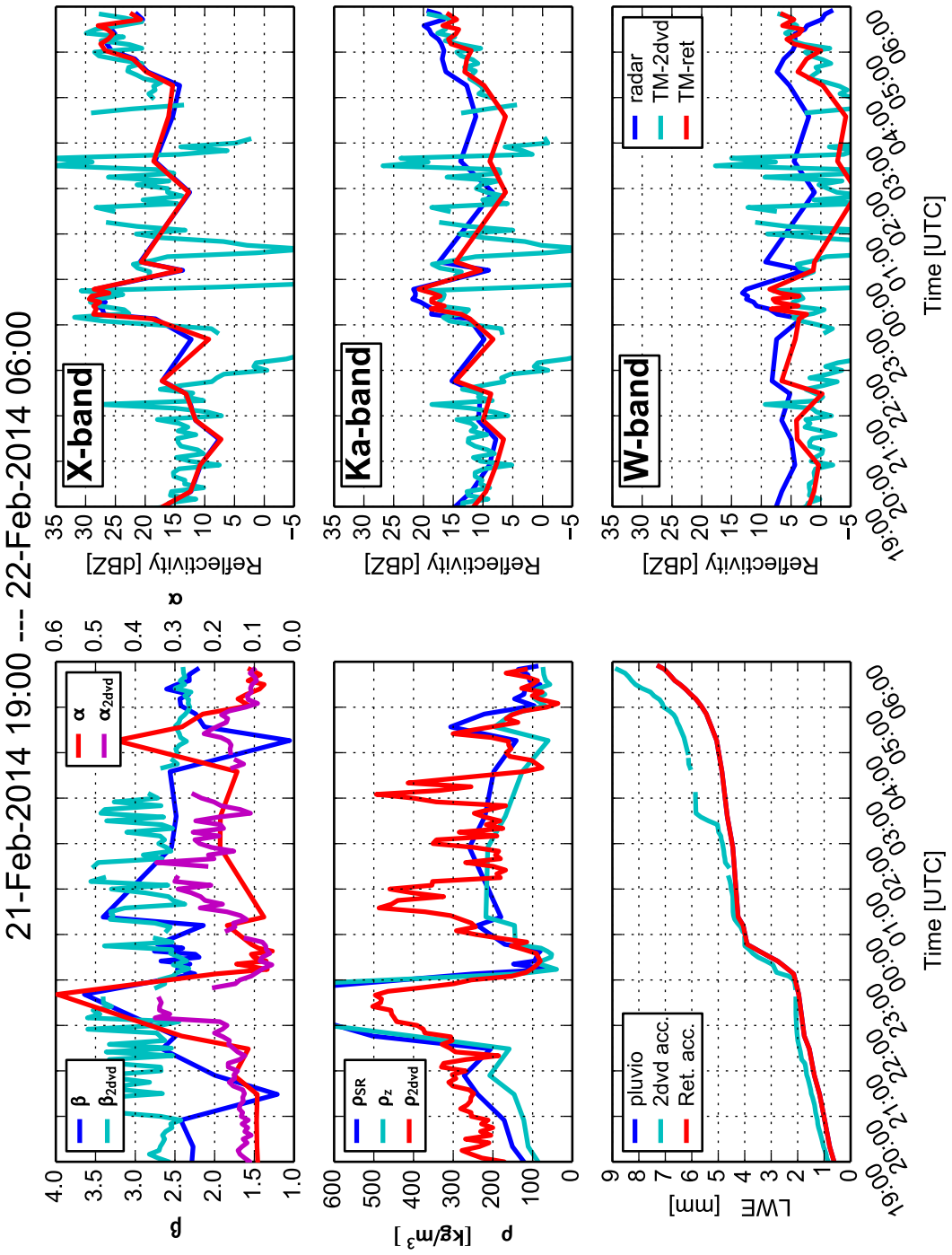

Fig. 5.12 Same as Fig. 5.8, but for test case 21-22 February 2014

Chapter 6

Applications of radar studies

Many times the achievements of a scientific study requires much time and much more work to produce practical results. It is opinion of the author that the time delay from the scientific results to the operational utilization of such knowledge is one of the most prominent cause of the modern disaffection of the public opinion respect to the scientific research. Moreover, even the most theoretical scholar should find useful to face off real-world problems, otherwise his/her research objectives are likely explore scientific fields that will never give practical outcomes.

This chapter is intended to highlight the practical applications of microphysical and scattering studies of snow. It is hope of the author that this resume would facilitate the utilization of the present study for bleeding edge education and outreach purposes.

The first section (6.1) of this chapter illustrates the application of complex snowflake modeling, DDA calculations and microphysical retrieval to reproduce the high-frequency (Ka and W-band) radar measurements. The results of this study confirm the greater capabilities of complex aggregates modeling in simulating the scattering properties of snow. The results are closely associated with the possibility to estimate the snowflake mass-size relation and further confirm the reliability of the microphysical retrieval method presented in chapter 5.

The second part (section 6.2) illustrates the work performed in collaboration with the Emilia Romagna region environmental agency (ARPA-ER) to implement an Hydrometeor Classification Algorithm (HCA) based on polarimetric radar measurements. The HCA implementation is planned to become an operational product of the ARPA-ER regional weather service and is currently in a test phase. The HCA will provide ARPA with a state of the art tool able to discriminate between different types of radar echoes and improve the performance of the operational quantitative precipitation estimation.

6.1 Multifrequency radar snow retrievals

Chapters 4 and 5 left an open question. It is possible to use DDA scattering computations to reproduce high frequency radar measurements?

Chapter 4 concluded that the fine structure of snowflake aggregates have an important role in determining the snowflake scattering properties. When the snow particle size parameter is larger than 1, the soft-sphere model is not able to reproduce the snowflake backscattering signature. When accurate modeled snow scattering properties are integrated over a set of PSDs large uncertainties arises from the unknown microphysical characteristics of snow and in particular the mass dimensional relation.

In chapter 5, an automatic microphysical retrieval method has been developed and tested on three different snow events. The microphysical retrieval method has been able to retrieve snow mass-size relations that accurately reproduce snow accumulations and near-Rayleigh radar reflectivity when integrated over the ground measured PSDs, but again, the Ka and W-band reflectivities calculated with a soft-spheroidal model and T-Matrix method largely underestimates the actual measurements.

Aiming at reproducing the high frequency scattering properties of snowfall using the microphysical information of PSDs and mass-size relation a large database of snowflake scattering properties spanning among a large variety of mass-dimensional relation is needed. Leinonen and Szyrmer (2015) published a scattering database of aggregates of dendritic crystals with various degree of riming. The riming degree modifies the mass of the aggregate particle and allows to determine the scattering properties of snowflakes with various mass-size relationships.

The scattering database uses the maximum dimension to define the snowflake's size. The D_{max} has been converted to the equivalent volume diameter using the aspect ratio information included in the database.

For each time interval analyzed with the microphysical retrieval method the scattering properties, extracted from the DDA database, are integrated over the measured PSD, which is defined at discrete size intervals of dD = 0.25 mm. For each size interval D_i the particles in the database with a dimension D_p that satisfy the relation $D_i - dD/2 < D_p < D_i + dD/2$ are selected. From this subset the particles are further selected according to their mass, which is requested to match the retrieved mass-size relation with a 10% tolerance. If no particle in the database satisfy these conditions the tolerance on the particle mass is relaxed to 20%. The radar backscattering properties of the specific size is defined by the average of the selected particles' σ_{hh}. This process is repeated through the whole size distribution to obtain the simulated radar reflectivity.

The comparison of the DDA retrieved radar reflectivities with the measured data is shown in figures 6.1, 6.2 and 6.3. The radar reflectivities obtained from the mass size relations and the T-matrix method is also shown as reference. Statistics about the average bias and the root mean square error (RMSE) between the measured radar reflectivity and the estimated Z_e using DDA and TMM are summarized in table 6.1 for each frequency and snowfall event.

As expected, the X-band DDA-retrieved radar reflectivity almost perfectly matches the observations at any analyzed snow event. In fact, at X-band radar frequencies the snow particles can be still considered as Rayleigh scatterers and no significant discrepancy is expected between DDA and TMM scattering properties.

At higher frequencies when the TMM reflectivity simulation results match the radar observations, the usage of the DDA scattering properties provides no significant contribution to the high frequency radar simulation. An example of such cases is the Ka-band reflectivity time series of the 12 February snow event. For this case ice crystals and tiny aggregates has been observed and the Rayleigh scattering approximation could be applied also at Ka-band. In this case, most of simulation bias could be attributed to the uncertainties related to the PSD measurement in low accumulation conditions.

For most of other cases the Ka-band DDA calculations gives reflectivity time series that almost perfectly match the measurements whereas the T-matrix soft-spheroid model always underestimate the Ka-band reflectivity. With respect to the TMM simulation the DDA scattering model at Ka-band improves the average bias from 2.9 to to 0.9 dBZ for the 15-16 February event and from 8.8 to -0.7 for the 21-22 February event; whereas the RMSE is reduced from 13.3 to 2.9 dBZ and from 8.8 to 5.3 dBZ respectively.

The previous conclusion is not valid during the two intense snowfall period of 21-22 February case (from 23:00 to 00:00 of 21 February and from 04:30 to 06:00 of 22 February). During these two cases the DDA reflectivity simulations overestimates the radar observation up to 2 dBZ at Ka-band and also up to 10 dBZ at W-band. In these part of the snowfall event, multiple types of snowflakes have been recorded by the PIP instrument, therefore it is probable that the microphysical retrieval method has failed.

From 04:30 to 06:00 of 22 February T-matrix soft-spheroidal model performs better than the DDA algorithm at W-band. It is unclear whether this is due to a bad microphysical retrieval or an intrinsic bad performance of the DDA algorithm. The solution to this problem needs more investigation. It has been already discussed that during this snow event the MRRM is expected to fail. Another possible explanation of the better performances of the T-matrix simulation could be given by looking at the measured dual frequency ratios (DFR). It appears that $\mathrm{DFR}_{X,K}$ is smaller than 7 dB and $\mathrm{DFR}_{K,W}$ is larger than 12 dBZ. Leinonen and Moisseev (2015) found that only spheroidal models can reproduce the measured reflectivities

Table 6.1 Average bias and root mean square error (RMSE) of reflectivity simulation using DDA and T-matrix methods (TMM) for the observed snowfall events

		average bias [dBZ]		RMSE [dBZ]	
Event date	band	DDA	TMM	DDA	TMM
12 February 2014	X	0.7	-0.1	1.1	0.1
	Ka	1.1	1.4	4.5	4.5
	W	-0.3	4.7	8.4	38.8
15-16 February 2014	X	0.3	-0.3	2.6	0.4
	Ka	0.9	2.9	2.9	13.3
	W	2.1	5.6	3.8	48.3
21-22 February 2014	X	-0.4	-0.4	2.2	0.7
	Ka	-0.7	8.8	5.3	8.8
	W	-4.0	4.4	25.3	25.1

in this area of the $DFR_{X,K}$ - $DFR_{K,W}$ space while aggregate snowflake models cannot. The bad performance of the DDA reflectivity retrieval for this particular case is likely to be caused by the inadequacy of the aggregate snowflake model.

The DDA W-band reflectivity simulations underestimate the MWACR observations for the first part of the 12 February case (before 07:00). It is possible that in this case a large portion of the PSD was not observed by the PIP instrument due to the technical limitation on the smallest detectable size. Therefore the retrieved radar reflectivity could be biased due to the underestimation of the total particle number concentration. During the second part of the case (after 07:30) larger aggregates are found by the PIP instrument and the W-band DDA simulation overestimates the measurement up to 5 dBZ. The technical failure of the XSACR instrument has certainly cause large issues to the microphysical retrieval and thus, it is not sure what is actually causing the observed discrepancies.

With the exception of the previously discussed cases, the DDA model matches well the W band measurements, whereas the T-matrix simulation underestimates the W-band reflectivities up to 10 dBZ and 5 dBZ on average.

Despite the limitations identified in these simulations, there are many instances where the DDA calculations, combined with the MRRM mass-size relation match the triple frequency radar measurements. These results support the validity of both the microphysical retrieval method and the complex aggregate modeling of snowflakes for scattering computation.

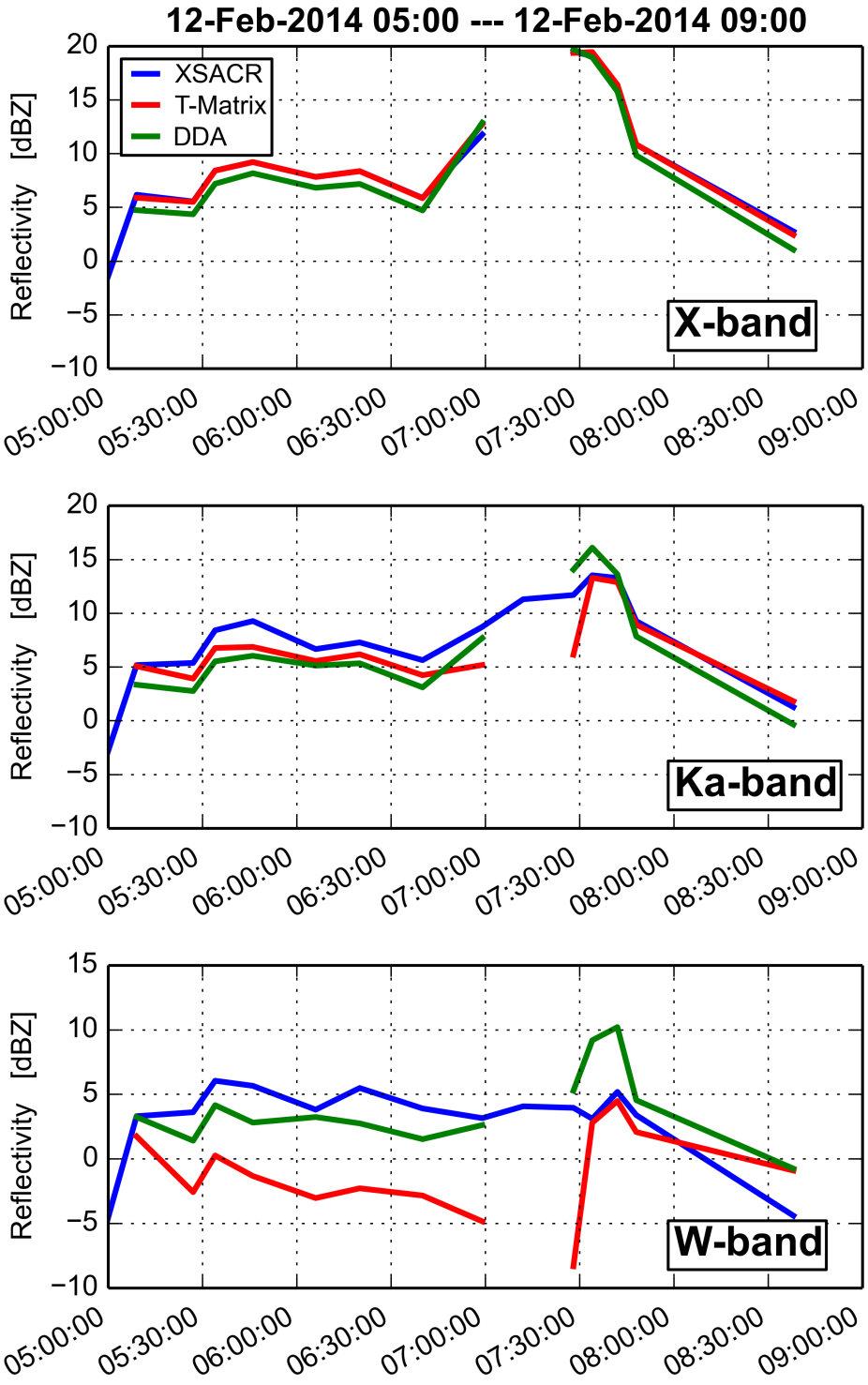

Fig. 6.1 Simulation of the radar equivalent reflectivity factor using the retrieved microphysical parameter in conjunction with T-matrix (red line) and DDA scattering calculations (red line). The measured radar reflectivity at the different frequencies is drawn with a blue line.

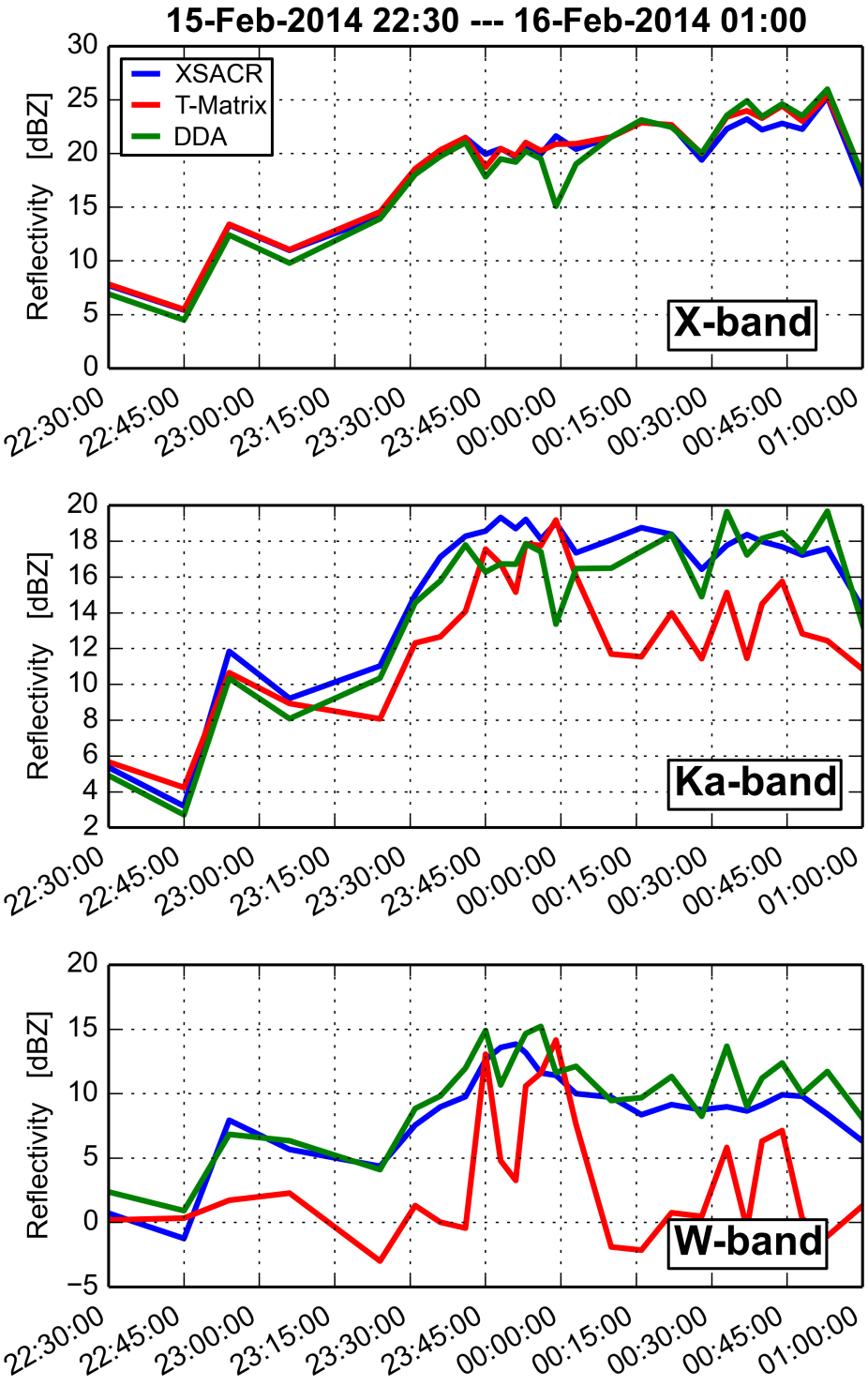

Fig. 6.2 Same as figure 6.1 for the event on 15-16 February 2014

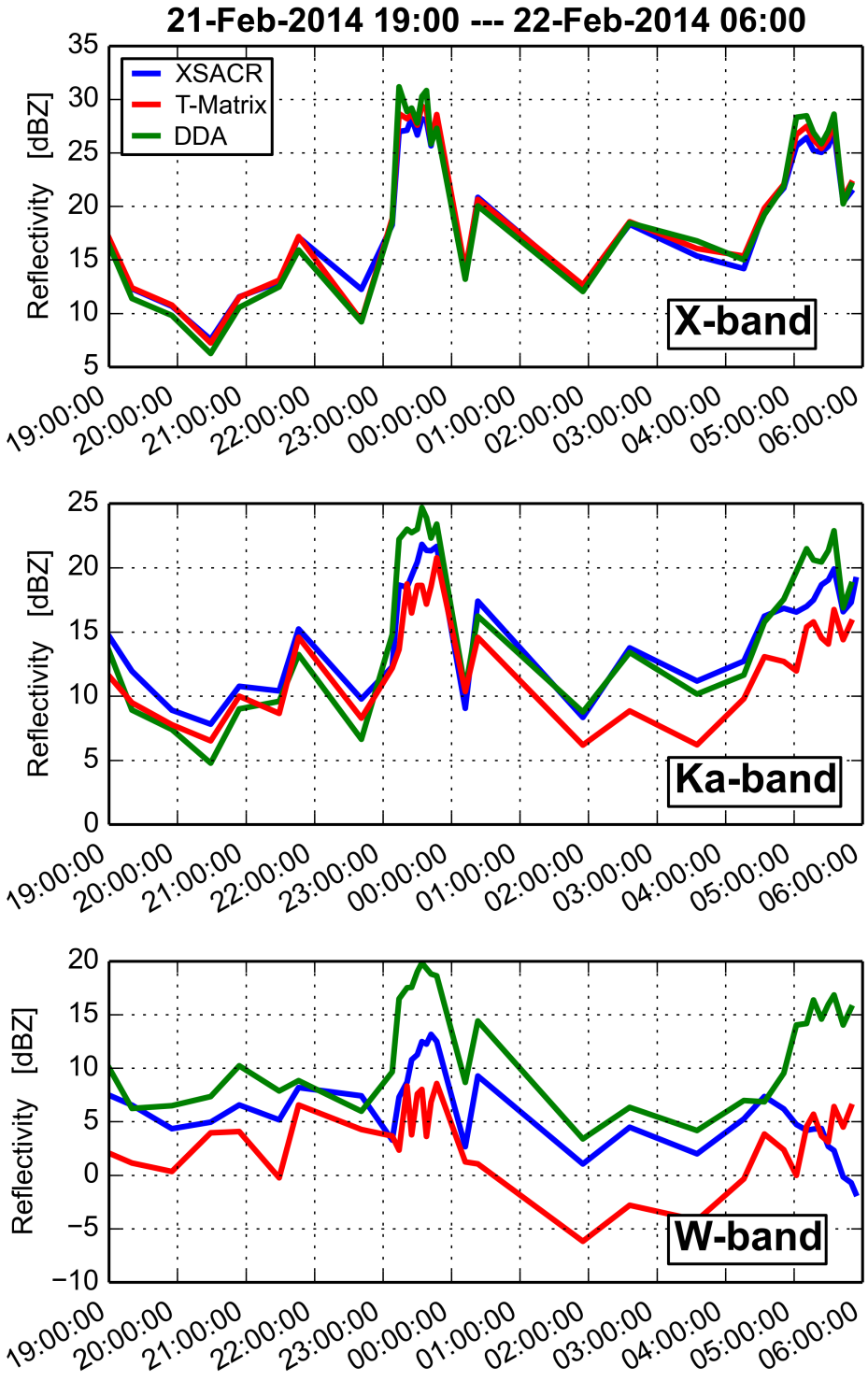

Fig. 6.3 Same as figure 6.1 for the event on 21-22 February 2014

6.2 Hydrometeor classification algorithm

The main objective of radar Hydrometeor Classification Algorithms (HCA) is to retrieve qualitative information about the dominant hydrometeor type within a given sampling radar volume. The radar echo classification is important for many reasons. The relationship between radar measurements and precipitation quantity depends on the precipitation type and thus HCA is used for quantitative precipitation estimation (QPE) preconditioning. Weather radar are mostly intended to observe clouds and precipitation, but often the radar signal is affected by unwanted echoes such as ground clutter, birds and insects; HCA helps to clean radar images from spurious non-meteorological signals. Finally, the identification and localization of dangerous weather events such as thunderstorms, hail or heavy rain and snowfall is an important part of the early alert system of civil defense organizations.

It is important to note that the actual hydrometeor content of a radar volume is usually a mixture of many types. Most HCA uses advanced clustering and pattern recognition techniques to individuate the dominant hydrometeor type within the radar volume. Starting from a selected number of hydrometeor types the method label the observed set of measurements according to its degree of similarity respect to a certain predefined theoretical and statistical group of features that identifies the hydrometeor type. The calculation of the degree of similarity is conducted by means of different statistical techniques such as: fuzzy logic classification, Bayesian best estimators, neural network, support vector machines and other machine learning algorithms.

The performance of the different HCA methods depend on the available measurement infrastructure. HCAs are optimized to work with a certain set of atmospheric data, including possibly also non-radar observations such as radio sounding, ground measurements and numerical weather forecasts. Since the scattering properties of hydrometeors depend on the wavelength of the incident radiation, different HCA methods are used at different radar frequencies. The most recent HCA techniques make large use of the modern radar capabilities to distinguish the the various hydrometeor types respect to the polarimetric information content about their overall shape.

Considering the measurement capabilities of the two polarimetric weather radar operated by ARPA-ER, the fuzzy logic polarimetric HCA proposed by Park et al. (2009) has been implemented. The implementation of the HCA algorithm constitutes a first step in the seeking for an advanced quantitative precipitation estimation (QPE) of frozen hydrometeors based on the microphysical and scattering analysis carried through out the present thesis. The lacking of local statistics about snow PSDs, characteristics and radar signatures inhibited further developments of the HCA algorithm. However the implementation of the algorithm constitutes an essential requirement for the prosecution of the research in this field.

The classification is conducted on the spatial scale of the radar resolution volume (radar range gate or radar volume bin), and its inputs are a set of polarimetric variables, namely the horizontal copolar radar reflectivity Z_{hh}, the differential radar reflectivity Z_{dr}, the specific differential phase K_{dp}, the correlation coefficient between the orthogonal polarized return signals ρ_{HV}. The algorithm makes also use of an horizontal texture parameter of the reflectivity SD(Z) and differential phase SD(Φ_{dp}) fields. This texture parameter is computed as the standard deviation over an along-beam boxcar of 1km width in the case of Z and 2 km for the Φ_{dp} field. These texture parameters quantifies the magnitude of small scale fluctuation in the polarimetric radar variables and thus helps to individuate non-meteorological scatterers. The mean Doppler velocity is utilized to reduced the uncertainties in the individuation of GC which does not produce a Doppler shift.

Before applying the algorithm, general data correction procedures are applied.
Z, Z_{dr}, and ρ_{hv} are smoothed along each radial using a 1-km averaging running window for Z and a 2-km window for Z_{dr} and ρ_{hv}. The Z and Zdr fields are corrected for path integrated attenuation by adding the bias estimated using the Φ_{DP} field (Bringi et al., 2001). The K_{DP} is derived from the filtered and unfolded Φ_{dp} field using the algorithm by Vulpiani et al. (2012).

The HCA discriminates between 10 classes of radar echo which are reported in table 6.2

Class	Name	notes
GC	Ground clutter	including ground clutter due to anomalous propagation
BS	Biological scatterers	birds, insects and bats
DS	Dry snow	mostly aggregates, not single crystals
WS	Wet snow	
CR	Ice crystals	
GR	Graupel	
BD	Big drops	DSD skewed toward large drops (> 3 mm)
RA	Rain	light to moderate
HR	Heavy rain	
RH	Rain and hail	

Table 6.2 Defined Hydrometeor classes

6.2.1 Fuzzy logic classification of hydrometeors

The truth values of variables in the fuzzy logic may be any real number between 0 (boolean logical false) and 1 (boolean logical true). The fuzzy logic based classification scheme consider the available measurement as "hints" on the nature of the unknown state of the observable and calculates a truth value for each possible class using the available observations. The unknown is identified to belong to the class with the largest truth value.

The information content of each observation depends on previous assumptions. For each radar echo class, a typical range of values for the radar measurements is defined. This range of values could either come from microphysical and scattering models or statistical analysis of previous observations. Each range of values takes the form of trapezoidal *membership* (weighting) functions $P_i(V_j)$ (which characterizes the distribution of the j-th variable for the i-th class) with a maximum value of 1 and a minimum value of 0. The six sets of membership values (one for each observable) are combined in a process called *aggregation* that produces a set of aggregation values A_i. The present implementation uses a weighted sum as aggregation process

$$A_i = \frac{W_{ij} Q_j}{\sum_{j=1}^{6} W_{ij} Q_j} \tag{6.1}$$

In equation 6.1 W_{ij} is a weighting parameter which determines the capacity of the observation j-th to identify the i-th class. For example the peculiar polarimetric characteristics of GC are the low ρ_{hv} and large texture values SD, whereas the measured Z could be any value and thus have a negligible influence in the determination of the GC aggregation value. The value of the weighting parameter largely depends on the degree of overlapping of the membership functions for that particular measurement. If the membership function of a specific class i is well separated from the other classes for a certain measurement j the value W_{ij} will be close to 1.

The accuracy of the radar measurements largely affects the HCA performance. The confidence vector Q_j in equation 6.1 takes into account the possible sources of measurement error and weights the relative importance of each observation accordingly. The confidence vector takes into account the vulnerability of radar observations to calibration errors, attenuation, nonuniform beam filling (NBF), partial beam blockage (PBB) and receiver noise.

The top and bottom of the melting layer can be determined from an upper-air sounding, numerical model output, or from polarimetric data. The melting layer detection algorithm (MLDA) utilized in the implementation, determines the top and bottom of the melting layer as a function of the azimuth for any given radar scan (Giangrande et al., 2008). The MLDA identifies radar ranges where polarimetric variables reaches determined thresholds that are found to be associated with the boundaries of the melting layer.

Figure 6.4 shows the normalized membership function for some classes considering just two distinctive measurements: Z-Z_{dr} and Z-ρ_{hv}. As it can be see, rain and dry snow classes largely overlaps in these space. The overlapping of liquid and frozen hydrometeors membership functions is a well known problem of hydrometeor radar classification. The identification of these radar classes can be achieved by taking into account the location of the radar volume respect to the height of the melting layer. The melting layer height and depth can be determined by radio sounding or numerical weather prediction, but since we wanted to made a self-sufficient radar HCA a polarimetric melting layer detection algorithm has been implemented.

Melting layer detection

The melting layer detection algorithm implemented (Giangrande et al., 2008) makes use of the spatial distribution of the characteristic polarimetric signature of wet snow to detected the azimuthal distribution of melting layer height.

In fact, melting hydrometeors produce a distinctive signature in radar reflectivity measurement, known as the radar "bright band", due to the higher refractive index of water respect to ice at microwave frequencies. For the same reason the high reflectivity band is associated with large values of the differential reflectivity. The last peculiar characteristic of the melting of snowflakes is the drop in the correlation coefficient which arises because of the mixture of water and ice phase and the largely inhomogeneous distribution of water within the melting snowflakes.

It is worth noting that the Z_{dr} peak and the ρ_{hv} drop reach their own maximum at beginning of snow melting (near the isotherm 0° C level) because of the maximum inhomogeneity of the water distribution inside each particle. The radar reflectivity tends to increase in the initial phase of the melting because of the increasing fraction of water within the wet snowflakes, and decline in the later stages because of the reduction of the hydrometeor size. This different distribution of polarimetric signatures of snow melting enables to determine not only the melting layer height, but also its top and bottom level.

6.2.2 Class designation

The HCA defines the radar echo class according with the "largest aggregation value" criteria. Some exception to this criteria are applied in order to ensure the consistency of the classification product with respect to the location of the melting layer and some peculiar characteristics of certain hydrometeor classes.

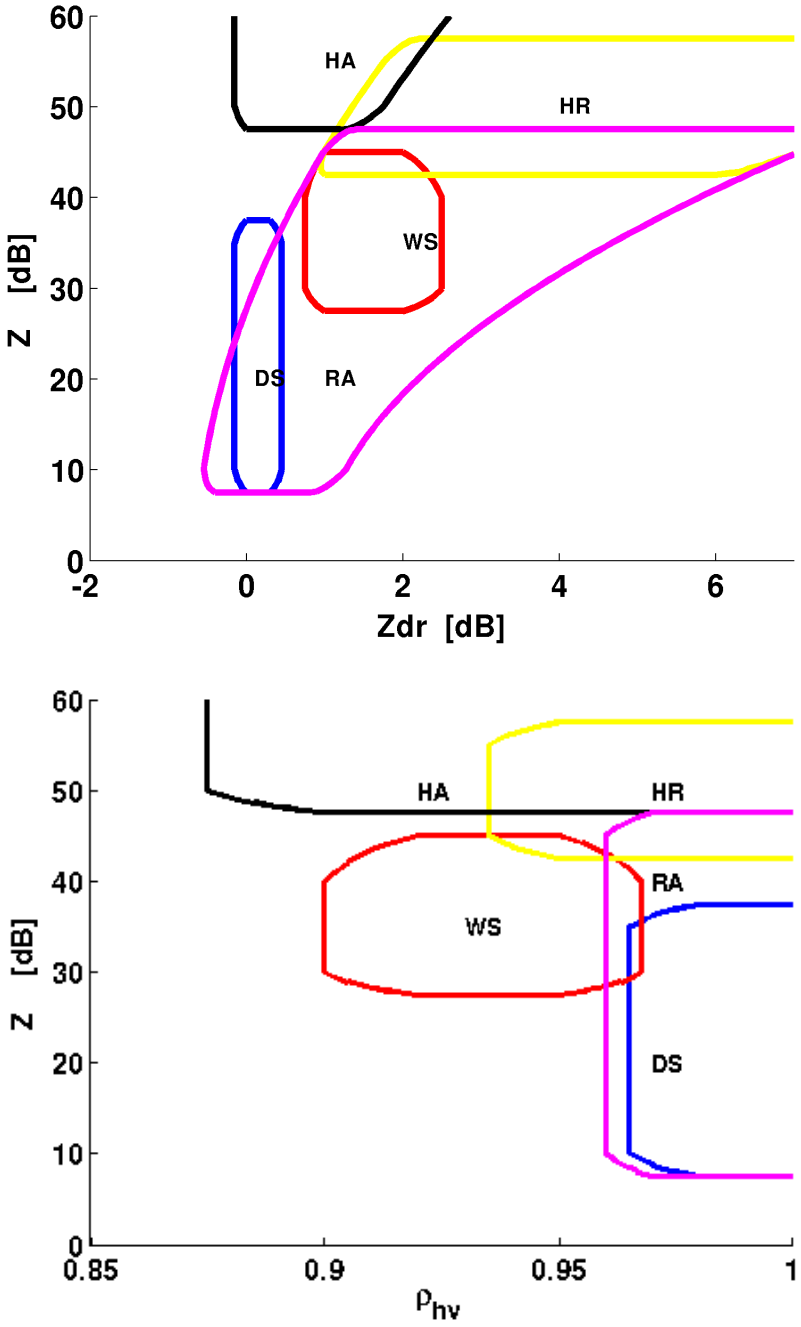

Fig. 6.4 Boundaries of the class membership function in the Z-Z_{dr} (top panel) and the Z-ρ_{hv} space (bottom panel). The class boundaries are drawn at a value of the membership function equal to 0.5.

The aggregation values A_i are modified according to the location of the radar bin respect to the melting layer height. The aggregation value of frozen hydrometeors are suppressed below the melting layer bottom, conversely the aggregation value of liquid precipitation types and biological scatterers are suppressed above the melting layer top. The mixed-phase hydrometeors can exist only within the melting layer. Due to the radar beam broadening mixed-phase particles can partially fill the radar bin volume even if the radar bin center is outside of the melting layer. In extreme cases the radar bin volume could be larger than the melting layer width and include hydrometeors of any type. For this reason, broad boundary regions at the melting layer top and bottom have been defined. Within this regions multiple types of hydrometeors can be identified by the algorithm. The boundary region width increases with the bin volume range according with the beam broadening.

Due to the additive aggregation formula adopted (equation 6.1) for the computation of the class aggregation value, a non-zero aggregation value is obtained even if not all the polarimetric characteristics of the specified class are met by the measurement. In some circumstances (particularly in the case of weak radar signal) the classification algorithm could produce clearly wrong class designation. The consistency of the classification results with the observed polarimetric properties of precipitation is further guaranteed by applying "hard thresholds" to the classification output. For example, hail is considered to be misclassified if $Z < 40$ dBZ. In such cases the algorithm accepts the class with the next highest aggregation value.

The results of the HCA applied to the radar measurement of 30 July 2014 along with the measured copolar radar reflectivity at horizontal polarization are shown in figure 6.5. This summer case has been selected because it clearly shows the capabilities of the HCA method, separating different types of hydrometeor including liquid, frozen and melting particles. The lowest elevation radar sweep of 0.5° is used for this case seeking for the inclusion of ground clutter and other type of non-meteorological scatterers. The HCA implementation has correctly detected the ground clutter due to the mountain top of the Apennines mountains and the Alps, at South-West and North-West of the radar (purple dots in the figure). The figure shows a vast rain precipitation area (yellow color) surrounded by a nearly circular wet snow band (lighter blue) indicating a nearly horizontally homogeneous melting layer height which is consistent with the stratiform nature of the precipitation event and the location of the melting layer is also consistent with the freezing level measured by the closest radio sounding. Above the melting layer the hydrometeor type is correctly classified as snow. Some big drops class echoes are found embedded in the Apennines mountains in accordance with the ground observations and the intense nature of the precipitation event.

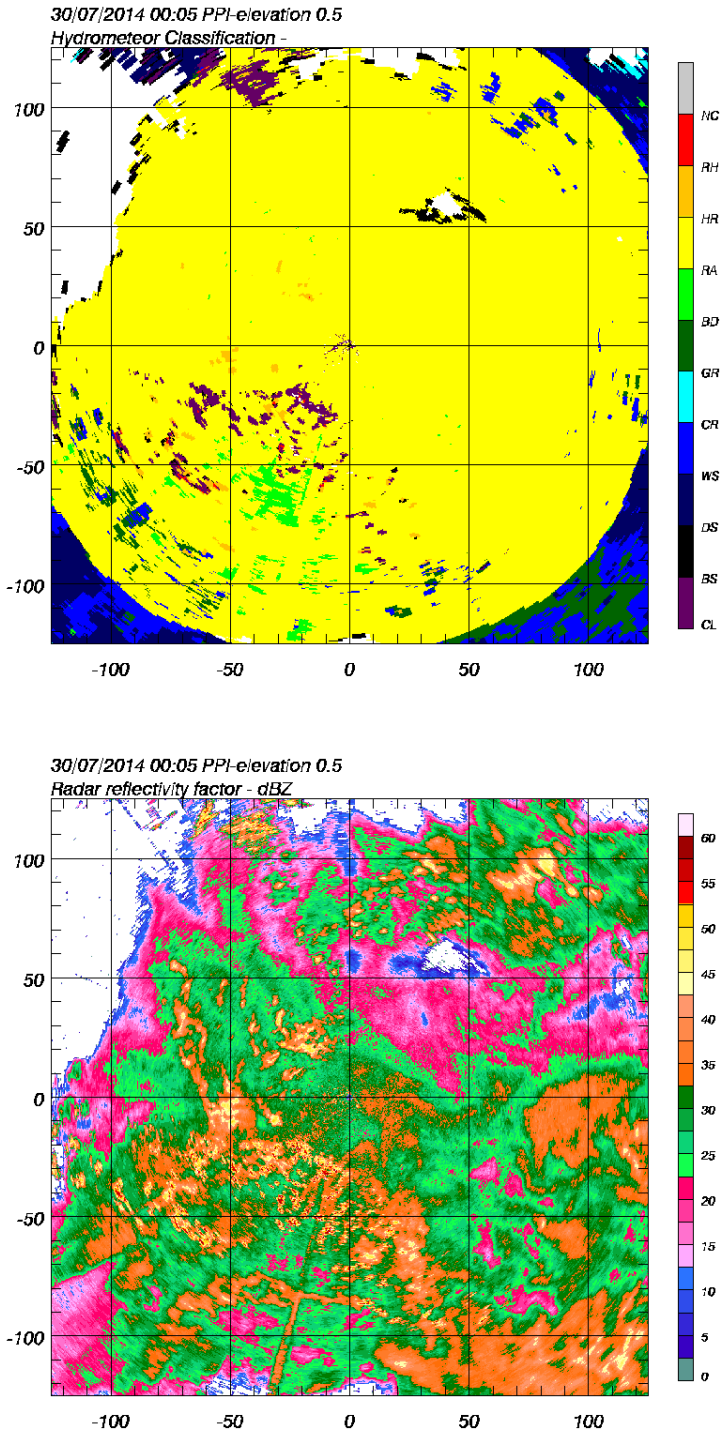

Fig. 6.5 Results of the classification algorithm for the precipitation event of 30 July 2014 observed by the San Pietro Capofiume (SPC) polarimetric radar which located at the center of each image. The top and bottom panels show respectively the 0.5° elevation PPI of echo class and measured radar reflectivity at horizontal polarization.

Chapter 7

Conclusion and discussion

The work presented in this study aims at improving the retrieval capabilities of snow precipitation through remote sensing instruments. Given the large interest of the scientific community and the characteristics of the ongoing and planned precipitation measurement satellite mission, this study focused mainly on microwave and radar measurement techniques.

This research does not look at just one particular aspect of the snowfall retrieval problem, but tries to address it as a whole, finding consistent results among the different areas of study investigated. This work studied separately the single particle properties of snowflakes and the characteristics of snowfall particle distribution, finding a solution that combines them in a self-consistent way and that is further confirmed by independent techniques and the experimental observations.

A state of the art snow aggregation algorithm (SAM) has been implemented to model the snowflake accurate morphology, simulating the basic physical governing phenomena of snow formation and growth. The algorithm has been further extended to model the initial stage of snowflake melting. The modeling study aims at simulating physically based complex snowflake habits that are able to catch the universal features of snow aggregates, such as the dependence of the snowflake to the particle dimension, aspect ratio and the aggregate fractal dimension.

The SAM model uses basic crystal shapes such as hexagonal columns and plates, bullet rosettes, droxtals and dendrites with variable linear dimension and random orientation as building blocks of complex snowflake aggregates. The implemented aggregation process is sufficiently versatile to model the aggregation of crystals of arbitrary shapes and sizes. The simulation proceeds by randomly aggregating ice crystals according the aggregation probability defined by the physical process of differential sedimentation. The resulting aggregates are highly detailed and represent well the morphological properties of natural aggregate snowflakes.

The snowflake models are used as input of discrete dipole approximation (DDA) scattering calculation. This is a flexible technique that does not places any restrictions on shape and internal structure of scattering particles. In the DDA, a target is replaced with a set of polarizable dipoles that reproduce its shape and dielectric properties. Since the SAM aggregates are defined by the cluster of the geometrical solid shapes of the constituent particles, the same aggregate model could be used to produce multiple DDA input shapes, with finer and finer dipole spacing resolution, just applying an ordinary point in polyhedron algorithm. This characteristics gives the opportunity to investigate the results of scattering computation with increasing accuracy.

The SAM method can also simulate the growth of a single aggregate particle using a controllable continuous collection aggregation process, that statistically constrain the modeled particle to follow a specified mass-size relationship. Since the shapes of the largest particles are obtained by aggregating additional crystals to an agglomerate of smaller ones the specified mass-size relation does not only represents the mass of the aggregate as a function of its size, but also describes the mass distribution within each particle. This feature has been used to investigate the importance of the radial distribution of mass within the aggregate in determining the snowflake radiative properties.

The radiative properties of the simulated particles are computed using the DDA method at 7 frequencies. Results from the ADDA-SAM models are compared to those of simplified spherical objects computed using the Mie solution. Different levels of accuracy for the representation of the radial mass distribution of the spherical targets are adopted. The highest degree of approximation of the complex aggregate using the spherical assumption is obtained by modeling a layered sphere with the exact radial density distribution of the SAM snowflake. The comparison between the radiative quantities calculated with the different models addresses the problem of the determination of the range of applicability of the spherical approximation for the modeling of complex snowflakes in radiative transfer studies. The analysis of the radiative properties obtained with the spherical models and the complex aggregated particles produced by SAM shows that the former are inadequate to represent the scattering characteristics of large aggregated particles.

In particular the DDA radar backscattering cross sections are up to 3 orders of magnitude larger than those of Mie solution. Large differences in the phase functions are observed between the different models. Otherwise, differences in the total scattering cross-sections are less significant. The backscattering cross sections are integrated over a set of PSDs in order to evaluate the sensitivity of radar parameters to the different models of snowflakes. Substantial differences between the radiative properties calculated using complex models and those obtained from simplified spherical models are observed. The calculations of the radar

equivalent reflectivity has been found to be largely sensitive to the radar backscattering model as well as the mass-dimension relationship and the PSDs used to describe the precipitation.

The modeling of melting snowflakes allows to simulate the transition from the radiative properties of a dry snowflake to those of a mixed-phase particle, which are of primary importance for the remote sensing of midlatitude precipitation. A direct comparison of the single-scattering properties of dry and wet snowflakes with the same mass, dimension, and shape is performed. Since a relevant melting process would change the morphology of the snowflake, the proposed method is not appropriate to model mixed-phase particles with large values of melted fraction. Future work will focus on the representation of wet snow with any value of melted fractions.

The simulation of the scattering properties of realistic models of partially melted snowflakes is further limited by the increased computational cost of DDA when mixtures multiple substances are included in the scattering target. In particular the inclusion of water increases the time required to complete the DDA calculations up to two orders of magnitude respect to the dry particle. For this reason an innovative formulation of the DDA methodology that makes uses of a memory efficient DDA formulation and exploits graphics processing units to accelerate the computations has been implemented. Unfortunately, it has not been possible to have access to powerful hardware to test the relative performance of the new implementation on practical snowflake scattering problems, but the early results obtained on simpler problems with low-end hardware are still promising.

The results of the scattering simulations highlights the fact that the uncertainties in the snow retrieval models arises not only from the scattering model adopted, but also from the microphysical parameterization of snow distributions and in particular the mass-size relation used. This is a hard problem since the single particle mass is difficult to measure and historically most of the measured mass-size relation required an enormous amount of effort and the samples has been consequently small in number and short in duration.

An innovative methodology has been developed to automatically estimate the mean snow mass-size relation using particle size distribution (PSD), velocity fits, snow accumulation and Rayleigh radar reflectivity. The model assumes that both the mass-size and the velocity-size relation can be approximate with a power law. It is shown that within the power-law assumption the particular couple of precipitation accumulation and radar reflectivity measured depends only on the exponent β of the mass size relation. The method is therefore able to retrieve a mass-size relation for the snowfall that accurately reproduce the precipitation gauge and near-Rayleigh radar measurements.

The mass-size retrieval method, has been tested against the Böhm's method which is based on the accurate modeling of snowflake aerodynamics and attempt to retrieve the mass of single

particles observed by a 2-dimensional video disdrometer (2DVD). The comparison shows a general good agreement between the two methods and underline the specific limitations of each of them. Being two different approaches, based on diverse physical principles and performed on the base of distinct instruments, the general good agreement of the retrieved microphysical properties is an indication of the theoretical correctness of both methods.

The 2DVD based method suffer from low intensity snowfall events because of the small sampling area of the 2DVD instrument and thus fails to estimate the power law fit when just few particles are observed. On the other hand, the developed Moment's Ratio Microphysical Retrieval method (MRRM) needs to synchronize and average in time the observation of the radar and the PIP disdrometer with the time interval required by the snow gauge to reach the minimum sampling resolution. The method assumes that, during this time period, the microphysical properties of the precipitating snow particles do not change. Being a bulk approach, the accuracy of the microphysical retrieval method is degradeted when multiple types of particles are included in the same averaging period.

The microphysical retrieval method is based on the fact that the reflectivity weighted bulk density and the snow rate weighted bulk density are inherently distinct quantities. It is important to note this difference and not use one in substitution of the other. It is common practice to try to reproduce radar measurement using disdrometer and snow gauge derived bulk density. In such case, one should not expect to be able to reproduce radar reflectivities even in the Rayleigh scattering regime.

The radar reflectivities at Ka and W band simulated with T-matrix spheroidal models and using the retrieved mass-dimensional relation cannot match the observation. This result reaffirm the fact that spheroidal shapes are unable to reproduce high frequency radar measurements. When the same simulation is performed with the usage of DDA scattering calculations the results reproduce better the observed radar reflectivities. This outcome gives validity to both the microphysical and the scattering model.

There are some circumstances where the DDA scattering calculations fail to reproduce the triple frequency radar measurements. There are indications that this failure happens when the assumptions behind the microphysical retrieval method breaks, but further investigations are needed to understand these last findings. The results are still promising and the triple-frequency measurement could be possibly used to detect the cases where the microphysical retrieval method fails.

A fuzzy logic hydrometeor classification algorithm has been implemented and made operational at the Emilia Romagna region environmental protection agency (ARPA-ER). The classification methodology is based on the statistical observed characteristics of different hydrometeor types. Future works will aim to develop a robust characterization of ice and

snow scattering properties based on the recent findings discussed in this thesis in order to develop a physically based classification method for snowfall.

The contemporary economic and social activities are largely affected by the environmental conditions including precipitation. It is likely to observe an increasing demand of accurate, continuous, reliable and global measurement of precipitation including snowfall. There is therefore an urgent need of physically consistent methods for snowfall remote sensing. The author believe that a multi-perspective approach, that simultaneously include the microphysical and scattering simulation of snowflake properties, is the way forward to solve the uncertainties related to snowfall remote sensing.

Appendix A

Radar measurements

A.1 Derivation of Z_e for snowflakes in Rayleigh regime

The radar backscattering cross section for a generic snowflake of size D in the Rayleigh regime is given by

$$\sigma_{bk}^{R} = \frac{\pi^5 D^6}{\lambda^4} \left(\frac{\varepsilon_{snow} - 1}{\varepsilon_{snow} + 2} \right)^2 \tag{A.1}$$

where $\varepsilon_{snow} = n_{snow}^2$ is the relative dielectric constant of the snow particle. The term bounded in the round parenthesis in equation A.1 is the dielectric constant of the snowflake $|K_{snow}|^2 = (\varepsilon_{snow} - 1)^2/(\varepsilon_{snow} + 2)^2$. The definition of radar equivalent reflectivity factor for a general family of scatterers with radar backscattering cross section $\sigma(D)$ is

$$Z_e = \frac{\lambda^4}{\pi^5 |K_w|^2} \int_{\min(D)}^{\max(D)} \sigma_{bk}(D) N(D)\, dD \tag{A.2}$$

The substitution of equation A.1 into equation A.2 gives the radar equivalent reflectivity factor for a generic population of snow particles

$$Z_e^R = \frac{1}{|K_w|^2} \int_{\min(D)}^{\max(D)} |K_{snow}(D)|^2 D^6 N(D)\, dD \tag{A.3}$$

The dielectric of the snowflake depends on the snowflake size. Aiming to find the dielectric properties of snow, the Maxwell-Garnett effective medium approximation (equation 2.28) for a mixture of ice inclusions in an air matrix[1] is

$$f_i \frac{\varepsilon_{ice} - 1}{\varepsilon_{ice} + 2} = \frac{\varepsilon_{snow} - 1}{\varepsilon_{snow} + 2} \tag{A.4}$$

[1] Remember that the relative dielectric constant of air is $\varepsilon_{air} = 1$

It is possible to recognize the dielectric factor of ice and the dielectric factor of snow respectively on the left hand side and on the right hand side of equation A.4.

$$f_i \, K_{ice} = K_{snow} \tag{A.5}$$

The volume fraction of ice inclusions f_i is defined as the ratio between the fractional volume of the snow particle occupied by the ice crystals and the total volume of the particle. This definition is rewritten in terms of densities considering that the total particle mass coincide with the mass of the ice part.

$$f_i = \frac{V_{ice}}{V} = \left(\frac{m_{ice}}{\rho_{ice}}\right) \Big/ \left(\frac{m_{ice}}{\rho_{snow}}\right) = \frac{\rho_{snow}}{\rho_{ice}} \tag{A.6}$$

Finally, the combination of equation A.6, A.5 and A.3 gives the equivalent radar reflectivity for snowflakes as a function of the snow particle densities

$$Z_e^R = \frac{1}{\rho_{ice}^2 |K_w|^2} \int_{\min(D)}^{\max(D)} \rho_{snow}^2(D) D^6 N(D) \, dD \tag{A.7}$$

A.2 Calibration correction of reflectivity measurements

The C-band Ikaalinen radar (Ika), belonging to the finnish national weather surveillance radar network, was used to check the calibration of the BAECC radars.

The Ika radar is a dual-polarization radar operating at a nominal wavelength of 5.3 cm and it is located 64 km South-West respect to the Hyytiälä forest field station. During the BAECC campaign, the Ika radar scanning strategy has been modified in order to measure a range-height indicator scan (RHI) above Hyytiälä every 15 minutes. The vertical reflectivity profile derived from the RHI scans has been compared with the vertical pointing profile of the XSACR radar (figure A.1) for the three distinct snow events analyzed in section 5.2.3.

The XSACR profile has been smoothed with a gaussian running window according to the Ika radar beamwidth at 64 km (approximately 1 km wide). The results are shown in figure A.2. The two reflectivity profiles match perfectly.

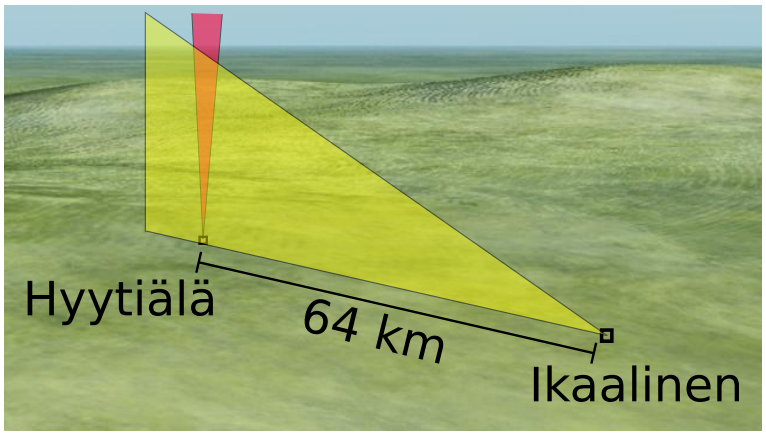

Fig. A.1 Relative position and observation strategy of the Ikaalinen C-band scanning radar and the XSACR vertically pointing radar.

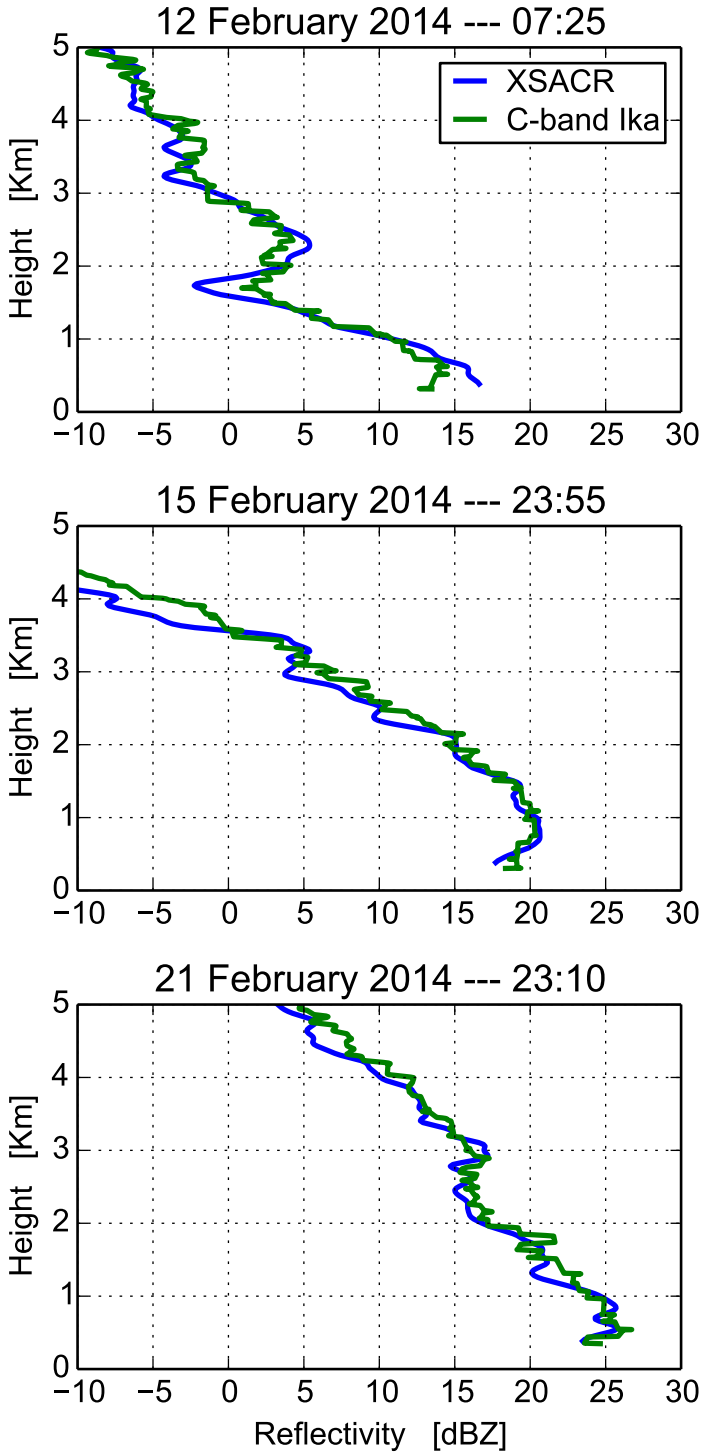

Fig. A.2 Reflectivity profiles from XSACR and Ika C-band data.

Appendix B

Particle imager dimensional correction

What is the size of a snowflake?

Snowflakes are generally complex-shaped particles and depending on the context, it arbitrary to use different definition of the snowflake "size". The particle "size" used may be the actual maximum dimension, the volume equivalent spherical diameter, the projected surface area equivalent spherical diameter, or the mass equivalent spherical diameter, among others. For many studies, it is necessary to convert from one size definition to another, especially when size-dependent parameters, obtained from a variety of sources are used (Petty and Huang, 2011).

Moreover, imaging disdrometers such as the Particle Image Package (PIP) and the 2-D Video Disdrometer (2DVD) are not able to access the total 3D complex shape of analyzed particles and thus, the measured particle size is just an approximation of the size definition derived from a single or a double side projection. In particular it is expected that particle sizes determined with such instruments always underestimate the true maximum dimension and underestimates the equivalent volume diameter in most cases (with the exception of single ice crystals exhibiting extreme aspect ratios).

Wood et al. (2013) established a theoretical and statistical method to estimate the the correction factor to be applied to measured sizes in order to obtain the particle maximum dimension. The same concept has been used to evaluate the correction factor to be applied to the PIP measured particle diameter D_{ec} (the diameter of a circle with the same projected area) in order to obtain the equivalent volume diameter D_{vol}.

Idelized snow particles has been modeled as tri-axial ellipsoids and their side-projected shapes has been evaluated. The ellipsoid are defined using their three distinct axis a b and c, where a is the major axis (also the "particle" maximum dimension D_{max}) and c is the minor (shortest) axis which was set to be oriented along the z-axis of the Cartesian reference frame.

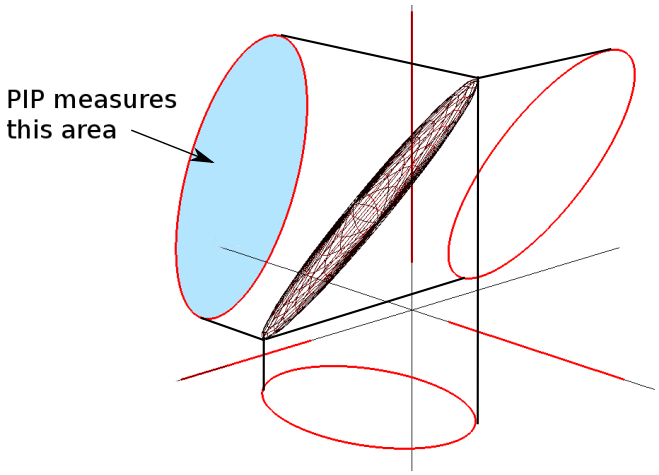

Fig. B.1 The theoretical scalene ellipsoid and its three projected ellipses

Particle orientation was varied by applying rotations around the y-axis with a canting angle extracted from a gaussian distribution with a standard deviation of 9° and limited over the range $\pm$ 21°, based on the estimates of Matrosov et al. (2005b). The particle has been also rotated uniformly around the z-axis.

The theoretical D_{ec} measured by the PIP instrument is derived from the ellipse projected onto the zx-plane for each particle orientation as it is shown in figure B.1.

The D_{ec} value averaged over the all orientation is calculated for ellipsoid with various axis ratios c/a and b/a. The value of the major axis a was fixed to 1, while the other two axis where varied among all possible ranges $[0.1 \leq b \leq a]$ and $[0.1 \leq c \leq b]$. These ranges produce particles that vary from needle-like to plate-like to spherical. The equivalent volume diameter for a generic ellipsoid is $D_{vol} = \sqrt[3]{abc}$.

In analogy with the study of Wood et al. (2013) the correction factor ϕ_{vol} as the ratio between D_{vol} and D_{ec} and the correction factor ϕ_{max} as the ratio between D_{max} and D_{ec}.

The mean correction factor ϕ_{vol} obtained from these simulations is shown in figure B.2 for various values of the aspect ratios c/a and b/a. The correction term respect to the maximum dimension ϕ_{max} is also shown.

The mean values of ϕ_{vol}, range from 0.8 to 1.5 whereas the mean value of ϕ_{max} range from 0.25 to 1. ϕ_{vol} is sensitive to both the vertical aspect ratio c/a and the horizontal aspect ratio b/a, while ϕ_{max} is mostly sensitive to the vertical aspect ratio only.

The correction factor of 1.11 applied in the MRRM retrieval (chapter 5) is defined from $1/\phi_{vol}$ for the ellipsoid with aspect ratio of 0.6, which is typical for snowflake aggregates (Hogan et al., 2012; Korolev et al., 2003).

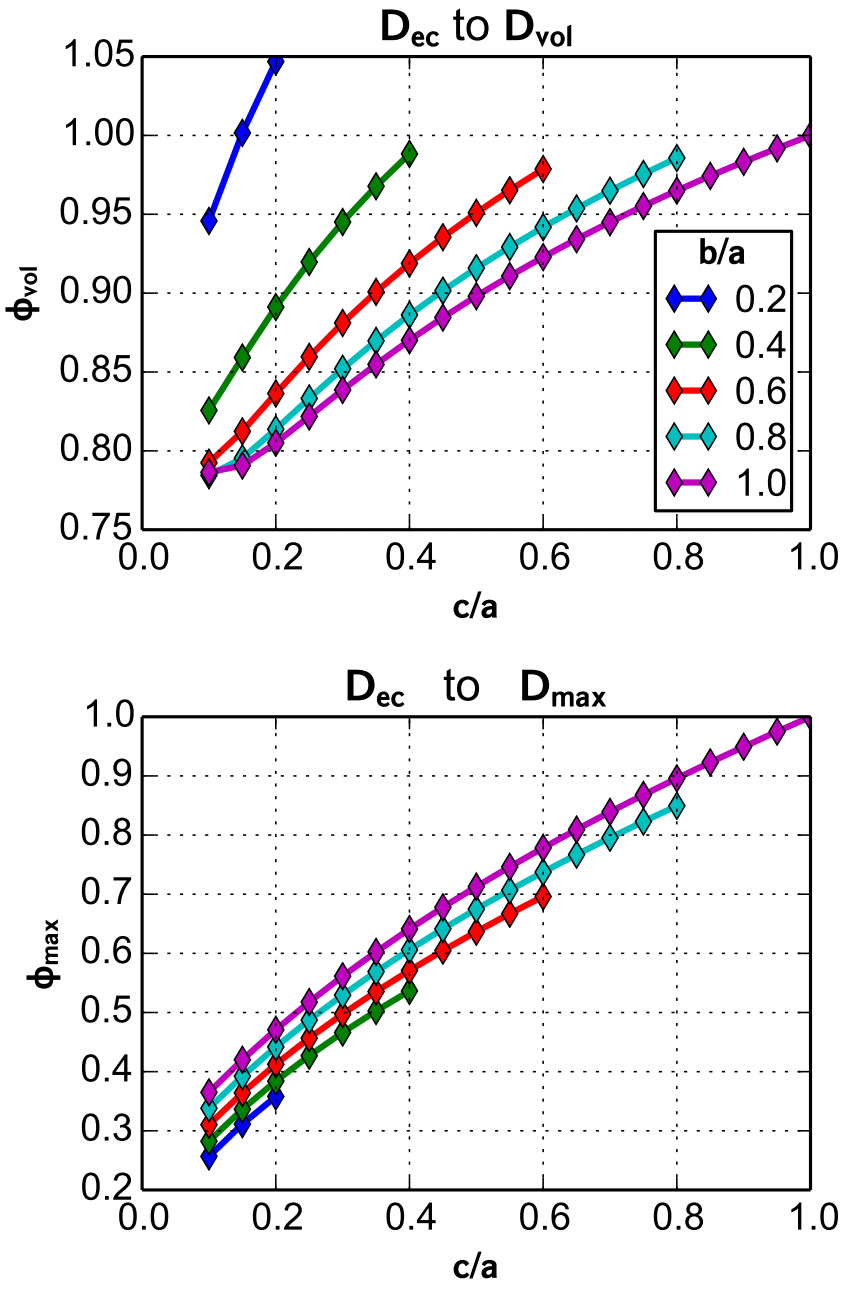

Fig. B.2 ϕ_{vol} and ϕ_{ec} as a function of the vertical and horizontal aspect ratio.

Bibliography

Aden, A. L. and Kerker, M. (1951). Scattering of electromagnetic waves from two concentric spheres. *Journal of Applied Physics*, 22(10):1242–1246.

Ahrens, J., Geveci, B., and Law, C. (2005). 36 paraview: An end-user tool for large-data visualization. *The Visualization Handbook*, page 717.

Atlas, D., Ulbrich, C. W., Marks, F. D., Amitai, E., and Williams, C. R. (1999). Systematic variation of drop size and radar-rainfall relations. *Journal of Geophysical Research: Atmospheres (1984–2012)*, 104(D6):6155–6169.

Behrangi, A., Stephens, G., Adler, R. F., Huffman, G. J., Lambrigtsen, B., and Lebsock, M. (2014). An Update on the Oceanic Precipitation Rate and Its Zonal Distribution in Light of Advanced Observations from Space. *Journal of Climate*, 27(11):3957–3965.

Bennartz, R. and Petty, G. W. (2001). The sensitivity of microwave remote sensing observations of precipitation to ice particle size distributions. *Journal of Applied Meteorology*, 40(3):345–364.

Böhm, H. P. (1989). A general equation for the terminal fall speed of solid hydrometeors. *Journal of the Atmospheric Sciences*, 46(15):2419–2427.

Bohren, C. and Huffman, D. (1983). *Absorption and Scattering of Light by Small Particles*. Wiley-Interscience.

Bohren, C. F. and Battan, L. J. (1980). Radar backscattering by inhomogeneous precipitation particles. *Journal of the Atmospheric Sciences*, 37(8):1821–1827.

Botta, G. and Aydin, K. (2010). Modeling of Microwave Scattering From Cloud Ice Crystal Aggregates and Melting Aggregates: A New Approach. *Geosci. Remote Sens. Lett.*, 7(3):572–576.

Botta, G., Aydin, K., Verlinde, J., Avramov, A. E., Ackerman, A. S., Fridlind, A. M., McFarquhar, G. M., and Wolde, M. (2011). Millimeter wave scattering from ice crystals and their aggregates: Comparing cloud model simulations with x- and ka-band radar measurements. *Journal of Geophysical Research: Atmospheres*, 116(D1). D00T04.

Botta, G., Scaranari, D., Montopoli, M., and Marzano, F. (2008). Backscattering Modeling for Polarimetric Radar Observation of Ice Crystals and Aggregates from C to Ka Band. *ERAD2008 Fifth European Conference on Radar in Meteorology and Hydrology*.

Brandes, A., Ikeda, K., Zhang, G., Schonhuber, M., and Rasmussen, R. M. (2007). A Statistical and Physical Description of Hydrometeor Distributions in Colorado Snowstorms Using a Video Disdrometer. *Jour. App. Met. Clim.*, 46(5):634–650.

Bringi, V. N. and Chandrasekar, V. (2001). *Polarimetric Doppler weather radar: principles and applications*. Cambridge University Press.

Bringi, V. N., Keenan, T., and Chandrasekar, V. (2001). Correcting c-band radar reflectivity and differential reflectivity data for rain attenuation: A self-consistent method with constraints. *Geoscience and Remote Sensing, IEEE Transactions on*, 39(9):1906–1915.

Bruggeman, V. D. (1935). Berechnung verschiedener physikalischer konstanten von heterogenen substanzen. i. dielektrizitätskonstanten und leitfähigkeiten der mischkörper aus isotropen substanzen. *Annalen der physik*, 416(8):665–679.

Cadeddu, M., Liljegren, J., and Turner, D. (2013). The atmospheric radiation measurement (arm) program network of microwave radiometers: Instrumentation, data, and retrievals. *Atmospheric Measurement Techniques*, 6(9):2359–2372.

Dash, J., Rempel, A., and Wettlaufer, J. (2006). The physics of premelted ice and its geophysical consequences. *Reviews of modern physics*, 78(3):695.

DeVoe, H. (1964). Optical Properties of Molecular Aggregates. I. Classical Model of Electronic Absorption and Refraction. *J. Chem. Phys*, 41(2):393–400.

Draine, B. and Flatau, P. (1994). Discrete-dipole approximation for scattering calculations. *J. Opt. Soc. Am. A*, 11(4):1491–1499.

Eccles, P. J. and Mueller, E. A. (1971). X-band attenuation and liquid water content estimation by a dual-wavelength radar. *Journal of Applied Meteorology*, 10(6):1252–1259.

Ellison, W. (2007). Permittivity of pure water, at standard atmospheric pressure, over the frequency range 0–25 thz and the temperature range 0–100 c. *J. Phys. Chem. Ref. Data*, 36(1):1–18.

Ellison, W., Lamkaouchi, K., and Moreau, J.-M. (1996). Water: a dielectric reference. *Journal of Molecular Liquids*, 68(2):171–279.

Evans, K., Walter, S., Heymsfield, A., and Deeter, M. (1998). Modeling of Submillimeter Passive Remote Sensing of Cirrus Clouds. *Jour. App. Met. Clim.*, 37:184–204.

Evans, K. F., Wang, J. R., Racette, P. E., Heymsfield, G., and Li, L. (2005). Ice cloud retrievals and analysis with the compact scanning submillimeter imaging radiometer and the cloud radar system during crystal face. *Journal of Applied Meteorology*, 44(6):839–859.

Fabry, F. and Szyrmer, W. (1999). Modeling of the Melting Layer. Part II: Electromagnetic. *Jour. Atm. Sciences*, 56:3593–3600.

Field, P. and Heymsfield, A. (2003). Aggregation and Scaling of Ice Crystal Size Distributions. *Jour. Atm. Sciences*, 60(3):544–560.

Field, P. and Heymsfield, A. (2007). Snow Size Distribution Parameterization for Midlatitude and Tropical Ice Clouds. *Jour. Atm. Sciences*, 64:4346–4365.

Field, P., Heymsfield, A., and Bansemer, A. (2006). Shattering and particle interarrival times measured by optical array probes in ice clouds. *Journal of Atmospheric and Oceanic Technology*, 23(10):1357–1371.

Field, P., Hogan, R., Brown, P., Illingworth, A., Choularton, T., and Cotton, R. (2005). Parametrization of ice-particle size distributions for mid-latitude stratiform cloud. . *Quart. J. Roy. Meteor. Soc.*, 131:1997–2017.

Foster, T. and Hallett, J. (2002). The alignment of ice crystals in changing electric fields. *Atmospheric research*, 62(1):149–169.

Frigo, M. and Johnson, S. (2005). The design and implementation of FFTW3 . *IEEE Proc.*, 93:216–231.

Fujiyoshi, Y. (1986). Melting snowflakes. *Journal of the atmospheric sciences*, 43(3):307–311.

Ganesh, M. and Hawkins, S. C. (2008). A far-field based t-matrix method for three dimensional acoustic scattering. In Mercer, G. N. and Roberts, A. J., editors, *Proceedings of the 14th Biennial Computational Techniques and Applications Conference, CTAC-2008*, volume 50 of *ANZIAM J.*, pages C121–C136. http://anziamj.austms.org.au/ojs/index.php/ANZIAMJ/article/view/1441.

Garrett, T., Fallgatter, C., Shkurko, K., and Howlett, D. (2012). Fall speed measurement and high-resolution multi-angle photography of hydrometeors in free fall. *Atmospheric Measurement Techniques*, 5(11):2625–2633.

Garrett, T. J. and Yuter, S. E. (2014). Observed influence of riming, temperature, and turbulence on the fallspeed of solid precipitation. *Geophysical Research Letters*, 41(18):6515–6522.

Garrett, T. J., Yuter, S. E., Fallgatter, C., Shkurko, K., Rhodes, S. R., and Endries, J. L. (2015). Orientations and aspect ratios of falling snow. *Geophysical Research Letters*.

Gayet, J.-F., Febvre, G., and Larsen, H. (1996). The reliability of the pms fssp in the presence of small ice crystals. *Journal of Atmospheric and Oceanic Technology*, 13(6):1300–1310.

Giangrande, S. E., Krause, J. M., and Ryzhkov, A. V. (2008). Automatic Designation of the Melting Layer with a Polarimetric Prototype of the WSR-88D Radar. *Jour. App. Met. Clim.*, 47:1354–1364.

Gillespie, D. (1975). An Exact Method for Numerically Simulating the Stochastic Coalescence Process in a Cloud. *Jour. Atm. Sciences*, 32:1977–1989.

Goodman, J., Draine, B., and Flatau, P. (1991). Application of fast-Fourier-transform tchniques to the discrete-dipole approximation. *Opt. Lett.*, 16(15):1198–1200.

Gorgucci, E., Scarchilli, G., and Chandrasekar, V. (1992). Calibration of radars using polarimetric techniques. *Geoscience and Remote Sensing, IEEE Transactions on*, 30(5):853–858.

Gourley, J. J., Illingworth, A. J., and Tabary, P. (2009). Absolute calibration of radar reflectivity using redundancy of the polarization observations and implied constraints on drop shapes. *Journal of Atmospheric and Oceanic Technology*, 26(4):689–703.

Grecu, M. and Olson, W. (2008). Precipitating Snow Retrievals from Combined Airborne Cloud Radar and Millimeter-Wave Radiometer Observations. *Jour. App. Met. Clim.*, 47:1634–1649.

Gunn, K. and Marshall, J. (1958). The Distribution with Size of Aggregate Snowflakes. *J. Meteor.*, 15:452–461.

Hallett, J. (1974). Production of secondary ice particles during the riming process. *Nature*, 249:26–28.

Heymsfield, A. (1972). Ice Crystal Terminal Velocities. *Jour. Atm. Sciences*, 29:1348–1357.

Heymsfield, A., Bansemer, A., Schmitt, C., Twohy, C., and Poellot, M. (2004). Effective Ice Particle Densities Derived from Aircraft Data. *Jour. Atm. Sciences*, 61:982–1003.

Heymsfield, A., Field, P., and Bansemer, A. (2008). Exponential Size Distributions for Snow. *Jour. Atm. Sciences*, 65:4017–4031.

Heymsfield, A., Schmitt, C., and Bansemer, A. (2013). Ice Cloud Particle Size Distributions and Pressure Dependent Terminal Velocities from In Situ Observations at Temperatures from 0 to –86 C. *Jour. Atm. Sciences*.

Heymsfield, A. J., Bansemer, A., Field, P. R., Durden, S. L., Stith, J. L., Dye, J. E., Hall, W., and Grainger, C. A. (2002a). Observations and Parameterizations of Particle Size Distributions in Deep Tropical Cirrus and Stratiform Precipitating Clouds: Results from In Situ Observations in TRMM Field Campaigns. *Journal of the Atmospheric Sciences*, 59(24):3457–3491.

Heymsfield, A. J., Lewis, S., Bansemer, A., Iaquinta, J., Miloshevich, L. M., Kajikawa, M., Twohy, C., and Poellot, M. R. (2002b). A General Approach for Deriving the Properties of Cirrus and Stratiform Ice Cloud Particles. *Journal of the atmospheric sciences*, 59(1):3–29.

Heymsfield, A. J. and Westbrook, C. D. (2010). Advances in the estimation of ice particle fall speeds using laboratory and field measurements. *Journal of the Atmospheric Sciences*, 67(8):2469–2482.

Hogan, R. J. and Kew, S. F. (2005). A 3d stochastic cloud model for investigating the radiative properties of inhomogeneous cirrus clouds. *Q. J. R. Meteorol. Soc.*, 131(611, A):2585–2608.

Hogan, R. J., Mittermaier, M. P., and Illingworth, A. J. (2006). The retrieval of ice water content from radar reflectivity factor and temperature and its use in evaluating a mesoscale model. *Journal of Applied Meteorology and Climatology*, 45(2):301–317.

Hogan, R. J., Tian, L., Brown, P. R. A., Westbrook, C. D., Heymsfield, A. J., and Eastment, J. D. (2012). Radar scattering from ice aggregates using the horizontally aligned oblate spheroid approximation. *J. Appl. Meteorol. Climatol.*, 51(3):655–671.

Holland, M. and Bitz, C. (2003). Polar amplification of climate change in coupled models. *Climate Dynamics*, 21(3-4):221–232.

Holroyd, E. (1971). *The Meso - and Microscale Structure of Great Lakes Snowstorm - Synthesis of Ground Measurements, Radar Data, and Satellite Observations*. PhD thesis, State University of New York at Albany.

Hong, G. (2007a). Parameterization of scattering and absorption properties of nonspherical ice crystals at microwave frequencies. *Jour. Geo. Res*, 112.

Hong, G. (2007b). Radar Backscattering Properties of Nonspherical Ice Crystals at 94 GHz . *J. Geophys. Res.*, 112.

Hosler, C. and Hallgren, R. (1960). The aggregation of small ice crystals. *Discussions of the Faraday Society*, 30:200–207.

Hou, A. Y., Kakar, R. K., Neeck, S., Azarbarzin, A. A., Kummerow, C. D., Kojima, M., Oki, R., Nakamura, K., and Iguchi, T. (2013). The Global Precipitation Measurement Mission. *Bulletin of the American Meteorological Society*, 95(5):701–722.

Huang, G.-J., Bringi, V., Cifelli, R., Hudak, D., and Petersen, W. (2010). A methodology to derive radar reflectivity-liquid equivalent snow rate relations using c-band radar and a 2d video disdrometer. *Journal of Atmospheric and Oceanic Technology*, 27(4):637–651.

Huang, G.-J., Bringi, V. N., Moisseev, D., Petersen, W. A., Bliven, L., and Hudak, D. (2015). Use of 2d-video disdrometer to derive mean density–size and ze–sr relations: Four snow cases from the light precipitation validation experiment. *Atmospheric Research*, 153:34–48.

Hudak, D., Barker, H., Rodruguez, P., and Donovan, D. (2006). The canadian cloudsat/calipso validation project. In *Proc. Fourth European Conf. on Radar in Hydrology and Meteorology*, pages 609–612. ERAD Barcelona, Spain.

Huntemann, M., Heygster, G., and Hong, G. (2011). Discrete dipole approximation simulations on gpus using opencl—application on cloud ice particles. *Journal of Computational Science*, 2(3):262–271.

Huuskonen, A., Saltikoff, E., and Holleman, I. (2014). The operational weather radar network in europe. *Bulletin of the American Meteorological Society*, 95(6):897–907.

Illingworth, A. J., Barker, H. W., Beljaars, A., Ceccaldi, M., Chepfer, H., Cole, J., Delanoë, J., Domenech, C., Donovan, D. P., Fukuda, S., Hirakata, M., Hogan, R. J., Huenerbein, A., Kollias, P., Kubota, T., Nakajima, T., Nakajima, T. Y., Nishizawa, T., Ohno, Y., Okamoto, H., Oki, R., Sato, K., Satoh, M., Shephard, M., Wandinger, U., Wehr, T., and van Zadelhoff, G.-J. (2014). THE EARTHCARE SATELLITE: The next step forward in global measurements of clouds, aerosols, precipitation and radiation. *Bulletin of the American Meteorological Society*.

Ishimoto, H. (2008). Radar Backscattering Computations for Fractal-Shaped Snowflakes. *J. Meteor. Soc. Japan*, 86(3):459–469.

Jackson, J. D. (1962). *Classical electrodynamics*, volume 3. Wiley New York.

Jiusto, J. E. and Weickmann, H. K. (1973). Types of snowfall. *Bulletin of the American Meteorological Society*, 54(11):1148–1162.

Johnson, B. T., Olson, W. S., and Skofronick-Jackson, G. (2015). The microwave properties of simulated melting precipitation particles: sensitivity to initial melting. *Atmospheric Measurement Techniques Discussions*, 8(6):5615–5649.

Johnson, B. T., Petty, G. W., and Skofronick-Jackson, G. (2012). Microwave properties of ice-phase hydrometeors for radar and radiometers: Sensitivity to model assumptions. *Journal of Applied Meteorology and Climatology*, 51(12):2152–2171.

Kahnert, M. (2013). The T-matrix code Tsym for homogeneous dielectric particles with finite symmetries. *Journal of Quantitative Spectroscopy and Radiative Transfer*, 123:62–78. Peter C. Waterman and his scientific legacy.

Kajikawa, M. (1972). Measurement of falling velocity of individual snow crystals. *Journal of the Meteorological Society of Japan*, 50(6):276–283.

Kajikawa, M. (1975). Experimental formula of falling velocity of snow crystals. *Journal of the Meteorological Society of Japan*, 53(4):267–275.

Kajikawa, M. (1976). Observation of falling motion of columnar snow crystals. *Journal of the Meteorological Society of Japan*, 54(5):276–283.

Kajikawa, M. (1992). Observations of the falling motion of plate-like snow crystals. part I: The free-fall patterns and velocity variations of unrimed crystals. *Journal of the Meteorological Society of Japan*, 70(1):1–9.

Kidd, C., Levizzani, V., Turk, J., and Ferraro, R. (2009). Satellite Precipitation Measurment for Water Resource Monitoring. *J. Am. Water Resour. As.*, 45(3):567–579.

Kim, M.-J. (2006). Single scattering parameters of randomly oriented snow particles at microwave frequencies. *Journal of Geophysical Research: Atmospheres*, 111(D14). D14201.

Klett, J. D. (1995). Orientation model for particles in turbulence. *Journal of the atmospheric sciences*, 52(12):2276–2285.

Kneifel, S., Kulie, M. S., and Bennartz, R. (2011). A triple-frequency approach to retrieve microphysical snowfall parameters. *Journal of Geophysical Research: Atmospheres*, 116(D11). D11203.

Kneifel, S., Löhnert, U., Battaglia, A., Crewell, S., and Siebler, D. (2010). Snow scattering signals in ground-based passive microwave radiometer measurements. *Journal of Geophysical Research: Atmospheres*, 115(D16). D16214.

Kneifel, S., von Lerber, A., Tiira, J., Moisseev, D., Kollias, P., and Leinonen, J. (2015). Observed relations between snowfall microphysics and triple-frequency radar measurements. *Journal of Geophysical Research: Atmospheres*, 120(12):6034–6055. 2015JD023156.

Knight, C. A. (1979). Observations of the morphology of melting snow. *Journal of the Atmospheric Sciences*, 36(6):1123–1130.

Kollias, P., Albrecht, B., and Marks Jr, F. (2002). Why mie? accurate observations of vertical air velocities and raindrops using a cloud radar. *Bulletin of the American Meteorological Society*, 83(10):1471–1483.

Korkmaz, S. (2004). Radar Attenuation due to Melting: A Comparison of Physical Models Proposed for the Melting Morphology . *Atmos. Res.*, 70:261–274.

Korolev, A., Isaac, G., Cober, S., Strapp, J., and Hallett, J. (2003). Microphysical characterization of mixed-phase clouds. *Q. J. R. Meteorol. Soc.*, 129:39–65.

Korolev, A. V., Emery, E. F., Strapp, J. W., Cober, S. G., and Isaac, G. A. (2013). Quantification of the Effects of Shattering on Airborne Ice Particle Measurements. *Journal of Atmospheric and Oceanic Technology*, 30(11):2527–2553.

Korolev, A. V., Emery, E. F., Strapp, J. W., Cober, S. G., Isaac, G. A., Wasey, M., and Marcotte, D. (2010). Small Ice Particles in Tropospheric Clouds: Fact or Artifact? Airborne Icing Instrumentation Evaluation Experiment. *Bulletin of the American Meteorological Society*, 92(8):967–973.

Kruger, A. and Krajewski, W. (2002). Two-Dimensional Video Disdrometer: A Description. *J. Atmos. Oceanic. Technol.*, 19:602–617.

Kulie, M. and Bennartz, R. (2009). Utilizing Spaceborne Radars to Retrive Dry Snowfall. *Jour. App. Met. Clim.*, 48:2564–2580.

Kulie, M., Bennartz, R., Greenwald, T., Chen, Y., and Fuzhong, W. (2010). Uncertainties in Microwave Properties of Frozen Precipitation: Implications for Remote Sensing and Data Assimilation. *Jour. Atm. Sciences*, 67:3471–3487.

Kulie, M. S., Hiley, M. J., Bennartz, R., Kneifel, S., and Tanelli, S. (2014). Triple-frequency radar reflectivity signatures of snow: Observations and comparisons with theoretical ice particle scattering models. *Journal of Applied Meteorology and Climatology*, 53(4):1080–1098.

Kummerow, C., Barnes, W., Kozu, T., Shiue, J., and Simpson, J. (1998). The Tropical Rainfall Measuring Mission (TRMM) Sensor Package. *Journal of Atmospheric and Oceanic Technology*, 15(3):809–817.

Kyrouac, J. and Holdridge, D. (2014). Arm surface meteorological instrumentation (met).

Lane, J., Magedson, B., and Rarick, M. (1984). An efficient point in polyhedron algorithm. *Computer vision, graphics, and image processing*, 26(1):118–125.

Lanza, L., Leroy, M., Alexandropoulos, C., Stagi, L., and Wauben, W. (2006). Wmo laboratory intercomparison of rainfall intensity gauges. *Final report, WMO, Geneva*.

Lawson, R., Baker, B., and Schmitt, C. (2001). An Overview of Microphysical Properties of Artic Clouds Observed in May and July 1998 during FIRE ACE. *J. Geophys. Res.*, 106(D14):14989–15014.

Lawson, R. P. (2011). Effects of ice particles shattering on the 2d-s probe. *Atmospheric Measurement Techniques*, 4(7):1361–1381.

L'Ecuyer, T., Petersen, W., and Moisseev, D. (2010). The light precipitation validation experiment (lpvex): Overview and early results. *AGU Fall Meeting Abstracts*, page K2.

Leinonen, J. (2014). High-level interface to t-matrix scattering calculations: architecture, capabilities and limitations. *Optics express*, 22(2):1655–1660.

Leinonen, J., Kneifel, S., Moisseev, D., Tyynela, J., Tanelli, S., and Nousianen, T. (2012). Evidence of nonspheroidal behavior in millimeter-wavelength radar observations of snowfall. *J. Geophys. Res.*, 117(D18).

Leinonen, J. and Moisseev, D. (2015). What do triple-frequency radar signatures reveal about aggregate snowflakes? *Journal of Geophysical Research: Atmospheres*, 120(1):229–239.

Leinonen, J., Moisseev, D., and Nousiainen, T. (2013). Linking snowflake microstructure to multi-frequency radar observations. *J. Geophys. Res.*, 118(8):3259–3270.

Leinonen, J. and Szyrmer, W. (2015). Radar signatures of snowflake riming: A modeling study. *Earth and Space Science*. 2015EA000102.

Liao, L. and Meneghini, R. (2005). A study of air/space-borne dual-wavelength radar for estimation of rain profiles. *Advances in Atmospheric Sciences*, 22(6):841–851.

Liao, L., Meneghini, R., Iguchi, T., and Detwiler, A. (2005). Use of dual-wavelength radar for snow parameter estimates. *Journal of Atmospheric and Oceanic Technology*, 22(10):1494–1506.

Libbrecht, K. G. (2005). The physics of snow crystals. *Reports on progress in physics*, 68(4):855–895.

Lin, Y.-L., Farley, R. D., and Orville, H. D. (1983). Bulk parameterization of the snow field in a cloud model. *Journal of Climate and Applied Meteorology*, 22(6):1065–1092.

Liu, G. (2004). Approximation of Single Scattering Properties of Ice and Snow Particles for High Microwave Frequencies. *Jour. Atm. Sciences*, 61:2441–2456.

Liu, G. (2008a). A Database of Microwave Single-Scattering Properties for Nonspherical Ice Particles. *BAMS*, pages 1563–1570.

Liu, G. (2008b). Deriving snow cloud characteristics from CloudSat observations. *J. Geophys. Res.*, 113.

Locatelli, J. and Hobbs, P. (1974). Fall Speeds and Masses of Solid Precipitation Particles. *J. Geophys. Res.*, 79(15):2185–2197.

Löhnert, U., Kneifel, S., Battaglia, A., Hagen, M., Hirsch, L., and Crewell, S. (2011). A Multisensor Approach Toward a Better Understanding of Snowfall Microphysics: The TOSCA Project . *BAMS*, pages 613–628.

Magono, C. and Lee, C. (1966). Meteorological Classification of Natural Snow Crystals. *Journal of the Faculty of Science Kokkaido University*, 2(4):321–366.

Magono, C. and Nakamura, T. (1965). Aerodynamic Studies of Falling Snowflakes. *J. Meteor. Soc. Japan*, 43(3):139–147.

Marshall, J. S. and Palmer, W. M. K. (1948). The distribution of raindrops with size. *Journal of meteorology*, 5(4):165–166.

Maruyama, K.-I. and Fujiyoshi, Y. (2005). Monte Carlo Simulation of the Formation of Snowflakes. *Jour. Atm. Sciences*, 62(5):1529–1544.

Marzano, F., Botta, G., and Montopoli, M. (2010). Iterative Bayesian Retrieval of Hydrometeor Content From X-Band Polarimetric Weather Radar. *Trans. Geosci. Remote Sens.*, 48(8):3059–3074.

Marzano, F., Scaranari, D., and Vulpiani, G. (2007). Supervised Fuzzy-Logic Classification of Hydrometeors Using C-Band Weather Radars. *Trans. Geosci. Remote Sens.*, 45(11):3784–3799.

Matrosov, S. (1998). A Dual-Wavelength Radar Method to Measure Snowfall Rate. *Jour. App. Met. Clim.*, 37:1510–1521.

Matrosov, S. (2007). Modeling Backscattering Properties of Snowfall at Millimeter Wavelengths. *Jour. Atm. Sciences*, 64:1727–1736.

Matrosov, S. Y., Heymsfield, A. J., and Wang, Z. (2005a). Dual-frequency radar ratio of nonspherical atmospheric hydrometeors. *Geophys. Res. Lett.*, 32(13).

Matrosov, S. Y., Reinking, R. F., and Djalalova, I. V. (2005b). Inferring fall attitudes of pristine dendritic crystals from polarimetric radar data. *Journal of the atmospheric sciences*, 62(1):241–250.

Matsuo, T. and Sasyo, Y. (1981). Melting of snowflakes below freezing level in the atmosphere. *Journal of the Meteorological Society of Japan*, 59(1):10–24.

Matzler, C. (2006). *Thermal Microwave Radiation: Application for Remote Sensing*. Electromagnetic Series. IET.

Maxwell Garnett, J. (1904). Colours in metal glasses and in metallic films. *Philosophical Transactions of the Royal Society of London. Series A, Containing Papers of a Mathematical or Physical Character*, pages 385–420.

Meissner, T. and Wentz, F. (2004). The Complex Dielectric Constant of Pure and Sea Water From Microwave Satellite Observations. *Trans. Geosci. Remote Sens.*, 42(9):1836–1849.

Meneghini, R., Kozu, T., Kumagai, H., and Boncyk, W. (1992). A study of rain estimation methods from space using dual-wavelength radar measurements at near-nadir incidence over ocean. *Journal of Atmospheric and Oceanic Technology*, 9(4):364–382.

Mie, G. (1908). Beiträge zur optik trüber medien, speziell kolloidaler metallösungen. *Annalen der physik*, 330(3):377–445.

Mishchenko, M., Travis, L., and Lacis, A. (2002). *Scattering, Absorption, and Emission of Light by Small Particles*. Cambridge University Press.

Mishchenko, M. I. and Travis, L. D. (1998). Capabilities and limitations of a current fortran implementation of the t-matrix method for randomly oriented, rotationally symmetric scatterers. *Journal of Quantitative Spectroscopy and Radiative Transfer*, 60(3):309–324.

Mishchenko, M. I., Videen, G., Khlebtsov, N. G., and Wriedt, T. (2013). Comprehensive T-matrix reference database: A 2012–2013 update. *Journal of Quantitative Spectroscopy and Radiative Transfer*, 123:145–152. Peter C. Waterman and his scientific legacy.

Mitchell, D. (1996). Use of Mass- and Area-Dimensional Power Laws for Determining Precipitation Particle Terminal Velocities. *Jour. Atm. Sciences*, 53(12):1710–1723.

Mitchell, D. and Heymsfield, A. (2005). Refinements in the Treatment of Ice Particle Terminal Velocities, Highlighting Aggregates. *Jour. Atm. Sciences*, 62:1637–1644.

Mitchell, D., Zhang, R., and Pitter, R. (1990). Mass-dimensional relationships for ice particles and the influence of riming on snowfall rates. *Journal of Applied Meteorology*, 29(2):153–163.

Mitra, S., Vohl, O., Ahr, M., and Pruppacher, H. (1990). A wind tunnel and theoretical study of the melting behavior of atmospheric ice particles. iv: Experiment and theory for snow flakes. *Journal of the Atmospheric Sciences*, 47(5):584–591.

Mossop, S. (1976). Production of secondary ice particles during the growth of graupel by riming. *Quarterly Journal of the Royal Meteorological Society*, 102(431):45–57.

Muramoto, K., Matsuura, K., and Shiina, T. (1995). Measuring the density of snow particles and snowfall rate. *Electron. Comm. Jpn. Pt. III*, 78(11):71–79.

Nakaya, U. and Tereda, T. (1935). Simultaneous observations of the mass, falling velocity and form of individual snow crystals. *Journal of the Faculty of Science, Hokkaido Imperial University. Ser. 2, Physics*, 1(7):191–200.

Newman, A. and Kucera, P. (2009). Presenting the Snowflake Video Imager (SVI). *J. Atmos. Oceanic. Technol.*, pages 167–179.

Noh, Y.-J., Liu, G., Seo, E.-K., Wang, J. R., and Aonashi, K. (2006). Development of a snowfall retrieval algorithm at high microwave frequencies. *Journal of Geophysical Research: Atmospheres*, 111(D22).

Nowell, H., Liu, G., and Honeyager, R. (2013). Modeling the microwave single-scattering properties of aggregate snowflakes. *Jour. Geo. Res*, 118:7873–7885.

Oraltay, R. and Hallett, J. (2005). The Melting Layer: A Laboratory Investigation of Ice Particle Melt and Evaporation near 0C . *Jour. App. Met. Clim.*, 44:206–220.

Ori, D., Maestri, T., Rizzi, R., Cimini, D., Montopoli, M., and Marzano, F. S. (2014). Scattering properties of modeled complex snowflakes and mixed-phase particles at microwave and millimeter frequencies. *Journal of Geophysical Research: Atmospheres*, 119(16):9931–9947.

Ori, D., Moisseev, D., von Lerber, A., Huang, G.-J., Tiira, J., and Chandrasekar, V. (in prep.). Investigating the connection between multi-frequency radar observations and microphysical properties of falling snow. *Atmospheric Measurement Techniques*.

Park, H., Ryzhkov, A. V., Zrnic, D. S., and Kim, K.-E. (2009). The Hydrometeor Classification Algorithm for the Polarimetric WSR-88D: Description and Application to an MCS. *Weather Forcast.*, 24:730–748.

Pena, O. and Pal, U. (2009). Scattering of electromagnetic radiation by a multilayered sphere. *Comput. Phys. Commun.*, 180:2348–2354.

Penttilä, A., Zubko, E., Lumme, K., Muinonen, K., Yurkin, M. A., Draine, B., Rahola, J., Hoekstra, A. G., and Shkuratov, Y. (2007). Comparison Between Discrete Dipole Implementations and Exact Techniques . *Journal of Quantitative Spectroscopy and Radiative Transfer*, 106(1–3):417–436. {IX} Conference on Electromagnetic and Light Scattering by Non-Spherical Particles.

Petäjä, T., Moisseev, D., O'Connor, E., Lappalainen, H., Levula, J., Lehtinen, K., and Kulmala, M. (2013). Overview of the Biogenic Aerosols -Effects on Clouds and Climate (BAECC) experiment. In *AGU Fall Meeting Abstracts*, page F246.

Petty, G. and Huang, W. (2010). Microwave Backscatter and Extinction by Soft Ice Spheres and Complex Snow Aggregates. *Jour. Atm. Sciences*, 67:769–787.

Petty, G. W. and Huang, W. (2011). The modified gamma size distribution applied to inhomogeneous and nonspherical particles: Key relationships and conversions. *Journal of the Atmospheric Sciences*, 68(7):1460–1473.

Pruppacher, H. and Klett, J. (1997). *Microphysics of Clouds and Precipitation: Second Revised and Enlarged Edition with an Introduction to Cloud Chemistry and Cloud Electricity*, volume 18 of *Atmospheric and Oceanographic Sciences Library*. Kluwer Academic Publishers, 2 edition.

Purcell, E. and Pennypacker, C. (1973). Scattering and Absorption of Light by Nonspherical Dielectric Grains. *Astrophys. J.*, 186:705–714.

Rasmussen, R., Baker, B., Kochendorfer, J., Meyers, T., Landolt, S., Fischer, A. P., Black, J., Thériault, J. M., Kucera, P., Gochis, D., Smith, C., Nitu, R., Hall, M., Ikeda, K., and Gutmann, E. (2011). How Well Are We Measuring Snow: The NOAA/FAA/NCAR Winter Precipitation Test Bed. *Bulletin of the American Meteorological Society*, 93(6):811–829.

Reiter, C. A. (2005). A local cellular model for snow crystal growth. *Chaos, Solitons & Fractals*, 23(4):1111–1119.

Rodgers, C. D. et al. (2000). *Inverse methods for atmospheric sounding: theory and practice*, volume 2. World scientific Singapore.

Rosenkranz, P. W. (1998). Water vapor microwave continuum absorption: A comparison of measurements and models. *Radio Science*, 33(4):919–928.

Sazaki, G., Zepeda, S., Nakatsubo, S., Yokomine, M., and Furukawa, Y. (2012). Quasi-liquid layers on ice crystal surfaces are made up of two different phases. *Proceedings of the National Academy of Sciences*, 109(4):1052–1055.

Sekhon, R. and Srivastava, R. (1970). Snow size spectra and radar reflectivity. *Journal of the Atmospheric Sciences*, 27(2):299–307.

Seliga, T. and Bringi, V. (1976). Potential use of radar differential reflectivity measurements at orthogonal polarizations for measuring precipitation. *Journal of Applied Meteorology*, 15(1):69–76.

Seo, E.-K. and Liu, G. (2005). Retrievals of cloud ice water path by combining ground cloud radar and satellite high-frequency microwave measurements near the arm sgp site. *Journal of Geophysical Research: Atmospheres*, 110(D14).

Shupe, M. D., Kollias, P., Matrosov, S. Y., and Schneider, T. L. (2004). Deriving mixed-phase cloud properties from doppler radar spectra. *Journal of Atmospheric and Oceanic Technology*, 21(4):660–670.

Sihvola, A. H. (1989). Self-consistency aspects of dielectric mixing theories. *Geoscience and Remote Sensing, IEEE Transactions on*, 27(4):403–415.

Sihvola, A. H. (1999). *Electromagnetic Mixing Formulas and Applications*. The Institution of Electrical Engineers, London, UK.

Sihvola, A. H. and Kong, J. A. (1988). Effective permittivity of dielectric mixtures. *Geoscience and Remote Sensing, IEEE Transactions on*, 26(4):420–429.

Silverman, B. W. (1986). *Density Estimation for Statistics and Data Analysis*, volume 26. Chapman and Hall, London.

Smith, P. L. (1984). Equivalent radar reflectivity factors for snow and ice particles. *Journal of Climate and Applied Meteorology*, 23(8):1258–1260.

Stage, S. A. (2013). Comments on an improvement to the brent's method. *International Journal of Experimental Algorithms*, 4(1):1–16.

Stephens, G. L., Vane, D. G., Boain, R. J., Mace, G. G., Sassen, K., Wang, Z., Illingworth, A. J., O'Connor, E. J., Rossow, W. B., Durden, S. L., Miller, S. D., Austin, R. T., Benedetti, A., Mitrescu, C., and The, C. S. T. (2002). THE CLOUDSAT MISSION AND THE A-TRAIN. *Bulletin of the American Meteorological Society*, 83(12):1771–1790.

Stokes, G. M. and Schwartz, S. E. (1994). The Atmospheric Radiation Measurement (ARM) Program: Programmatic Background and Design of the Cloud and Radiation Test Bed. *Bulletin of the American Meteorological Society*, 75(7):1201–1221.

Straka, J., Zrnic, D., and Ryzhkov, A. (2000). Bulk Hydrometeor Classification and Quantification Using Polarimetric Radar Data: Synthesis of Relations. *Jour. App. Met. Clim.*, 39:1341–1372.

Strutt, J. W. L. R. (1871). Lviii. on the scattering of light by small particles. *The London, Edinburgh, and Dublin Philosophical Magazine and Journal of Science*, 41(275):447–454.

Szyrmer, W. and Zawadzki, I. (2010). Snow studies. part ii: Average relationship between mass of snowflakes and their terminal fall velocity. *Journal of the Atmospheric Sciences*, 67(10):3319–3335.

Taflove, A. and Hagness, S. (2005). *Computational Electrodynamics: The Finite Difference Time Domain Method*. Artech House Antennas and Propagation Library. Artech House, third edition.

Tanelli, S., Durden, S., Im, E., Heymsfield, G., Racette, P., and Starr, D. (2009). Next-generation spaceborne cloud profiling radars. In *Radar Conference, 2009 IEEE*, pages 1–4.

Teschl, F., Randeu, W., and Teschl, R. (2013). Single-scattering of preferentially oriented ice crystals at centimeter and millimeter wavelengths. *Atmospheric Research*, 119:112–119.

Thompson, R., Illingworth, A., and Ovens, J. (2011). Emission: a simple new technique to correct rainfall estimates from attenuation due to both the radome and heavy rainfall. *Proceeding WRaH*.

Thurai, M., Huang, G., Bringi, V., Randeu, W., and Schönhuber, M. (2007). Drop shapes, model comparisons, and calculations of polarimetric radar parameters in rain. *Journal of Atmospheric and Oceanic Technology*, 24(6):1019–1032.

Tyynela, J., Leinonen, J., Moisseev, D., and Nousianen, T. (2011). Radar Backscattering from Snowflakes: Comparison of Fractal, Aggregate, and Soft Spheroid Models. *J. Atmos. Oceanic. Technol.*, 28:1365–1372.

Tyynelä, J., Leinonen, J., Westbrook, C., Moisseev, D., and Nousiainen, T. (2013). Applicability of the rayleigh-gans approximation for scattering by snowflakes at microwave frequencies in vertical incidence. *Journal of Geophysical Research: Atmospheres*, 118(4):1826–1839.

Tyynelä, J. and Chandrasekar, V. (2014). Characterizing falling snow using multifrequency dual-polarization measurements. *Journal of Geophysical Research: Atmospheres*, 119(13):8268–8283.

Tyynelä, J., Leinonen, J., Moisseev, D., Nousiainen, T., and von Lerber, A. (2014). Modeling radar backscattering from melting snowflakes using spheroids with nonuniform distribution of water. *Journal of Quantitative Spectroscopy and Radiative Transfer*, 133:504–519.

Um, J., McFarquhar, G., Hong, Y., Lee, S.-S., Jung, C., Lawson, R., and Mo, Q. (2015). Dimensions and aspect ratios of natural ice crystals. *Atmospheric Chemistry and Physics*, 15(7):3933–3956.

van de Hulst, H. (1957). *Light Scattering by Small Particles*. Dover Publications.

Varadan, V. V., Lakhtakia, A., and Varadan, V. K. (1988). Comments on recent criticism of the t-matrix method. *The Journal of the Acoustical Society of America*, 84(6):2280–2284.

Vulpiani, G., Montopoli, M., Passeri, L. D., Gioia, A. G., Giordano, P., and Marzano, F. S. (2012). On the use of dual-polarized c-band radar for operational rainfall retrieval in mountainous areas. *Journal of Applied Meteorology and Climatology*, 51(2):405–425.

Wakasugi, K., Mizutani, A., Matsuo, M., Fukao, S., and Kato, S. (1986). A direct method for deriving drop-size distribution and vertical air velocities from vhf doppler radar spectra. *Journal of Atmospheric and Oceanic Technology*, 3(4):623–629.

Wang, Y. and Chandrasekar, V. (2010). Quantitative Precipitation Estimation in the CASA X-band Dual-Polarization Radar Network. *Journal of Atmospheric and Oceanic Technology*, 27(10):1665–1676.

Warren, S. and Brandt, R. (2008). Optical constants of ice from the ultraviolet to the microwave: A revised compilation. *Jour. Geo. Res*, 113.

Waterman, P. (1965). Matrix formulation of electromagnetic scattering. *Proceedings of the IEEE*, 53(8):805–812.

Weast, R. C., Lide, D., Astle, M., and Beyer, W. (1989). Handbook of chemistry and physics. –1989–1990.

Westbrook, C., Ball, R., Field, P., and Heymsfield, A. (2004a). A theory of growth by differential sedimentation, with application to snowflake formation. *Phys. Rev E*, 70(2).

Westbrook, C., Ball, R., Field, P., and Heymsfield, A. J. (2004b). Universality in snowflake aggregation. *Geophysical research letters*, 31(15).

Westbrook, C. D., Ball, R. C., and Field, P. R. (2006). Radar scattering by aggregate snowflakes. *Quarterly Journal of the Royal Meteorological Society*, 132(616):897–914.

Wiscombe, W. J. (1980). Improved mie scattering algorithms. *Applied optics*, 19(9):1505–1509.

Wood, N. B. (2011). *Estimation of snow microphysical properties with application to millimeter-wavelength radar retrievals for snowfall rate*. PhD thesis, Colorado State University Libraries, Fort Collins, Colorado, 231 pp. https://dspace.library.colostate.edu/handle/10217/48170.

Wood, N. B., L'Ecuyer, T. S., Bliven, F. L., and Stephens, G. L. (2013). Characterization of video disdrometer uncertainties and impacts on estimates of snowfall rate and radar reflectivity. *Atmospheric Measurement Techniques*, 6(12):3635–3648.

Wood, N. B., L'Ecuyer, T. S., Heymsfield, A. J., Stephens, G. L., Hudak, D. R., and Rodriguez, P. (2014). Estimating snow microphysical properties using collocated multisensor observations. *Journal of Geophysical Research: Atmospheres*, 119(14):8941–8961.

Wood, N. B., L'Ecuyer, T. S., Heymsfield, A. J., and Stephens, G. L. (2015). Microphysical Constraints on Millimeter-Wavelength Scattering Properties of Snow Particles. *Journal of Applied Meteorology and Climatology*, 54(4):909–931.

Yang, P., Bi, L., Baum, B. A., Liou, K.-N., Kattawar, G. W., Mishchenko, M. I., and Cole, B. (2013). Spectrally consistent scattering, absorption, and polarization properties of atmospheric ice crystals at wavelengths from 0.2 to 100 μ m. *Journal of the Atmospheric Sciences*, 70(1):330–347.

Yang, W. (2003). Improved recursive algorithm for light scattering by a multilayered sphere. *Appl. Opt.*, 42(9):1710–1720.

Yurkin, M. and Hoekstra, A. (2010). *User manual for the discrete dipole approximation code ADDA v1.0*.

Yurkin, M. A. and Kahnert, M. (2013). Light scattering by a cube: accuracy limits of the discrete dipole approximation and the t-matrix method. *Journal of Quantitative Spectroscopy and Radiative Transfer*, 123:176–183.

Zubko, E., Petrov, D., Grynko, Y., Shkuratov, Y., Okamoto, H., Muinonen, K., Nousiainen, T., Kimura, H., Yamamoto, T., and Videen, G. (2010). Validity criteria of the discrete dipole approximation. *Applied optics*, 49(8):1267–1279.

Acknowledgements

That's definitely the toughest part of the thesis. Probably because it is 2:00 AM and the deadline for the upload of this file is approaching, but also because it is always hard to remember everyone I should acknowledge and spend the right words for each on of them. I can feel the curiosity of all my relatives, friends, colleagues and stalkers of any kind who are recklessly ignore the math-filled chapters of this manuscript and rapidly goes through this text looking just for these last lines to see who and how I acknowledged.

Of course I would like to acknowledge my parents and my sister for growing me up, supporting me in my toughest moments and letting me choose all the possible wrong ways that have build my current consciousness. I also would like to acknowledge my scientific supervisors: Tiziano, Rolando and Dmitri (or whatever is the current official west-style spell of your name) who mentored me and gave me the right advice on how not to be too wrong. Obviously great thanks go to all university colleagues: Nicolo, Flavio, Jussi, Annakaisa, Jani and Maria who share with me their expertise and spent both insightful and funny hours talking about work or whatsoever came in our minds. Finally, special thanks go to my closest friends Simone, Sara, Sara (the special one who could make me also so angry) Mauro, Mauro (the other one which I should have mentioned as a *de facto* brother since that day he married Silvia), Simone (the one without that forest-like beard), Laura, Maria Grazia, Serena, Francesca, Francesco, Martina, Laura (the blonde one), Francesca (Andrea's girlfirend ... damn!! I should had mentioned Andrea in the colleagues list ...), Tommaso, Matteo, Michele, Stefania, Tiziana, Angelo, Stefano . . . and it is already too difficult to make a complete list . . . everyone has shared with me some moments that make me honored and grateful to had the opportunity to spend with them; some of those moments have been hard, some good or even too good, the point is: I have learned something that is essential and pure thanks to those great people and even if most of them are far away and I share just ordinary and yearly happy birthday wishes, they mean something to me that I will never forget.

I would be ungrateful if I do not mention all the unknown genius screenplayers that make possible the broadcast of *The Big Bang Theory* TV show. It is because of you that 20 minutes per week I just let the TV to think in place of my brain; and I am still sane. Some notable mentions goes also to *The IT crowd* and, more recently, *Elementary* people. I wish I could

acknowledge also *Sherlock*'s production, it is for certain a great show, but it seems that it takes a full PhD course to write just one episode and does not seems a fair comparison.

This is the end of the "ordinary part" of the acknowledgments and I am really happy that this has came to an end. That was the part that you should have read sitting on a comfortable sofa, drinking good wine, possibly during winter time in front of a fireplace while outside is snowing and of course your music centre is playing Peter Gariel's cover of *The Book of Love*[1]. That just to let the sweet flow of memories pass softly through your mind. If this part did not let you think about how great is your life it is probably because you did not meet the prescribed environmental requirements.

Again, the fact is that it is too difficult. I feel so much pressure because this is supposed to be my last opportunity to acknowledge everyone during my studies. If think about it, I can not believe it: this is the end (please change the soundtrack accordingly) I should really quit studying and begin working.
Believe me, I am not afraid of working; research and studying involves a large amount of effort and in most countries a PhD course is even considered as an actual job (why the black sheep is always you my beloved Italy?), but this subtle thought that my student life has came to an end is bothering me. Until yesterday anyone who asked me what I do received the same draconian answer: "I study, I am a student and if possible: I will do it for the rest of my life".

The fact is that I am still in love with knowledge and I probably will never cheat on it. I am fascinated from new and astonishing discoveries from the minimum-gene-number synthetic cell to the gravitational wave signature on the cosmic microwave background.

If I look back to my life I would hardly recognize in me a possible PhD candidate, a geek or meteorologist (and in many ways I still not deserve to pretend to put any of these title beside of my name). In primary school I was really bad in writing and I had my hard times with math as well. First two years of high school I have got 8 in discipline[2].

When I was 12 years old I had been badly sick, something that forced me to stay in bed for a couple of months; I was tremendously bored by the just came "Big Brother" TV show so I decided to begin reading some books and I was curious to start with a masterpiece like Marquez's "*One Hundred Years of Solitude*" and from that moment I never stopped reading (and my writing skills had befitted from that too). For the last three years of high school I have moved from the scientific high school to a technical school focused on aeronautics and that was just because I was curious to fly (who wasn't?). Here I was first introduced to the

[1]To anyone is living in the ignorance: *The Book of Love* was the accompanying soundtrack of the last scene of the *Scrubs* TV series finale

[2]For non-Italian readers, Italian high school grades range from 1 to 10. Typically you get 9 in discipline by default, 10 is reserved to heaven creatures who takes care of carrying teachers' bags and bring homework to sick schoolmates; usually 7 means that you are not going to pass to the next grade because of your bad behavior. With an 8 grade you are not a criminal, but you have received your warning.

amazing world of meteorology (obviously I also learned to fly) and I decided to enroll the atmospheric physics course at the university. At college I felt in love for rigorous math, I discovered the infinite possibilities of computer coding (yes, before university course I did not know how computers work) and I discovered why the sky is blue and why the most far mountains looks brightest. Besides the most academic interests, during the college years I have also enjoyed the fun of learning salsa dancing, city administration, political allegiance and nonetheless, commitment to the humanitarian cause (which also reward you letting you to touch the most remote parts of this tiny world).

My point is that, for one reason or another, in a certain moment of my life, I was curious of something and I felt in love with it and I never let it go away. Last year I spent wonderful time in Finland with lovely people and bad, cold weather[3]; I was curious to try to save some money using bicycle instead of public transportation and I found myself riding a spiky-tired bike on a slippery ice surface with no sunlight at all; at present I can barely stay down of my saddle.

Many people say that "curiosity" is what pushes humanity beyond the edges of knowledge and sustain the continuous scientific development and progress. I think that this sentence is overused to explain technical and mathematical science base research, whereas "curiosity" should be cited as the pushing force of all kind scince and arts including literature, history and all kinds of humanities, arts and social sciences. Curiosity to me has been the most basic instinct that makes me what I am. Curiosity is life!

I just would like to acknowledge whoever has introduced me to new things and tickled my interest. Maybe I will never remember that some parts of my life are just because of you and probably you will never remember it too. It does not matter if this leaded me to a new endless love or just let me know that something is simply just not tuned with my reference tone. To a not measurable extend: I am here because of you and you will be part of my life forever.

At present, I am not afraid of quitting studies anymore, even if sometimes I am scared. I will go forward and nostalgically look back to the glorious past. To anyone has not yet found the right path: Never forget to stay curious and always *remember to be happy*.

[3] But believe me dear finnish friends: compared with the graceless lands of Mordor that are the Po plains, Finland is just as like Wonderland